Doctoral Dissertation

A Mechanism-Independent Tsunami Source Modeling for Advanced Rapid Tsunami Estimation

(津波即時予測の高度化に向けた発生メカニズムに依存しない津波波源モデリング)

Tatok Yatimantoro

Graduate School of Science, Hokkaido University
Department of Natural History Sciences

2025 September

Abstract

This study investigates the applicability of static source modeling for rapid tsunami source estimation across diverse generation mechanisms, including seismic, non-seismic, and compound sources. Accurate reconstruction of initial sea surface displacement is essential for tsunami forecasting, hazard assessment, and early warning systems. Here, this study evaluated whether simplified static representations, based on two-dimensional Gaussian functions, can reproduce synthetic tsunami waveforms with sufficient accuracy under varying source conditions.

Two case studies are analyzed: the 2018 Anak Krakatau volcanic tsunami, representing a non-seismic event, and the 2024 Noto tsunami, modeled synthetically as a compound scenario involving both earthquake and submarine landslide sources. For the Anak Krakatau case, tsunami waveform inversion is performed using observed tide gauge data, yielding a deformation pattern and displaced water volume that are consistent with previous studies. For the Noto tsunami, synthetic tsunami waveforms are generated through forward modeling and inverted to evaluate three source scenarios: earthquake-only, landslide-only, and a combined scenario. The combined scenario produces more complex and realistic initial sea surface deformation, yet waveform fitting does not uniformly improve. In fact, the addition of the landslide component reduces inversion accuracy at several stations primarily influenced by the seismic source.

Compared to a method, the proposed framework offers improved adaptability in compound-source environments and requires fewer assumptions about source geometry. Overall, the results confirm that this static inversion approach is not only practical and computationally efficient, but also sufficiently flexible to handle various tsunami generation mechanisms. It therefore holds promise for enhancing the speed and reliability of rapid tsunami estimation and early warning systems, both in real and simulated applications.

Keywords: Initial sea surface displacement; Tsunami waveform inversion; Rapid tsunami estimation; Early warning system.

Table of Contents

Abstract ii

Chapter 1. Introduction 1

1.1 Background and Motivation 1

1.2 Approaches to Tsunami Source Modeling 2

1.3 Challenges in Modeling Non-Seismic and Compound Sources 5

1.4 Objectives and Scope of the Study 7

Chapter 2. Literature Review 9

2.1 Source Modeling for Earthquake-Generated Tsunamis 9

2.2 Source Modeling for Non-Seismic Tsunami Events 11

Chapter 3. Tsunami Source Modeling in a Volcanic Event 14

3.1 Overview of the 2018 Anak Krakatau event 14

3.2 Tsunami Waveform and Bathymetry Data Used 18

3.3 Development of the Initial Sea Surface Displacement Model 22

3.4 Sensitivity analysis 35

3.5 Comparison of Static and Dynamic Source Scenario Tsunamis 45

3.6 Summary of Source Modeling for the 2018 Anak Krakatau Tsunami..... 50

Chapter 4. Tsunami Source Modeling in a Combined Earthquake-Submarine Landslide Event 52

4.1 Overview of the 2024 Noto Tsunami 52

4.2 Synthetic Tsunami Waveforms and Bathymetry Data for Simulation 61

4.3 Tsunami Source Scenarios for Numerical Modeling 63

4.3.1 Earthquake Scenario 64

4.3.2 Submarine Landslide scenario 70

4.3.3 Combine Earthquake and Submarine Landslide Scenario 75

4.4 Estimation of the Potential Tsunami Source Area 79

4.5 Modeling the Initial Sea Surface Displacement 91

4.6 Summary of Synthetic Analysis for the 2024 Noto Tsunami 111

Chapter 5. Discussion and Conclusions 114

5.1 Discussion 114

5.2 Conclusion 122

Acknowledgement 124

References 126

Chapter 1

Introduction

1.1 Background and Motivation

Tsunamis are among the most destructive natural disasters, posing direct threats to the safety and livelihoods of coastal communities. The impacts of such disasters are not limited to loss of life and physical infrastructure damage, but also extend to social, economic, and environmental dimensions, all of which require a long period for recovery. Major events such as the 2004 Indian Ocean tsunami and the 2011 Tohoku tsunami serve as stark reminders of the devastating potential of high-magnitude earthquakes that trigger large-scale tsunamis (Borrero, 2005; Mori et al., 2011). The rapidly propagating tsunami waves, often arriving with little warning, have resulted in hundreds of thousands of casualties and tremendous economic losses.

In addition to globally impactful disasters, regionally generated tsunamis have also demonstrated the potential to cause severe damage. Events such as the 2018 Sulawesi tsunami and the tsunami triggered by the Anak Krakatau eruption in the same year confirmed that even tsunamis generated by smaller, localized sources can produce highly destructive waves (Omira et al., 2019; Muhari et al., 2019). In many of these cases, delayed or inaccurate early warnings were the main contributing factors to the high death toll (Escaleras & Register, 2008). This highlights that the effectiveness of early warning systems does not solely depend on the scale of the event, but also on the speed and accuracy of tsunami source estimation, which determines how quickly and precisely alerts can be issued to the public.

At the same time, the complexity of tsunami generation mechanisms is becoming increasingly recognized, where the source is not always a megathrust earthquake occurring along a subduction zone. Recent studies have shown that tsunamis can also be generated by non-seismic processes, such as submarine landslides, volcanic eruptions, or atmospheric disturbances that cause rapid changes in sea surface pressure. In some cases, tsunamis may even result from a combination of multiple triggering mechanisms, as suspected in the 2024 Noto tsunami in Japan (Tajima et al., 2024; Yanagisawa, Abe, & Baba, 2024; Mulia et al., 2024). These situations illustrate that early warning systems relying solely on seismic parameters are no longer sufficient to address the wide range of possible scenarios.

Therefore, in the context of disaster risk reduction in coastal areas, there is an urgent need to develop tsunami source modeling approaches that are not only rapid and efficient but also flexible enough to accommodate various generation mechanisms. The ability to quickly and accurately estimate the initial sea surface deformation, which serves as the source of tsunami waves, is a key component in building adaptive and responsive warning systems. Against this background, this study seeks to address these challenges by evaluating a static source modeling approach designed to support early estimation in situations with limited data and time.

1.2 Approaches to Tsunami Source Modeling

Tsunami source modeling is a critical first step in the simulation and early warning process, as the initial sea surface deformation generated by the source determines the direction, speed, amplitude, and arrival time of tsunami waves across various locations. Over the past several decades, a range of approaches has been developed to represent tsunami sources, ranging from physics-based forward modeling methods to data-driven estimation techniques such as tsunami waveform inversion. Each approach has its strengths and limitations, depending on the availability of data, the type of generation mechanism, and the intended application, whether for post-event analysis or real-time early warning systems.

Traditional forward modeling methods are commonly applied in the context of megathrust earthquakes, where elastic dislocation models are used to compute seafloor deformation based on fault parameters such as length, width, depth, dip angle, slip direction, and slip amount. These models serve as the initial condition for tsunami propagation simulations. Although this approach is highly effective for large-scale events with well-defined seismic sources, it typically requires substantial geophysical information and computational time, making it less suitable for real-time applications.

As an alternative, tsunami waveform inversion has been developed to extract source information directly from recorded tsunami signals at observation stations such as tide gauges, wave gauges, or bottom pressure sensors. In this method, the co-seismic or initial sea surface deformation is derived by inverting recorded waveforms using Green's functions to relate the source and the observed signal. While this method has been widely used in post-event analysis and successfully applied to major events such as the 2004 Sumatra tsunami (e.g., Tanioka et al., 2006; Fujii & Satake, 2007), the 2010 Chile tsunami (e.g., Fujii & Satake, 2013), and the 2011 Tohoku tsunami (e.g., Fujii et al., 2011; Gusman et al., 2012), its application in early warning remains challenging due to computational demands and limited observation networks. One example of the application of real-time initial sea surface deformation estimation is demonstrated by Tsushima et al. (2009), who developed a tsunami forecasting system using data from offshore bottom pressure sensors without relying on prior assumptions about fault geometry. The system is capable of updating forecasts every minute and has shown high accuracy in predicting coastal tsunami arrival times and amplitudes, even more than 20 minutes before the peak wave reaches the shoreline along the Pacific coast of northeastern Japan, as demonstrated in a simulation of the 1896 Sanriku tsunami.

Among the various approaches, there is a growing need for source models that are simple yet sufficiently representative, especially for supporting rapid estimation in early warning contexts. One promising method is the use of static source models based on Gaussian functions or other simplified distributions (Saito, Satake, & Furumura, 2010). These models are not intended to reconstruct the detailed physical source processes but rather to provide a rapid estimate of the initial sea surface deformation capable of producing tsunami waveforms consistent with the reference scenarios used in this study. This approach is particularly useful under conditions of limited data and time and is more flexible in accommodating different types of sources, including those generated by submarine landslides or volcanic eruptions.

In this study, the static source modeling approach serves as the primary method for evaluating how well simplified representations of initial sea surface deformation can reproduce reference tsunami waveforms. The inversion method is not the main focus but is employed as a supporting tool to assess the effectiveness of the source models. The primary objective of this research is not to develop a new inversion algorithm, but rather to assess the ability of static source models to realistically and efficiently capture the essential characteristics of tsunamis generated by various source mechanisms.

1.3 Challenges in Modeling Non-Seismic and Compound Sources

Although tsunami source modeling based on elastic dislocation has proven effective for events triggered by megathrust earthquakes in subduction zones, this approach is not always sufficient for explaining tsunamis generated by non-seismic processes or by multiple contributing mechanisms. Over the past two decades, an increasing number of tsunami events have demonstrated that in addition to earthquakes, alternative sources such as submarine landslides, submarine volcanic eruptions, and atmospheric disturbances (e.g., pressure waves from explosive eruptions) can also generate destructive tsunami waves. In some recent cases, tsunamis have been found to originate from compound mechanisms, where an earthquake triggers a submarine slope failure almost simultaneously.

One of the main challenges in modeling non-seismic sources lies in the lack of direct observational data that can constrain the physical parameters of the tsunami source. Unlike earthquakes, which are typically accompanied by rich seismic and geodetic datasets, events such as submarine landslides, volcanic eruptions, and atmospheric disturbances often go undetected by conventional monitoring systems. These non-seismic sources involve fundamentally different physical processes, as they do not generate fault slip or elastic dislocation. Instead, such events are characterized by mass movement, localized bathymetric changes, and complex fluid-solid interactions (e.g., Ward, 2001; Harbitz et al., 2006; Paris, 2015). As a result, critical parameters such as landslide volume, source geometry, initial depth, movement velocity, and timing are difficult to estimate accurately, particularly in real-time scenarios. This uncertainty directly impacts tsunami modeling outcomes, leading to discrepancies in predicted amplitudes, arrival times, or wave propagation patterns compared to actual observations.

Furthermore, tsunami waves generated by non-seismic sources often exhibit spectral and temporal characteristics that differ from those of seismically generated tsunamis (e.g., Okal & Synolakis, 2004; Tappin et al., 2014; Paris, 2015). For instance, submarine landslides tend to produce shorter-period waves with more localized propagation, although the amplitudes can be very large near the source. In some cases, such tsunamis arrive significantly earlier than predicted by earthquake-based models. This mismatch can result in the failure of early warning systems that rely solely on seismic data, as illustrated by the 2018 Palu tsunami and the 2024 Noto event.

The challenges are further compounded when a tsunami is generated by a combination of mechanisms, such as an earthquake that induces a submarine slope failure. In these scenarios, the tsunami waveform observed in the field is a superposition of waves generated by multiple processes occurring in close succession but with different dynamics. Distinguishing the contribution of each source to the overall waveform becomes extremely difficult, especially in the absence of sufficient observational data. Consequently, source estimation based on a single triggering mechanism may result in misleading or incomplete interpretations.

These circumstances underscore the importance of developing tsunami source modeling approaches that can flexibly accommodate different types of sources, including compound mechanisms. Static source models with simplified configurations may serve as a useful first step in emergency situations or when data are limited. However, these models must be systematically validated to define their limitations, especially when applied to complex cases. This study addresses this need by designing numerical experiments to evaluate how well static representations of initial sea surface deformation can reproduce physically relevant tsunami waveforms for both non-seismic and compound scenarios.

1.4 Objectives and Scope of the Study

Building on the background described above, this study is driven by the need for tsunami source modeling approaches that can provide rapid estimates of initial sea surface deformation, particularly for events not solely caused by earthquakes. This modeling strategy is expected to address operational challenges that arise when tsunami generation involves non-seismic processes or a combination of multiple mechanisms. In the context of early warning systems, the success of an initial estimate strongly depends on the speed and accuracy of the deformation representation. Therefore, the adopted approach must not only be computationally efficient but also adaptable to diverse source characteristics.

This study specifically investigates the capacity of static source models to reproduce initial sea surface deformation patterns relevant to tsunami generation from various source types. The approach employs simplified two-dimensional Gaussian distributions to construct the initial deformation model without explicitly simulating the generation dynamics. The model's performance is evaluated through waveform inversion to determine how well the inverted surface deformation reflects the complexity of the original tsunami source scenario.

To explore the applicability of the approach, two case studies are examined. The first is the 2018 Anak Krakatau volcanic tsunami, a representative example of non-seismic tsunami generation following a flank collapse triggered by an eruption.

The second is a synthetic scenario based on the 2024 Noto tsunami in Japan, which prior studies suggest was generated by a combination of earthquake rupture and submarine landslide. This synthetic scenario is numerically constructed using parameters derived from previous research to represent a complex multi-mechanism source. Three primary source configurations are analysed: earthquake-only, landslide-only, and combined earthquake–landslide.

The scope of this study includes the construction of initial sea surface deformation models, simulation of tsunami wave propagation, and waveform inversion to evaluate the accuracy of the static source models. The evaluation is carried out by comparing inversion results with reference simulations in terms of waveform shape, amplitude, arrival time, and spatial distribution of deformation. Through this approach, the study contributes to a deeper understanding of tsunami source characteristics and provides a scientific foundation for the use of simplified models in early warning systems with limited observational input. As a final note, certain parts of this manuscript have been adapted from Yatimantoro et al. (2025) for methodological development and refinement of scientific context within the scope of this research.

Chapter 2

Literature Review

2.1 Source Modeling for Earthquake-Generated Tsunamis

Earthquake-generated tsunamis are the most common type of tsunami and have been the main focus of source modeling methodology development over the past several decades. In this context, the tsunami source is represented as seafloor deformation resulting from fault rupture during an earthquake. This modeling approach reflects a direct link between tectonic processes beneath the Earth's surface and changes in sea surface elevation that trigger tsunami waves. Given the relatively regular nature of earthquake sources and their observability through geophysical data, earthquake-generated tsunami models can be developed using standardized and widely reproducible frameworks.

Conventional modeling approaches utilize geophysical observations, such as seismic and geodetic data, to estimate the slip distribution on the fault plane. This distribution is then converted into seafloor deformation and used as the initial input for tsunami propagation simulations. The vertical seafloor deformation is generally assumed to be accurately inferable from fault movement at depth, and this method has proven effective in supporting tsunami hazard analysis and scenario-based forecasting systems.

A foundational contribution to tsunami source modeling was made by Satake (1987), who introduced the concept of tsunami waveform inversion. In his study of the 1983 Japan Sea earthquake, Satake (1987) demonstrated that tsunami waveforms observed at tide gauge stations could be used to estimate slip distribution on the fault plane. By superimposing responses from unit sources, he was able to quantitatively reconstruct the spatial characteristics of the source. This finding established a new paradigm in which tsunami waveforms themselves could be used as direct information for source estimation.

Over time, tsunami waveform inversion methods have advanced significantly. Subsequent studies applied this technique to estimate the initial sea surface deformation directly, without requiring explicit assumptions about fault geometry. This presents a key advantage for operational applications. Studies such as Baba, Cummins and Hori (2005), Satake et al. (2005), Saito, Satake and Furumura (2010), Saito et al. (2011), and Gusman, Mulia and Satake (2018) have demonstrated the effectiveness of this approach in reconstructing earthquake-generated sea surface deformation. Yamanaka and Tanioka (2024) further developed this method to account for non-linear effects in tsunami propagation, extending its applicability to more complex conditions. A common assumption in these methods is that the initial velocity components of tsunami waves are negligible, which is considered reasonable for earthquake-generated events.

Tsunami waveform inversion has also been adapted for use in real-time tsunami forecasting systems. Studies by Yasuda et al. (2007) and Tsushima et al. (2009) developed systems capable of updating source estimations based on incoming observational data. These developments show that tsunami waveform inversion is not only relevant for post-event analysis but also highly applicable for operational forecasting.

Furthermore, waveform inversion has been incorporated into joint inversion frameworks, which integrate tsunami waveform data with geodetic or seismic data to enhance source resolution. This approach was first applied by Satake (1993) to estimate slip distributions of the 1944 and 1946 earthquakes using a combination of tsunami and geodetic data. Since then, the method has been refined and expanded, as evidenced by studies such as Tanioka, Satake and Ruff (1995), Baba et al. (2009), Yokota et al. (2011), and Gusman et al. (2017). These studies show that by combining different types of observational data, source estimation can be conducted with greater spatial and temporal accuracy. The integration of geodetic, seismic, and tsunami data enables source modeling that not only reconstructs seafloor deformation but also provides a more comprehensive understanding of earthquake mechanisms.

2.2 Source Modeling for Non-Seismic Tsunami Events

Beyond tectonic processes, various non-seismic mechanisms can also generate significant tsunamis, including submarine landslides, volcanic activity, and atmospheric disturbances due to explosive eruptions. Each of these mechanisms possesses distinct physical characteristics and often involves complex multi-physics dynamics. Unlike earthquake-generated tsunamis, which can be modeled using standardized fault parameters, non-seismic sources are often difficult to represent simply because they may involve interactions between solid, liquid, and in some cases, gaseous media.

The primary challenge in non-seismic source modeling lies in the scarcity of direct observational data and the high uncertainty surrounding source parameters, such as landslide volume, eruption depth, or atmospheric pressure profiles. Additionally, many non-seismic events are localized and sudden, making them less likely to be captured by conventional seismic monitoring networks. As a result, modeling approaches for these events require greater flexibility, both in numerical schemes and in assumptions about the source. This has led to the development of inversion methods based on tide gauge data, satellite observations, and exploratory scenario-based simulations to comprehensively understand their potential and impacts.

An illustrative example is the 2018 Palu tsunami. This event demonstrated that co-seismic deformation alone was insufficient to explain the extreme inundation observed along Palu Bay. Gusman et al. (2019), through a joint inversion approach using tide gauge and satellite observations, revealed complex vertical motions not entirely attributable to fault slip. Numerical simulations that combined fault deformation with multiple landslide scenarios, both subaerial and submarine, yielded results that better matched field observations. This study highlights the need for source modeling frameworks that can accommodate compound sources, especially in narrow bays or basins prone to wave amplification.

In addition to landslides, submarine volcanic activity can also generate damaging tsunamis. Sandanbata et al. (2022) analyzed an event at the Sumisu caldera, where a moderate-magnitude volcanic earthquake was capable of generating meter-scale tsunamis. They proposed a composite source model involving circular faulting and vertical cracking induced by pressurized magma. Despite the relatively low seismic energy release, the resulting vertical seafloor deformation was sufficient to trigger observable tsunami waves. Such events underscore that tsunami modeling for volcanic activity must go beyond magnitude-based assessments and consider more complex mechanisms, including internal pressure dynamics and caldera deformation.

A broader source paradigm was further demonstrated by the 2022 Hunga Tonga–Hunga Ha'apai eruption, which triggered a globally observed tsunami without significant seafloor deformation. Fujii and Satake (2024a) showed that the tsunami was generated by atmospheric pressure waves, specifically Lamb and Pekeris waves, that propagated concentrically following the massive explosion. Using DART buoy data and tsunami inversion techniques, they estimated the pressure amplitudes, propagation speeds, and origin times of these atmospheric waves. The Proudman resonance phenomenon, which occurs when the speed of atmospheric waves approaches that of long ocean waves, explained the tsunami generation mechanism in this case. This study expands the theoretical scope of tsunami generation and reinforces the need for modeling and warning systems that can detect and respond to non-traditional tsunami sources.

Findings from these studies show that non-seismic tsunami events exhibit highly diverse characteristics and often involve unconventional and complex generation mechanisms. Therefore, source modeling for such events requires approaches tailored to their unique physical nature and must consider the potential for multiple interacting mechanisms within a single event.

Chapter 3

Tsunami Source Modeling in a Volcanic Event

3.1 Overview of the 2018 Anak Krakatau Tsunami

Among recent tsunami events, the 2018 Anak Krakatau tsunami stands out due to its unusual generation mechanism and strong relevance to ongoing efforts to improve source modeling for non-seismic tsunamis. Unlike most historical tsunamis, which are typically triggered by large undersea earthquakes, this event was primarily caused by a volcanic flank collapse that generated a devastating tsunami in the absence of significant ground shaking. This unique characteristic makes it a compelling case for evaluating alternative modeling approaches that do not rely solely on seismic data. In addition to causing numerous fatalities and severe damage along the coastlines of Java and Sumatra, the event also provides valuable insight into the role of flank collapse in tsunami generation, which remains underrepresented in current early warning systems. To gain a more comprehensive understanding of the event, it is important to review the geographical setting and geological background of Anak Krakatau volcano.

The Anak Krakatau volcano is situated between Indonesia's Java and Sumatra islands in the Sunda Strait. According to Abdurrachman et al. (2018), the observed volcanic activity can be interpreted as an indicator of the transition of the subduction system from oblique orientation along Sumatra to perpendicular orientation along Java. The Anak Krakatau Volcano has a significant historical connection with its predecessor, the ancient Krakatau Volcano. The history of the eruption of the Krakatau volcano and its resulting tsunami can be traced back to the year 416 (Soloviev & Go 1974).

On December 22, 2018, Anak Krakatau erupted, resulting in a devastating tsunami in the Sunda Strait and surrounding areas. According to a report from the National Agency for Disaster Management (BNPB 2019), this tsunami resulted in the death of 437 people, with ten individuals still missing and 31,943 injured. An additional 16,198 people were evacuated from affected areas. The most severe devastation occurred along the west coast of Java, particularly in the Banten Province, where the tsunami reached a maximum run-up height of 13.5 meters with a run-up distance of approximately 160 meters (Muhari et al. 2019). According to the Indonesian Agency for Meteorology, Climatology, and Geophysics (BMKG) earthquake database, a seismic event occurred on December 22, 2018, at 13:55:48 (UTC), with a magnitude of 4.9. The epicentre of this event was situated near the Anak Krakatau volcano. A low-frequency component in the seismic waveform provides strong evidence of a potential correlation between the event and the volcanic eruption (Permana, Yatimantoro & Handayani 2023). Satellite imagery from the Japan Aerospace Exploration Agency (JAXA 2018) captured a significant collapse in the southwestern section of the Anak Krakatau caldera before (December 10, 2018) and after (December 22, 2018) the eruption, further indicating the tremendous nature of the event.

Previous studies have suggested that the collapse of the southwestern side of Anak Krakatau was the primary source of the tsunami (Grilli et al. 2019; Heidarzadeh et al. 2020; Mulia et al. 2020; Omira & Ramalho 2020; Paris et al. 2020; Grilli et al. 2021). These studies were conducted to understand the flank collapse mechanism and tsunami from the 2018 Anak Krakatau eruption.

Grilli et al. (2019) used NHWAVE (Non-Hydrostatic Wave Model), a three-dimensional non-hydrostatic model specifically designed to simulate landslide-generated tsunamis, including vertical acceleration and frequency dispersion effects. In this model, the slide is represented as a depth-averaged layer fully coupled with the surrounding water, with rheological behavior modeled either as a Newtonian fluid or a granular medium governed by Coulomb friction. They applied NHWAVE to analyze the collapse characteristics of Anak Krakatau, accounting for the rheology of the collapsed material. The resulting wave field was then used to initialize FUNWAVE-TVD (Fully Non-linear Boussinesq Wave Model with Total Variation Diminishing), a fully nonlinear and dispersive two-dimensional Boussinesq-type model, which was applied to simulate tsunami propagation from the near-field to the far-field. The geometry and failure surface of Anak Krakatau were reconstructed based on satellite imagery captured before and after the collapse, resulting in an estimated collapse volume of 0.27 km^3.

Heidarzadeh et al. (2020) used COMCOT (Cornell Multi-grid Coupled Tsunami Model), a numerical model based on nonlinear shallow water equations, to simulate the tsunami generated by the flank collapse. Their results showed that a collapsed volume of 0.175 km^3 provided the best agreement with the available observational data.

Mulia et al. (2020) estimated a collapse volume of 0.24 km^3. They simulated the avalanche dynamics using VolcFlow, a two-dimensional depth-averaged numerical model that was initially developed for simulating volcanic avalanches and later extended to model both the landslide motion and water flow using shallow water equations based on mass and momentum conservation. This coupled model efficiently represents the interaction between slide material and water, making it suitable for landslide-induced tsunami studies. The resulting wave field was then propagated to more distant coastal areas using the FUNWAVE-TVD model. Their simulation results showed that the collapse caused waves higher than 40 meters in the area surrounding the volcano.

Omira and Ramalho (2020) employed a multilayer viscoplastic model to simulate collapse mechanisms. They conducted a simulation that included two subsequent failures occurring five seconds apart, with volumes of 0.1 km^3 and 0.035 km^3, respectively. They utilised the same model to calculate the propagation of the resulting tsunami in the near and far fields. This generated a leading wave measuring 45 meters near the volcano.

Paris et al. (2020) employed a two-layer depth-averaged coupled model, AVALANCHE, to describe the sliding process. This model incorporates granular rheology and Coulomb friction to adjust for the slide characteristics and dispersive effects of the water flow component. By utilising satellite and aerial photographs taken before and after the collapse and thoroughly analysing simulated water waves in contrast to far-field data, such as tide gauges and field surveys, Paris et al. (2020) could reproduce the total volume of the landslide, including subaerial and submarine, to be approximately 0.15 km^3.

The strategy of Grilli et al. (2021) was similar to that used by Grilli et al. (2019) to ascertain the collapse mechanism and tsunami generation. In contrast to Grilli et al. (2019), the NHWAVE model incorporates vertical acceleration, specifically non-hydrostatic pressures, within the layer of the slide material. The findings indicate that a collapsed volume of 0.224 km^3 is most suitable for alignment with the observed tsunami flow depth and run-up, as evidenced by several post-event field surveys, tide gauge records, and eyewitness testimonies.

The results of previous studies, which modeled the collapse and tsunami, suggest that the tsunami height exceeded 40 meters above the mean sea level during propagation near the volcano. Zhu et al. (2021) conducted a tsunami waveform inversion to construct an initial sea surface displacement model for the 2018 tsunami. In their model, the maximum height of the initial sea surface was less than 10 m, which was significantly smaller than the tsunami heights simulated around the source areas in other studies (Grilli et al. 2019; Heidarzadeh et al. 2020; Mulia et al. 2020; Omira & Ramalho 2020; Paris et al.2020; Grilli et al. 2021).

3.2 Tsunami Waveform and Bathymetry Data Used

This study used the Digital Elevation Model (DEM) for bathymetry and topography, as in Mulia et al. (2020), which was derived from the National Bathymetry (BATNAS) dataset, and the topographic data for Anak Krakatau were derived from the National Digital Elevation Model (DEMNAS). The BATNAS and DEMNAS datasets are produced by the Indonesian Geospatial Agency (BIG). In their study, Mulia et al. (2020) employed two nested simulation grids with different resolutions: a three-arc-second grid for the vicinity of the Anak Krakatau volcano and a six-arc-second grid for the broader Sunda Strait region. In this study, a single simulation grid with a uniform resolution of three arc-seconds was adopted by resampling the dataset used by Mulia et al. (2020) (Figure 3.1). This gridded elevation model represents the pre-collapse surface conditions of the volcano prior to the 2018 event.

The 2018 Anak Krakatau tsunami was recorded at four tide gauge stations in the Sunda Strait: Ciwandan, Serang, Kota Agung, and Panjang (Figure 3.1). BIG provides tide gauge data with a 1-minute sampling interval (https://srgi.big.go.id/map/jkg-active). A polynomial fitting function was used to estimate the astronomical tides. By using these estimates to obtain the tsunami waveform, the tidal waves were removed from the original records (Figure 3.2).

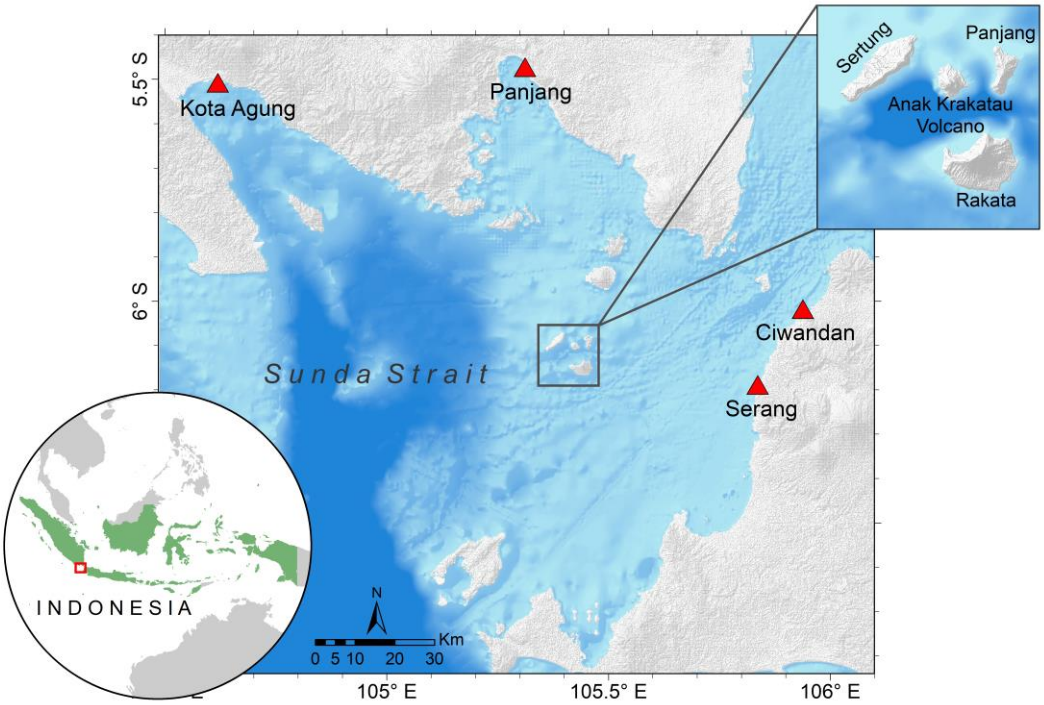

Figure 3.1. The computational area and locations of the tide gauge stations that recorded the 2018 Anak Krakatau tsunami (red triangles). In this study, the tide gauge stations were assumed to be located at the sites determined by Mulia et al. (2020).

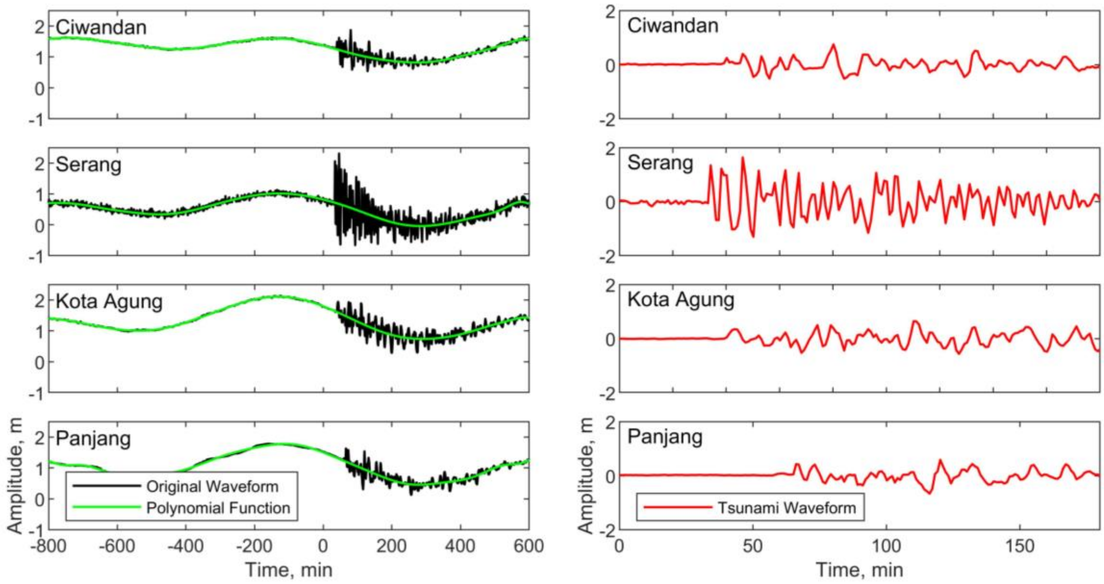

Figure 3.2. Data for the observed waveform (black line), polynomial function (green line), and tsunami waveform (red line) at Ciwandan, Serang, Kota Agung, and Panjang stations, respectively. Time 0 minute indicates the origin time of a low-frequency seismic event by the BMKG (13:55:48 UTC)

3.3 Development of the Initial Sea Surface Displacement Model

In the modeling, sea surface displacements were assumed to occur instantaneously at a specific time. As previously noted, the eruption is considered to have been initiated at 13:55:48 UTC; however, the timing has some uncertainties for this modeling approach, as it is not necessarily the tsunami generation time. Determining the appropriate origin time for a tsunami is vital because tsunami waveform inversion results are strongly influenced by the assumed tsunami occurrence time. Four potential initial times of 13:54:00, 13:55:00, 13:56:00, and 13:57:00 UTC were tested to determine the optimal time for a tsunami.

The tsunami source area was assumed to be located southwest of the volcano, with dimensions of 2.5 × 2.0 km². These assumptions are consistent with the location and size of the volcanic flank collapse during the eruption, as indicated by satellite imagery from JAXA (2018). Unit sources for sea surface displacement were then assigned to the assumed tsunami source area. Each unit source had a two-dimensional Gaussian shape with a horizontal variance represented by σ (Yamanaka et al. 2019; Yamanaka & Shimozono 2021). The initial water surface distribution for each source unit is described as follows:

$$\eta(x,y) = m_j\, exp\left[-\frac{\left(x-x_j\right)^2 + \left(y-y_j\right)^2}{2\sigma^2}\right] \quad (3.1)$$

where η represents the water surface elevation above the mean sea level for the unit source, x and y denote the locations along the longitudinal and latitudinal directions, respectively, x_j and y_j are the centre coordinates of each unit source, and m_j is the height of the water surface at the central location of the unit source. The index j refers to the *j-th* unit source, with 20 unit sources used in this study (Figure 3.3). This study employed values of 250, 375, and 500 meters for σ to investigate the effects of unit source size on model accuracy. A total of 20 unit sources (Figure 3.3) were used, each assuming a different value of σ, and the corresponding inversion results were compared to identify the most effective unit source size.

The interval between the assigned unit sources was fixed at 0.5 km within a rectangular frame for the source area (Figure 3.3). Tsunami waveforms from each Gaussian source were then simulated at the four tide gauge stations using a linear long wave model to produce Green's functions. The governing equations for the 2D linear long wave model are as follows (e.g., Yamanaka and Tanioka, 2024):

$$\frac{\partial \eta}{\partial t} + \frac{1}{R\cos\lambda}\left[\frac{\partial}{\partial \lambda}(M\cos\lambda) + \frac{\partial N}{\partial \theta}\right] = 0 \tag{3.2}$$

$$\frac{\partial M}{\partial t} + \frac{gh}{R}\frac{\partial \eta}{\partial \lambda} = -fN \tag{3.3}$$

$$\frac{\partial N}{\partial t} + \frac{gh}{R\cos\lambda}\frac{\partial \eta}{\partial \theta} = fM \tag{3.4}$$

where η represents the water surface elevation from the mean sea level; M (= Uh) and N (= Vh) represent the fluxes in the latitudinal (λ) and longitudinal (θ) directions, respectively; U and V are the velocities in the latitudinal and longitudinal directions, respectively; h is the still water depth; g is the gravitational acceleration; R is the Earth's radius; f is the Coriolis coefficient; and t is time. A simulation time step of 0.3 seconds was used, which met the Courant–Friedrichs–Lewy (CFL) stability conditions and simulated the tsunami propagations for 120 minutes. All non-linear effects occurring over the sea area near the volcano and beyond were neglected in this analysis.

This study performed the tsunami waveform inversion using the initial wave of the tsunami as recorded by tide gauge stations. The observed tsunami waveforms are expressed as a superposition of Green's functions at each station. To obtain a stable solution, the inversion employed two hyperparameters, following an approach similar to that of Hossen et al. (2015). The inversion equation is as follows:

$$\begin{bmatrix} \boldsymbol{G}_{ij} \\ \alpha\boldsymbol{S}_{jj} \\ \beta\boldsymbol{I}_{jj} \end{bmatrix} \boldsymbol{m}_j = \begin{bmatrix} \boldsymbol{d}_i \\ \boldsymbol{0} \\ \boldsymbol{0} \end{bmatrix} \tag{3.5}$$

where $\boldsymbol{G}_{ij}$ is Green's function, $\boldsymbol{S}_{jj}$ is the smoothing matrix constructed following the formulation of Baba et al. (2005), as shown below:

$$0 = m_{p-1,q} + m_{p+1,q} + m_{p,q-1} + m_{p,q+1} - 4m_{p,q} \tag{3.6}$$

where $m_{p,q}$ denotes the initial sea-surface displacement at the source grid point located at position (p, q), with p indexing the longitudinal direction and q the latitudinal direction. $\boldsymbol{I}_{jj}$ is the identity matrix, m_j is the height of the water surface at the central location of the Gaussian source, $\boldsymbol{d}_i$ is the observed tsunami waveform, α is the smoothing parameter, and β is the damping parameter. The index i corresponds to the observation points (tide gauge stations) with ($i = 1, 2, ..., N$), where N is the number of observed tsunami waveforms. Index j corresponds to the unit sources, with ($j = 1, 2, ..., M$), where M is the total number of unit sources used to discretise the tsunami source area. The model parameters were estimated using a regularized least-squares approach applied to the above equation.

This study determined the optimal values of the two hyperparameters, α and β, within an assumed range for each value using a grid search cross-validation process. Following the approach of Yokoi et al. (2023), a "leave-one-station-out" cross-validation method was employed. In this procedure, the tsunami waveform observed at one tide gauge station was used as evaluation data. The inversion using tsunami waveforms observed at the other three stations was conducted assuming values of α and β, producing a sea-surface deformation model. The difference in the observed waveform for evaluation and synthetic waveform from the model was then evaluated based on the root mean square error (RMSE) for quantifying the effects of hyperparameters, defined as:

$$RMSE = \sqrt{\frac{1}{N}\sum_{i=1}^{N}\left(u_i^{obs} - u_i^{syn}\right)^2} \tag{3.7}$$

where u_i^{obs} and u_i^{syn} represent the observed and synthetic waveform amplitudes at time index i, respectively, and N is the total number of time steps. The tsunami waveforms at four tide gauge stations were each used as the evaluation waveform in turn, resulting in four different RMSE values for each pair of α and β. The sum of these four RMSE values was defined as the total RMSE. A range of α and β combinations was tested to evaluate the total RMSE as a function of the hyperparameters. To identify the optimal values, the relationship between total RMSE and the $\alpha - \beta$ pairs was visualized, and the pair yielding the minimum total RMSE was selected. Using these optimal hyperparameter values, the final inversion was then performed with all four observed tsunami waveforms. An illustration of the grid-search cross-validation procedure is shown in Figure 3.4.

This study conducted a total of twelve inversion simulations based on the combinations of four origin times at 13:54:00, 13:55:00, 13:56:00, and 13:57:00 UTC and Gaussian σ values of 250, 375, and 500 meters (Figure 3.5). Table 1 lists the total RMSE values for all scenarios and shows that the minimum total RMSE value was 0.63, obtained from a combination of an origin time of 13:56:00 UTC and a Gaussian scale of 250 meters. This was achieved using the optimal α and β values of 0.0032 and 0.0017, respectively, as shown in Figure 3.6a. Figure 3.6b shows the initial sea surface displacement model for the 2018 Anak Krakatau tsunami. The estimated initial sea surface displacement indicates subsidence around the collapsed area, followed by uplift. According to Paris et al. (2013), the results obtained in this study, which reflect the characteristics of the initial sea surface displacement, are similar to those of a volcanic tsunami caused by subaerial failure. Within this specific category, subsidence was observed in the area surrounding the collapse site, followed by wave propagation leading to a crest. The maximum sea surface height estimated in this model, approximately 90 meters during tsunami generation, is reasonable considering the extent of the resulting environmental tsunami damage to the Sertung and Rakata Islands surrounding the Anak Krakatau volcano, as shown by Muhari et al.'s (2019) survey.

To characterise the source model quantitatively, this study computed water volume, which was determined as:

$$Vt = \iint |\eta_t| d\lambda d\theta \tag{3.8}$$

where η_t denotes the height of the water surface in the developed source model. The absolute value of η_t was used to account for the total displacement of water, regardless of whether the surface displacement was positive or negative, ensuring that the contributions of uplift and subsidence were not canceled out during integration. The computed volume in this model was 0.19 km^3. For comparison, previous studies estimated that the volume of the collapsed volcanic flank ranged from 0.14 to 0.27 km^3 (Grilli et al. 2019; Heidarzadeh et al. 2020; Mulia et al. 2020; Omira & Ramalho 2020; Paris et al. 2020; Grilli et al. 2021). Thus, the water volume in the present model was consistent with the volume of collapsed materials reported in previous studies regarding the order of magnitude. The static source model of Zhu et al. (2021) introduced a volume of elevated water, which had a different definition from the volume calculated in this study, and determined it for their model as 0.03 km^3. Comparing the estimations from this study with those of Zhu et al. (2021), the current estimation is likely more reasonable. A comparison between the volume of water and the volume of the collapsed volcanic flank is relevant because flank collapse directly triggers the displacement of seawater in the surrounding region. The displaced water volume (Vt) reflects the combined effects of uplift and subsidence caused by collapse, leading to sea surface deformation. Despite the physical differences between solid materials and water, the consistency between the water volume and collapse volumes reported in previous studies demonstrates that the value of Vt can be correlated with that of the collapsed volume.

Figure 3.6c compares the waveforms at the Ciwandan, Serang, Kota Agung, and Panjang stations. Waveform fitting between synthetic and observed data generally fits within the inversion time windows. The arrival times of the synthetic and the observed waves at the Ciwandan station matched well; the simulated tsunami arrived approximately one minute after the observed one. The amplitude of the simulated tsunami within the time window at this station also appeared to fit the observations well. At the Serang station, there was strong agreement between the synthetic and observed waveforms within the inversion time window regarding the timing and amplitude of the tsunami. The amplitude of the synthetic waveform at the Kota Agung station was slightly smaller than that observed, although the simulated arrival time aligned well with the observed data. This discrepancy may be attributed to several factors, such as limitations in the resolution of nearshore bathymetric data, local amplification effects not captured by the model, or the absence of complex source processes, such as asymmetrical mass failure or multi-stage sliding. In contrast, the waveform at Panjang station exhibited notable differences from the observation in both amplitude and arrival time. A more detailed analysis of the Panjang station will be presented in the following subchapter.

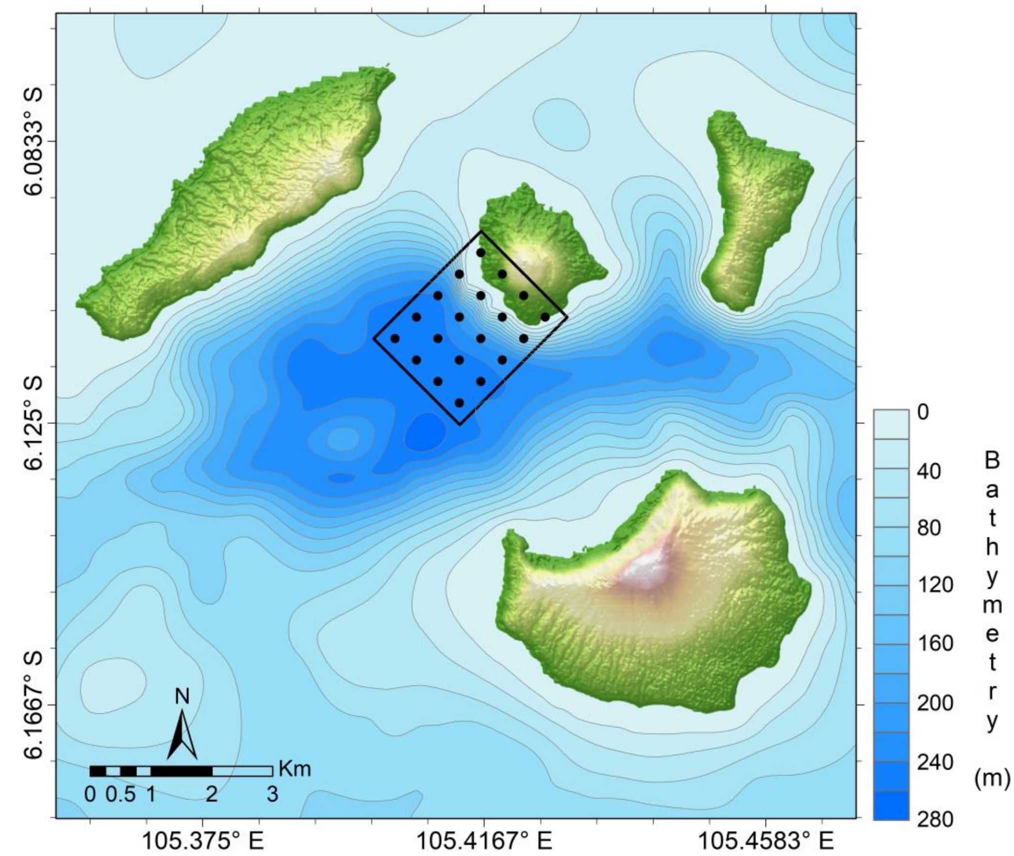

Figure 3.3. Assumed source area (black rectangle). The black dots indicate the central location of the assigned Gaussian sources with an interval of 0.5 km. The gray lines represent depth contours with 20-meter intervals.

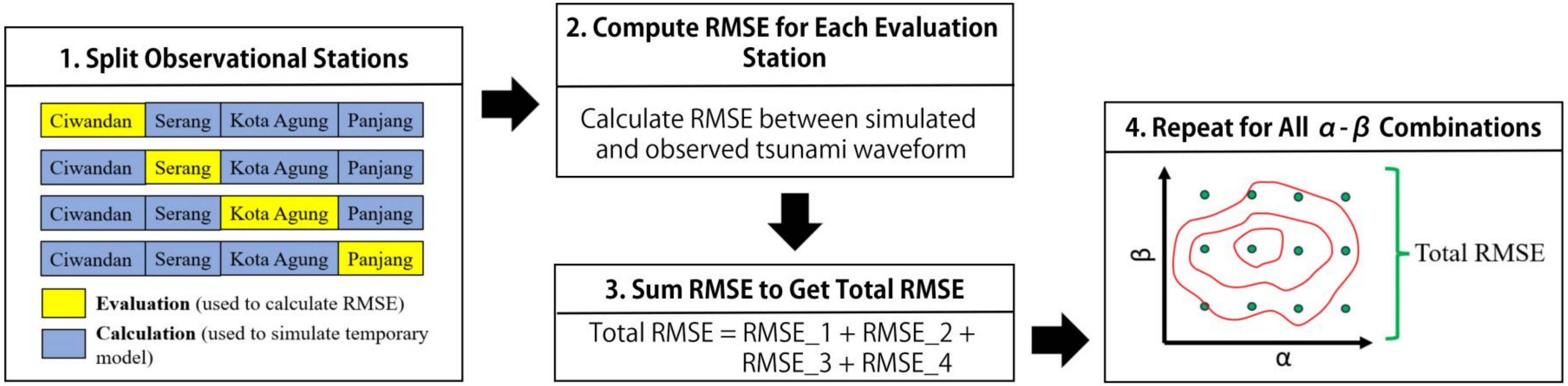

Figure 3.4. Flowchart illustrating the grid-search cross-validation procedure

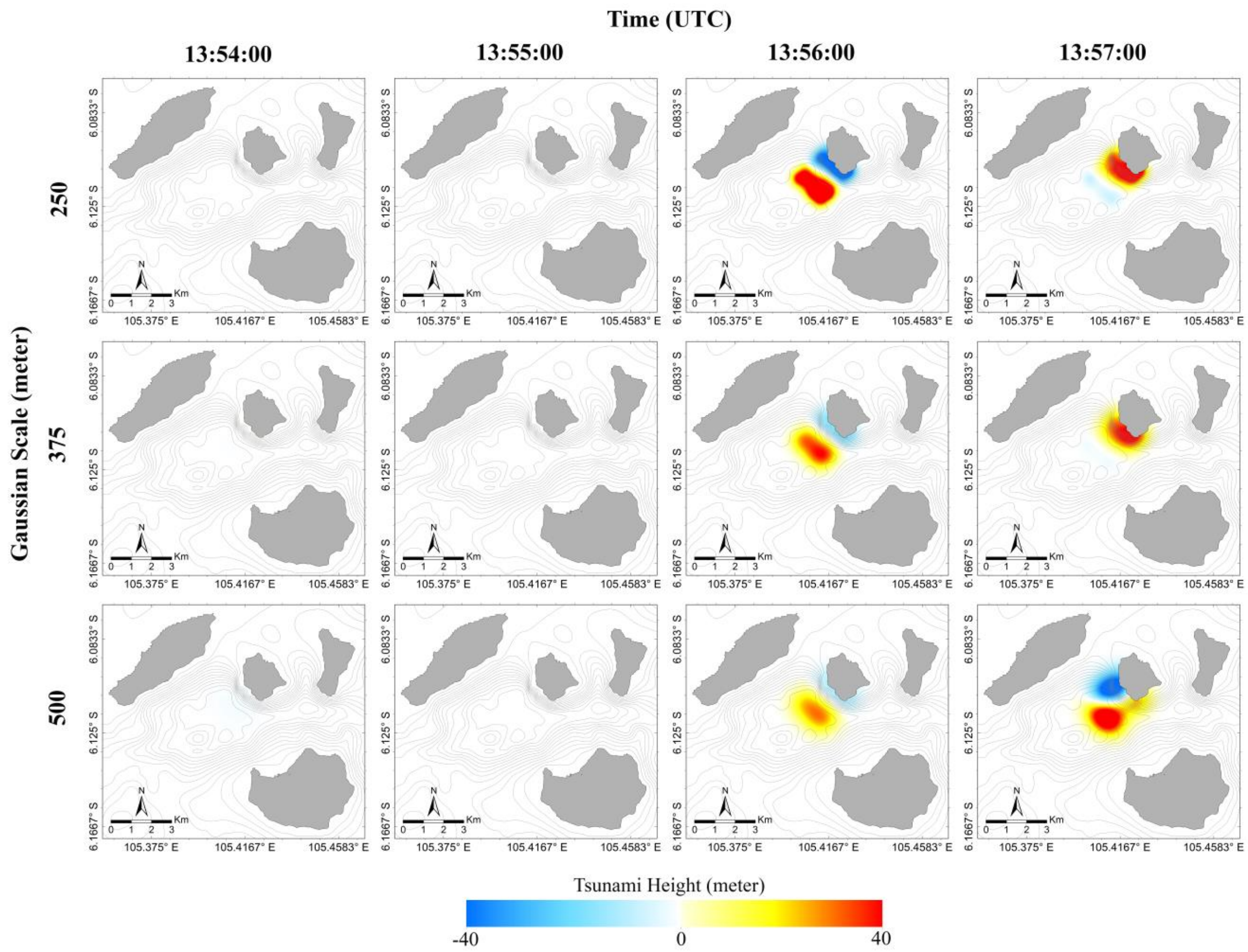

Figure 3.5. The initial sea surface displacement models developed from 12 scenarios with varying origin times and Gaussian scales. The gray lines represent depth contours with 20-meter intervals.

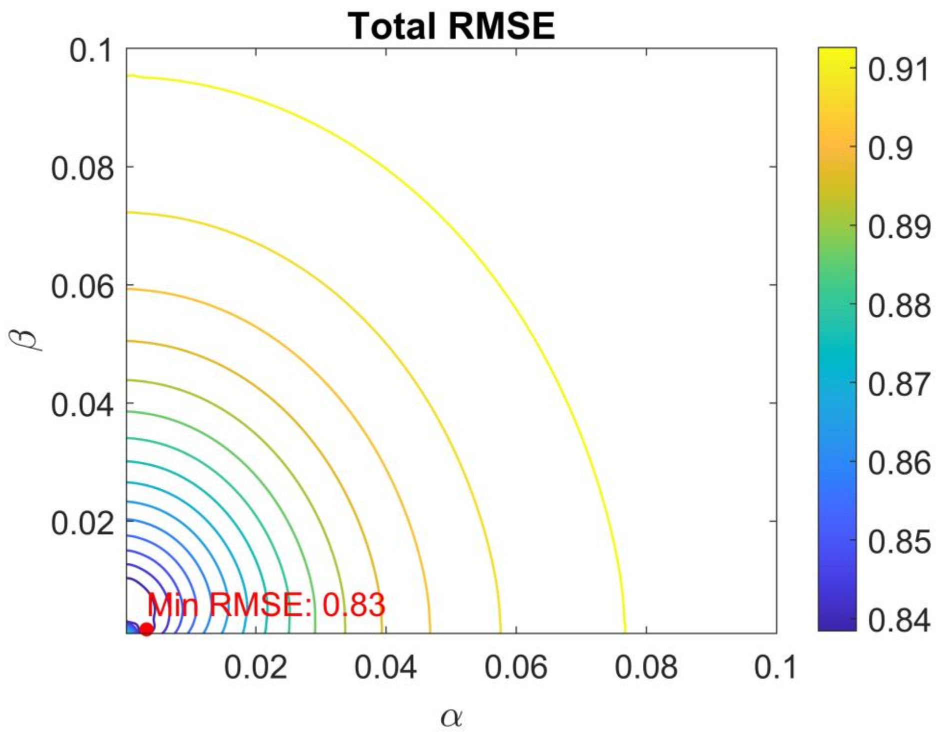

Figure 3.6a. Results of Grid search analysis using four tide gauge stations with a tsunami origin time of 13:56:00 UTC and a Gaussian scale of 250 m.

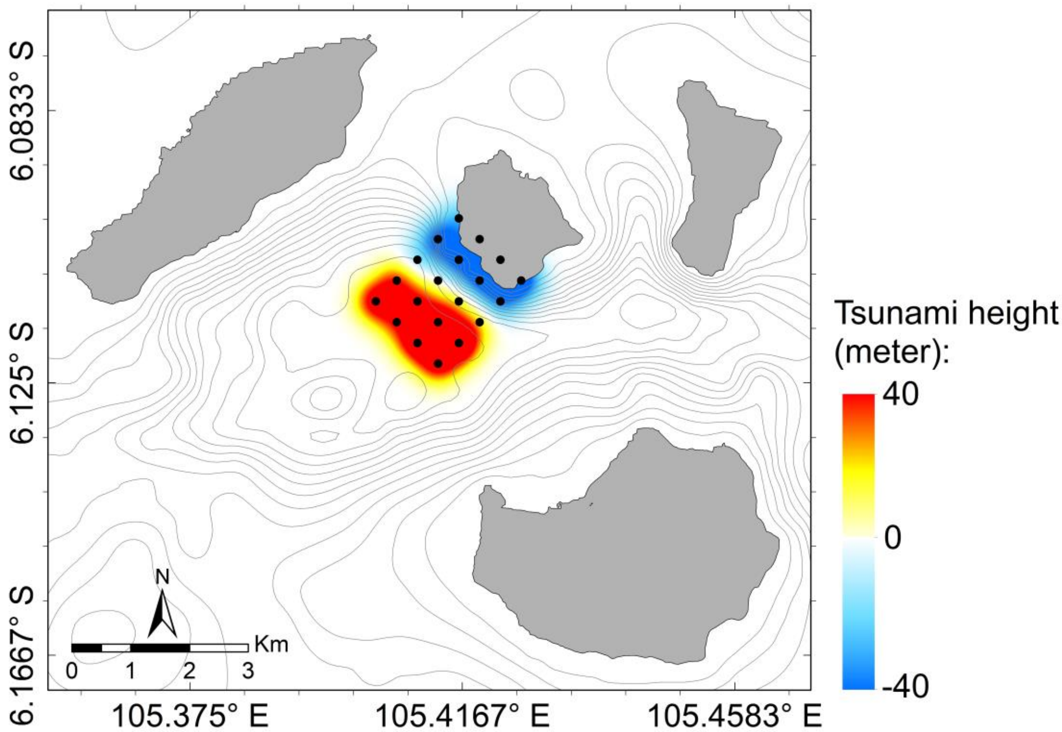

Figure 3.6b. Developed initial sea surface displacement using four tide gauge stations with a tsunami origin time of 13:56:00 UTC and a Gaussian scale of 250 m. The gray lines represent depth contours with 20-meter intervals.

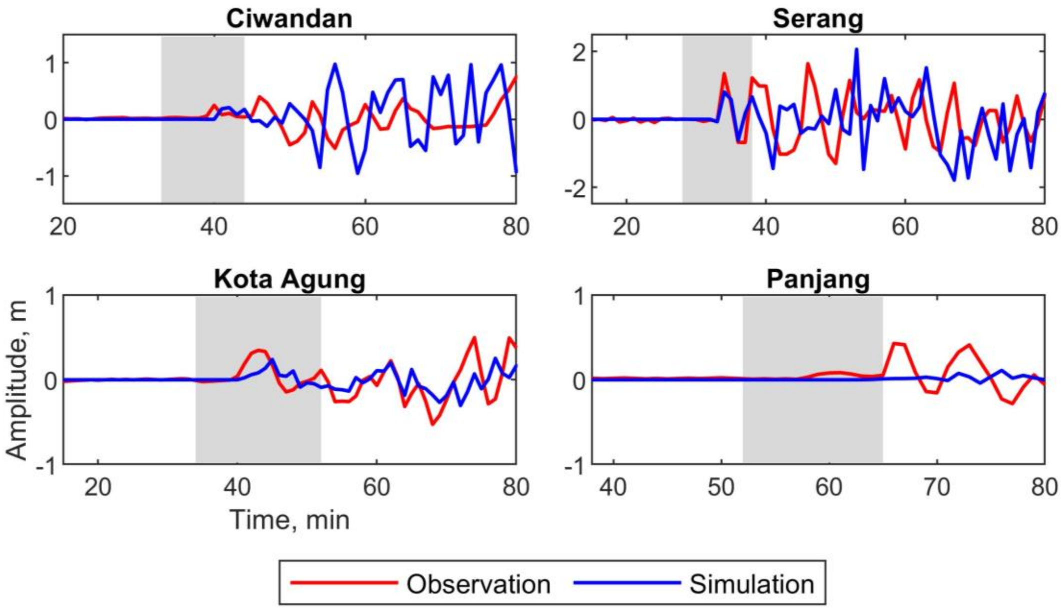

Figure 3.6c. Comparison of the observed and estimated waveforms using four tide gauge stations with a tsunami origin time of 13:56:00 UTC and a Gaussian scale of 250 m. The gray area indicates the time window for the inversion.

Table 1. Total RMSE values derived from 12 distinct scenarios

Time (UTC) / σ (meter)	13:54:00	13:55:00	13:56:00	13:57:00
250	0.92	0.92	0.63	0.73
375	0.92	0.92	0.71	0.74
500	0.93	0.92	0.74	0.79

3.4 Sensitivity analysis

To further evaluate the robustness and reliability of the inversion results, a comprehensive sensitivity analysis was conducted. As a preliminary test, 50% noise was added to the tsunami waveforms simulated at the four tide gauge stations, based on the previously estimated sea surface displacement model. These noise-added waveforms were then treated as observed data and subjected to inversion using the same method described in the earlier section, with the optimal hyperparameter values of α and β. As shown in Figure 3.7, the inversion was able to reasonably reproduce both the tsunami waveforms and the overall pattern of sea surface displacements. Figure 3.7a illustrates that the inverted displacement model retains the general structure characterized by two prominent adjacent uplift and subsidence regions. This result demonstrates that the inversion approach is relatively stable, even under the presence of considerable noise in the input data. As previously mentioned, the tsunami observations were recorded at four tide gauge stations that are sparsely distributed across the Sunda Strait (Figure 3.1). Despite the limited spatial resolution of the observation network, the data appear sufficient to capture the large-scale features of the tsunami source at Anak Krakatau.

To assess the resolution limits of the inversion framework, this study conducted a checkerboard test. A synthetic initial sea surface displacement pattern was constructed using alternating positive and negative anomalies arranged at a finer spatial scale than the original source model (Figure 3.8a). As in the previous test, 50% noise was added to the resulting tsunami waveforms before inversion. While the waveform fitting remained reasonably accurate (Figures 3.8b and 3.8c), the inverted sea surface displacement failed to reproduce the central part of the checkerboard pattern with sufficient fidelity. This result highlights a limitation in the resolving power of the inversion approach when using only four tide gauge stations. It suggests that the current observational network may be inadequate for resolving short-wavelength components of sea surface deformation. Nonetheless, the inversion method reliably reconstructs the dominant large-scale characteristics of the tsunami source under the linear wave assumption, even when the input data are significantly perturbed.

While the sensitivity tests demonstrated the overall stability and resolution capability of the inversion using four tide gauge stations, a notable misfit remained at one specific location, Panjang station. To further investigate the cause of this discrepancy and its influence on the inversion results, an additional analysis was conducted with a focus on this station. Significant mismatches in waveform fitting were encountered at Panjang tide gauge station during the inversion validation process. As shown in Figure 3.6c, the synthetic tsunami waveform exhibited a delay of approximately 6 minutes in arrival time compared to the observed data. Additionally, the simulated tsunami amplitudes during the initial phase were significantly lower than those recorded. This mismatch in both timing and amplitude hindered satisfactory agreement and raised concerns regarding the reliability of the Panjang station data in the inversion computation. One likely cause of these discrepancies is the quality of the bathymetric data in the nearshore region surrounding the Panjang station. The available bathymetric dataset may not accurately represent the complex underwater topography of the harbor and coastal areas, which are known to affect tsunami waveform characteristics.

To further evaluate the influence of Panjang station on the inversion results, a sensitivity analysis was conducted by re-running the inversion using tsunami waveforms from only the remaining three tide gauge stations: Ciwandan, Serang, and Kota Agung (Figure 3.9). The outcomes indicate that the exclusion of Panjang data did not significantly degrade the inversion performance. As shown in Figure 3.9b, the estimated initial sea surface displacement retained a similar structure to the target model (Figure 3.9a), characterized by large-scale subsidence and uplift patterns consistent with a volcanic flank collapse scenario. The corresponding waveform fitting at the three stations also demonstrated high agreement with the target data (Figure 3.9c), reinforcing the robustness of the inversion.

Following this result, the inversion was recomputed using only these three stations. The new solution yielded a total RMSE of 0.58, which is slightly better than the RMSE of 0.63 obtained using all four stations. Interestingly, the optimal hyperparameter values (α = 0.0032 and β = 0.0017) remained unchanged, further confirming the stability of the inversion scheme. The resulting sea surface displacement model and waveform fitting results (Figures 3.10a – 3.10c) closely resembled the one derived using four stations, indicating that the inclusion of Panjang station had minimal impact on the overall source estimation.

Waveform fitting at the remaining three stations also provided satisfactory results. At the Ciwandan station, the arrival time of the simulated tsunami lagged by approximately one minute compared to observations. However, this delay falls within the acceptable range, given the 1-minute sampling interval of the tide gauge records. The amplitude of the synthetic waveform was in good agreement with the observed data. At Serang station, excellent agreement was observed in both arrival time and amplitude. At Kota Agung station, while the amplitude was slightly underestimated, the arrival time and waveform shape were consistent with the observed tsunami.

To further verify the limited impact of the Panjang station, this study compared synthetic waveforms at Panjang generated from both inversion scenarios—using either four or three stations (Figure 3.11). The comparison revealed that both waveforms were nearly identical in amplitude and arrival time, with a consistent delay of approximately six minutes relative to the observed data. This persistent discrepancy, regardless of the number of stations used in the inversion, suggests that the waveform misfit at Panjang is not a result of model instability but more likely due to inaccuracies in the local bathymetric representation or other unmodeled site effects. Based on these findings, this study concludes that tsunami waveforms recorded at Ciwandan, Serang, and Kota Agung stations are sufficient to reliably estimate the initial sea surface displacement of the 2018 Anak Krakatau tsunami, and that the Panjang station may be excluded from the inversion without compromising model accuracy.

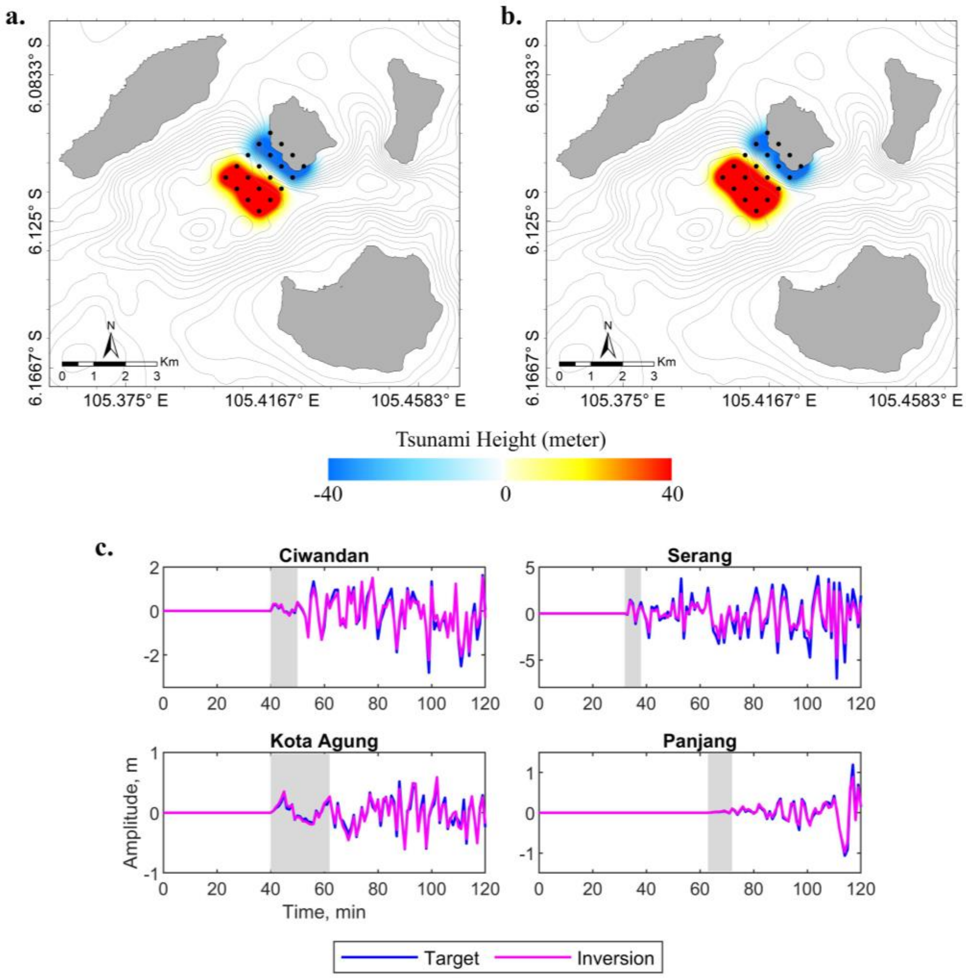

Figure 3.7. Sensitivity test using the initially estimated sea surface displacement model from this study; a. Target model; b. Inversion result; c. Waveform fitting: the gray area indicates the inversion time window. The gray lines in panels (a) and (b) represent depth contours with 20-meter intervals.

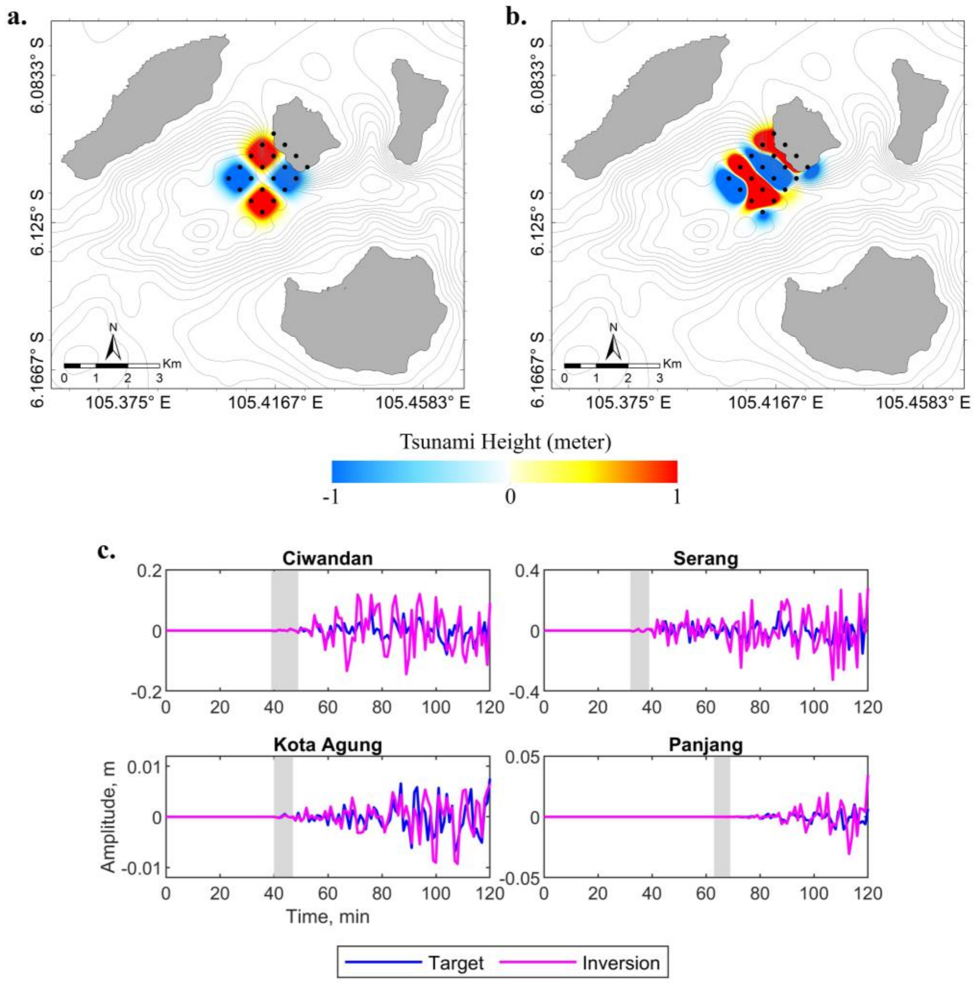

Figure 3.8. The checkerboard test; a. Target model; b. Inversion result; c. Waveform fitting: the gray area indicates the inversion time window. The gray lines in panels (a) and (b) represent depth contours with 20-meter intervals.

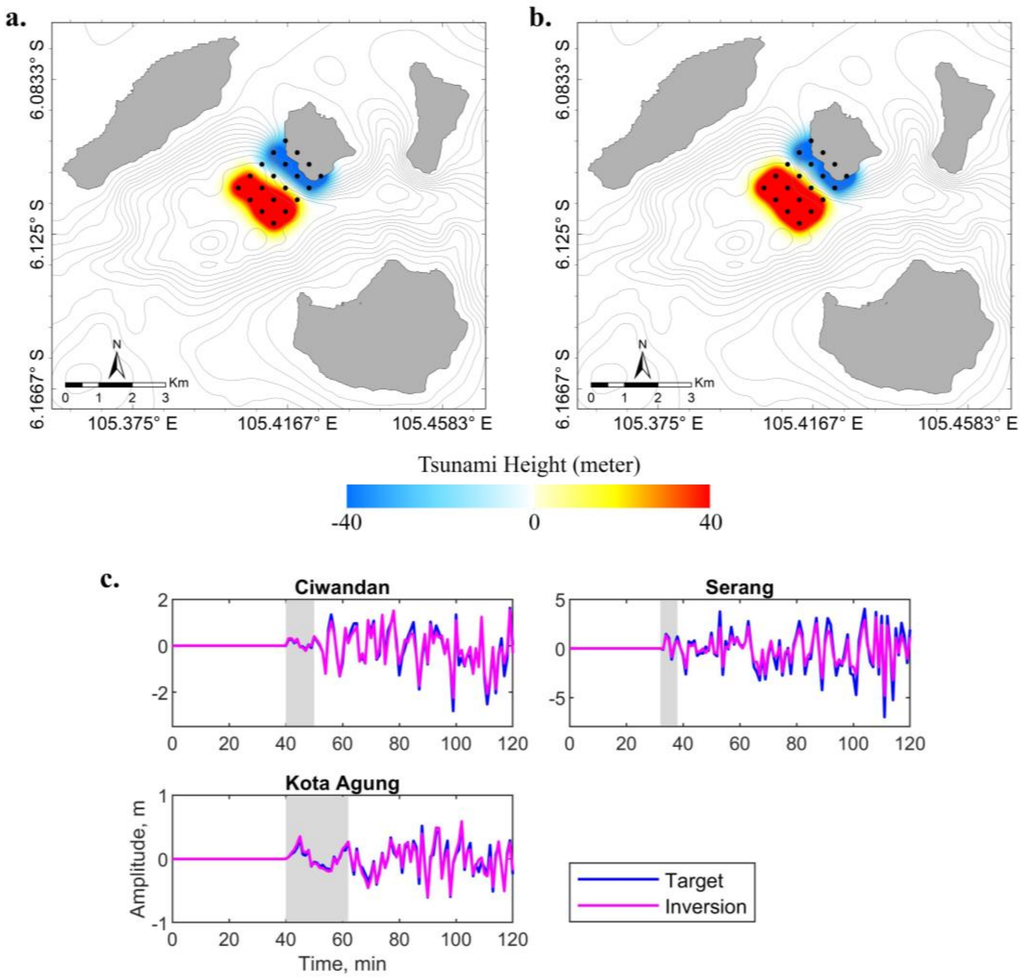

Figure 3.9. An additional sensitivity analysis using three tide gauge stations: a. Target model; b. Inversion result; c. Waveform fitting: the gray area indicates the inversion time window. The gray lines in panels (a) and (b) represent depth contours with 20-meter intervals.

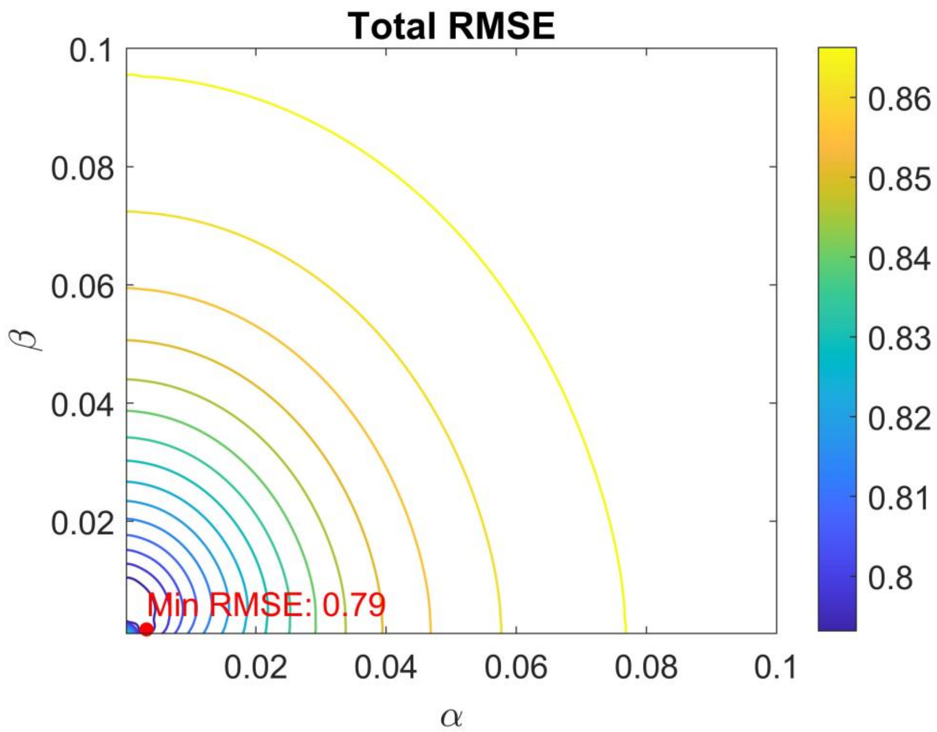

Figure 3.10a. Grid search analysis using three tide gauge stations with a tsunami origin time of 13:56:00 UTC and a Gaussian scale of 250 m.

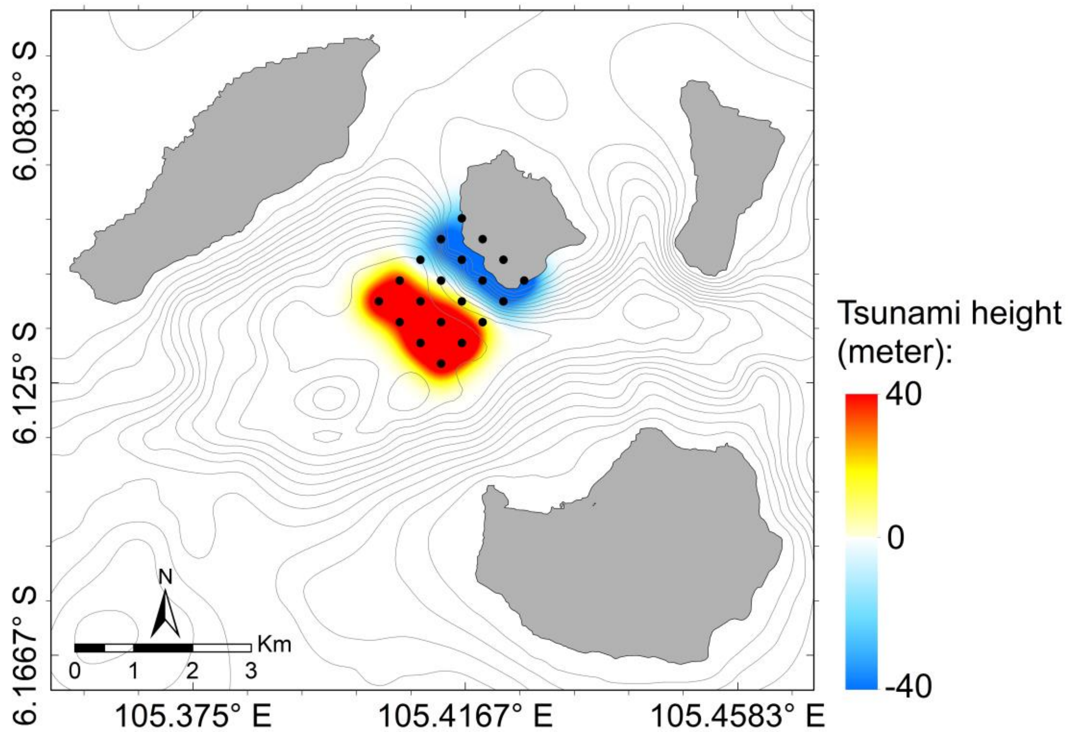

Figure 3.10b. Initial sea surface displacement using three tide gauge stations with a tsunami origin time of 13:56:00 UTC and a Gaussian scale of 250 m. The gray lines represent depth contours with 20-meter intervals.

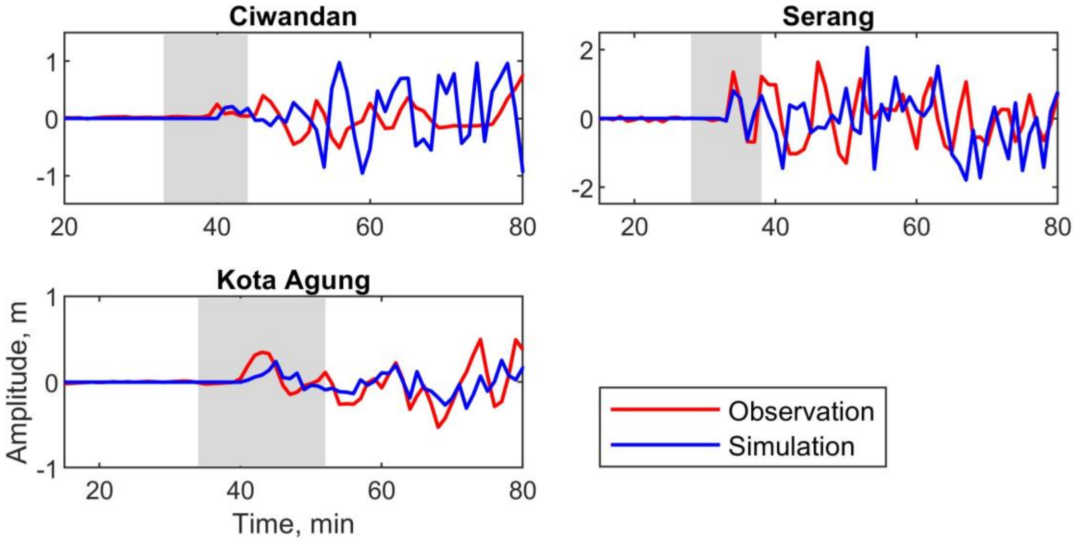

Figure 3.10c. Waveform fitting using three tide gauge stations with a tsunami origin time of 13:56:00 UTC and a Gaussian scale of 250 m. The gray area indicates the inversion time window.

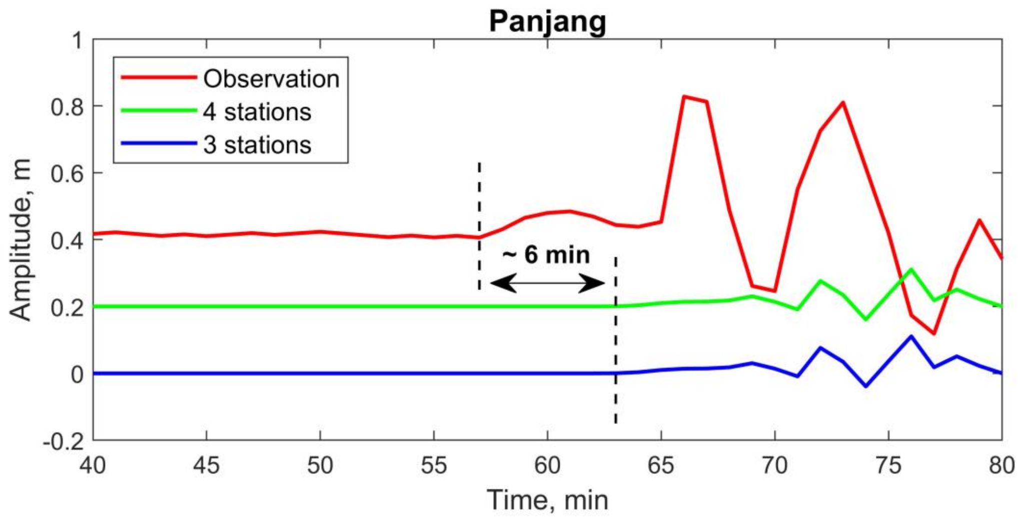

Figure 3.11. Comparison between tsunami and synthetic waveforms at Panjang station using data from 3 and 4 stations. The dashed line indicates tsunami arrival time.

3.5 Comparison of Static and Dynamic Source Scenario Tsunamis

While the previous sections have demonstrated the effectiveness and limitations of the inversion approach based on linear assumptions and observational constraints, it remains essential to evaluate how such static source models compare with more physically realistic dynamic scenarios. To this end, a comparative analysis was conducted using a dynamic source model that incorporates the physics of flank collapse and non-linear wave propagation. Specifically, the results of the inversion-based static source model were compared with those from a dynamic simulation developed by Ratnasari et al. (2023), which incorporates flank collapse dynamics using a non-linear dispersive model (hereafter referred to as Ratnasari et al.'s (2023) scenario). Figure 3.12 compares snapshots of tsunami propagation, profiles along control lines AA’ and BB’, and waveforms at the tide gauge stations simulated under the present scenario using the four stations and under Ratnasari et al.’s (2023) scenario. It should be noted that the tsunamis under these two scenarios simulate distinct numerical conditions; hence, the results do not necessarily have to match. Nonetheless, these comparisons are useful for demonstrating the consistency of the results obtained in this study with those derived from numerical modeling that accounted for the flank collapse mechanism during their simulations.

The time of zero in the present scenario and that in Ratnasari et al. (2023) have different meanings: the former is for the origin time of the tsunami generation and the latter is for the initiation time of the collapse. To account for this discrepancy, a time shift (Δt) was introduced to align the two scenarios, and its value was empirically determined as 0.37 minutes through trial and error. As shown in Figures 3.12, the results at a time (t) (2, 3, 4, and 5 minutes) were presented for the present scenario, while those at t + Δt were shown for Ratnasari et al.'s (2023) scenario.

According to Figures 3.12a – 3.12d, the snapshots and spatial profiles of the simulated tsunamis between the present scenario and Ratnasari et al.'s (2023) scenario were reasonably similar. High-frequency fluctuations appeared in Ratnasari et al.'s (2023) scenario, which considered the collapse dynamics with non-linear and wave dispersion effects. Additionally, reflective waves from the surrounding islands could contribute to generating fluctuations. However, some high-frequency fluctuations with larger amplitudes also appeared in the present scenario. In this study, linear long-wave equations were applied to simulate the propagation of the estimated source model, which did not contain high-frequency components. Therefore, these fluctuations were likely caused by waves reflected from the islands. Once such fluctuations appear, they tend to persist longer in simulations using linear long wave equations than non-linear long wave or dispersive equations because wave dispersion, dissipation, and diffusion effects are omitted in the simulation. This likely explains why high-frequency fluctuations with large amplitudes were observed in the present scenario. However, the wave patterns generated in the present scenario and those of Ratnasari et al. (2023) appear moderately similar for low-frequency components.

An in-depth analysis was conducted to investigate the characteristics of the initial sea surface displacement. Tsunami waveforms simulated using the non-linear dispersive model under the dynamic collapse scenario of Ratnasari et al. (2023) were treated as observed data for the inversion. A noise level of 0% was assigned to these waveforms. Based on this approach, an initial sea surface displacement model corresponding to Ratnasari et al.'s (2023) dynamic scenario was constructed (Figure

3.13). Following the previous investigation, several tsunami origin times were tested: 13:54:00, 13:55:00, 13:56:00, and 13:57:00 UTC. The waveform fitting results at the tide gauge stations in Ciwandan, Serang, Kota Agung, and Panjang indicated that the tsunami origin time at 13:56:00 UTC yielded the most optimal results (Figure 3.13b). Furthermore, Figure 3.13a qualitatively shows that a significant positive displacement is concentrated around Mount Anak Krakatau, consistent with the location of the static source model developed in this study for flank collapse. The volume of the water surface displacements for the scenario with an occurrence time of 13:56 UTC was 0.12 km3, which agreed with the collapse volume of 0.24 km3 for the Anak Krakatau in Ratnasari et al. (2023) at the order of magnitude but deviate from its value.

The comprehensive investigations presented in previous sections demonstrate that a reasonable static sea surface displacement model can be developed if it is relatively large. However, the calculated volume of 0.12 km^3 is significantly smaller than 0.24 km^3 by a factor of two. These results suggest that non-linear dispersive wave characteristics influence the primary tsunami waveforms simulated under the Ratnasari et al. (2023) scenario. In particular, the non-linear effects of the tsunami near the source area were non-negligible. This may explain why the waveforms were not reasonably reproduced after the inversion time. This study demonstrated that a static source model developed for the Anak Krakatau event (non-seismic tsunami event) within the framework of linear inversion did not have unreasonable characteristics; however, future studies should investigate and quantify the impacts of non-linear and dispersion effects.

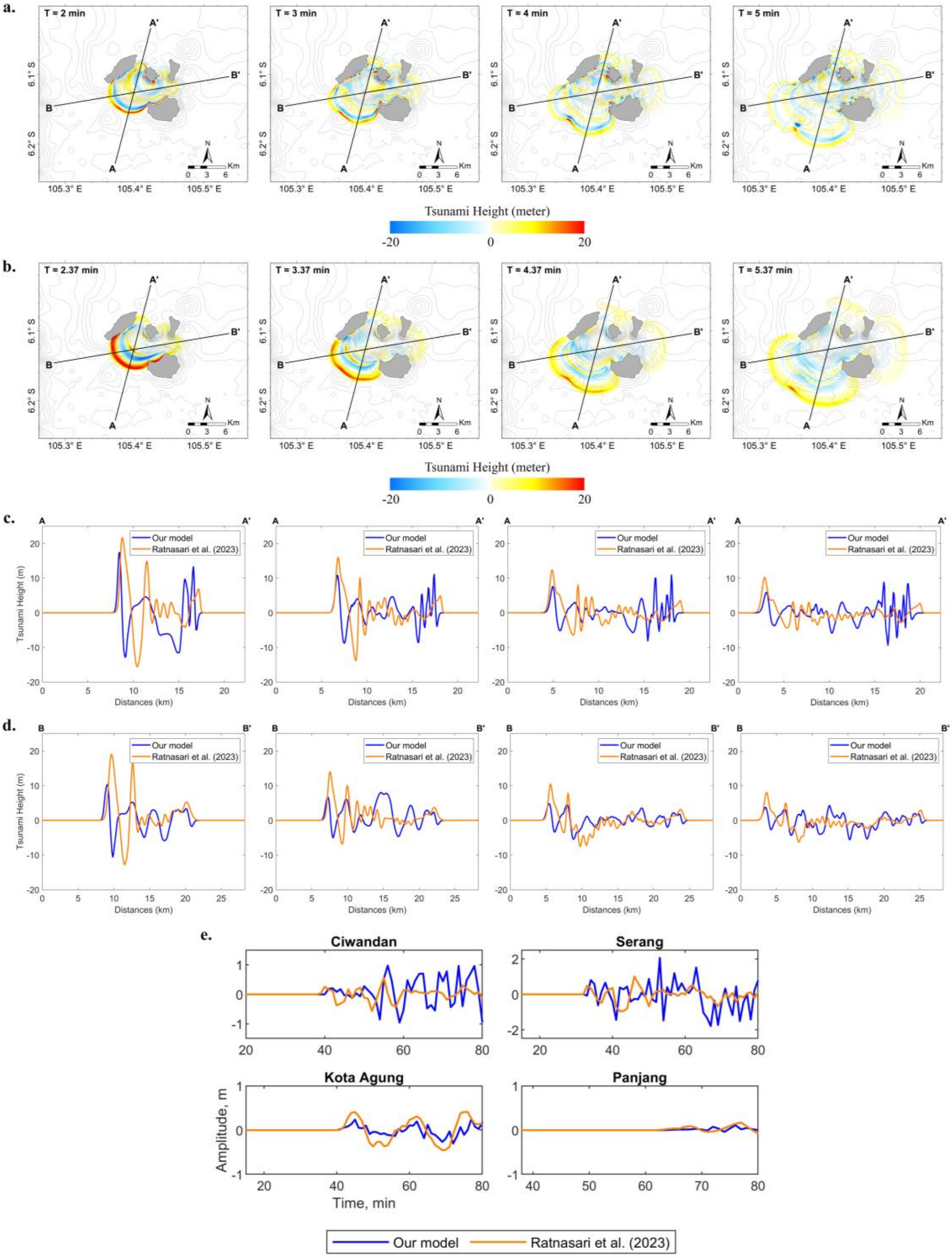

Figure 3.12. a. Snapshot from the present scenario; b. Snapshot of Ratnasari et al.'s (2023) scenario; c. Tsunami height along the AA' line; d. Tsunami height along the BB' line; e. Synthetic waveforms at four tide gauge stations from both models. The gray lines in panels (a) and (b) represent depth contours with 20-meter intervals.

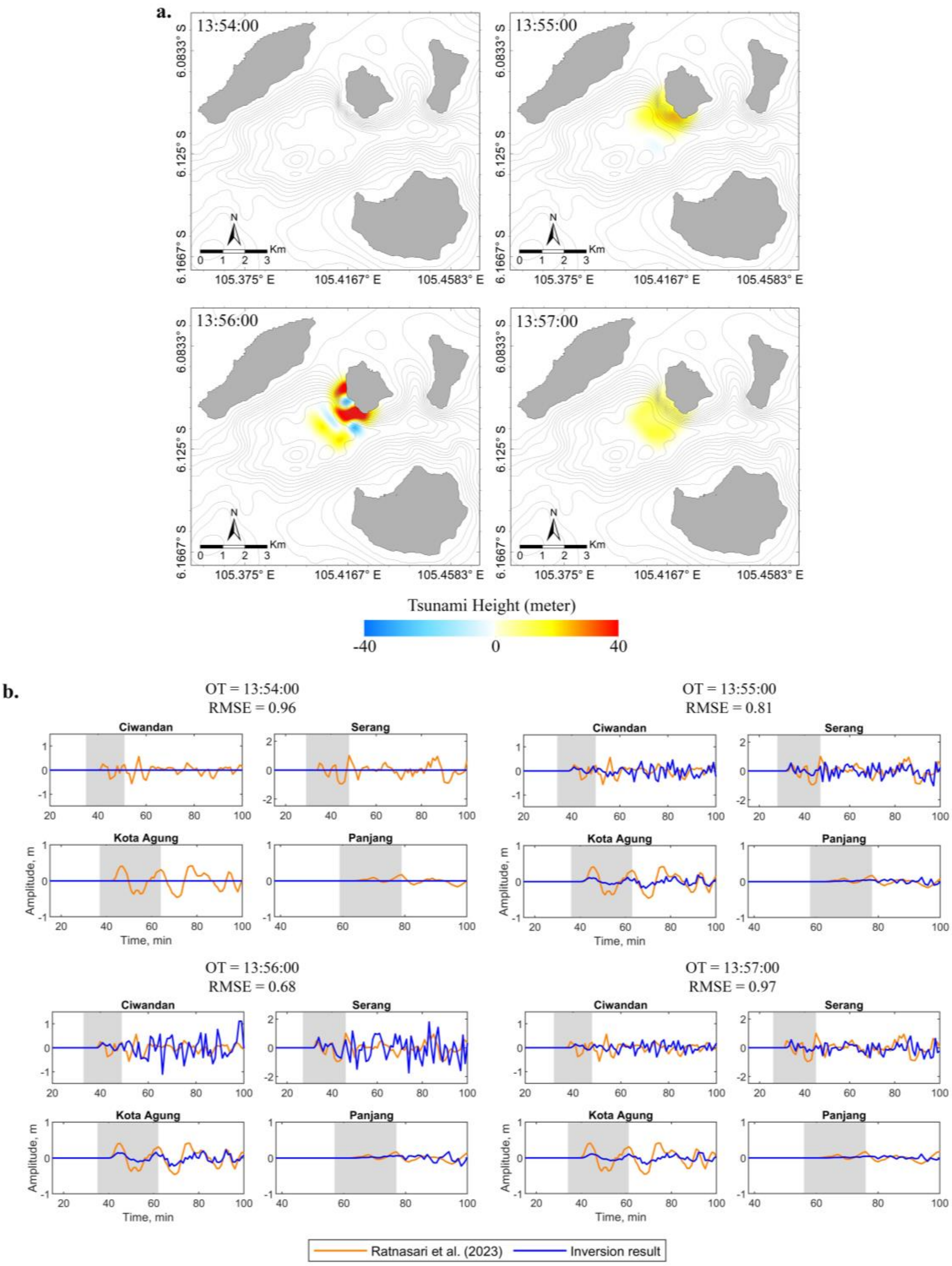

Figure 3.13. a. The initial sea surface displacement models; b. Waveform fitting results for varying origin times. The gray lines in panel (a) represent depth contours with 20-meter intervals.

3.6 Summary of Source Modeling for the 2018 Anak Krakatau Tsunami

This chapter presented the development and evaluation of a static tsunami source model for the 2018 Anak Krakatau non-seismic tsunami using a waveform inversion method based on tide gauge observations in the Sunda Strait. By employing a two-dimensional Gaussian representation for unit sources, the optimal model was obtained with a tsunami origin time of 13:56:00 UTC and a Gaussian width (σ) of 250 meters. The inversion results successfully reproduced the key characteristics of the observed tsunami waveforms, both near the source area and at tide gauge stations. The displaced water volume was calculated to be approximately 0.19 km^3, which is consistent in order of magnitude with the collapse volume estimates reported in previous studies. Although this estimated volume was slightly lower, the underestimation is likely attributable to the omission of non-linear and dispersive effects in the linear modeling framework.

Sensitivity analyses confirmed the robustness of the inversion method under significant synthetic noise and with a limited number of observation stations. A persistent waveform mismatch at the Panjang station was attributed to potential inaccuracies in nearshore bathymetric data. However, excluding this station from the inversion improved the RMSE value and preserved the overall spatial structure of the estimated sea surface displacement. A comparison with a dynamic source model that incorporates flank collapse dynamics and non-linear dispersive wave propagation further supported the validity of the inversion-based static model, particularly in capturing the dominant low-frequency tsunami features.

These findings demonstrate that static source modeling based on waveform inversion is an effective approach for rapidly estimating tsunami source characteristics during non-seismic events. To enhance the accuracy and reliability of such models, future research should focus on investigating the relationship between physical parameters of volcanic flank collapse, such as sediment inflow volume and flow velocity, and the resulting sea surface deformation, while also incorporating nonlinear and dispersive effects to better capture the complex dynamics of tsunami generation. Moreover, the integration of high-resolution bathymetric data and tsunami waveforms with finer temporal resolution is essential to improve inversion accuracy and support a more comprehensive understanding of tsunami generation mechanisms.

Chapter 4

Tsunami Source Modeling in a Combined Earthquake-Submarine Landslide Event

4.1 Overview of the 2024 Noto Tsunami

On January 1, 2024, a significant earthquake struck the Noto Peninsula region in Japan. According to the Japan Meteorological Agency (JMA), the earthquake was centered at 37°29.7’N latitude and 137°16.2’E longitude, with a hypocentral depth of approximately 16 km and a magnitude of M_{JMA} 7.6. The origin time was recorded at 7:10:22.5 UTC. The focal mechanism indicated a reverse faulting type, with two possible fault planes: the first with a strike of 47°, dip of 37°, and rake of 100°; and the second with a strike of 215°, dip of 54°, and rake of 82°. These orientations suggest dominant northeast–southwest (NE–SW) tectonic deformation, consistent with the regional tectonic trend.

The Noto Peninsula is known for its high seismic activity, which results from the complex interaction between the Eurasian, Amurian, and Okhotsk plates (Nishimura, Hiramatsu, & Ohta, 2023). The 2024 Noto Earthquake was not an isolated event but rather the culmination of an earthquake swarm that had persisted since late 2020. During this period, more than 20,000 earthquakes were recorded in the region, indicating an unusual pattern of stress accumulation and release, likely involving mechanisms such as pre-slip, aseismic slip, and elevated pore-fluid pressure within the crust. This prolonged swarm activity is also suspected to have contributed to the occurrence of the 2023 Suzu Earthquake (Mw 6.5). The 2024 mainshock (Mw 7.6) is believed to have ruptured a reverse fault situated above a parallel fault responsible for the May 2023 Suzu Earthquake (Mw 6.5) (Yoshida et al., 2023; Peng et al., 2025). This sequence of events highlights the structural complexity of the active fault systems in the Noto Peninsula.

Historically, this region has experienced several significant earthquakes. Notably, the 1993 Noto-Hanto Oki Earthquake (Mw 6.6) and the 2007 Noto-Hanto Earthquake (Mw 6.7), both recorded in the United States Geological Survey (USGS) catalogue. These events generated minor tsunamis: in 1993, tsunami waves with a maximum amplitude of approximately 0.5 meters were observed at Wajima and Naoetsu tide gauge stations (Abe & Okada, 1995); in 2007, maximum wave heights of 23 cm and 16 cm were recorded at Noto and Kanazawa Port, respectively (Namegaya & Satake, 2008). In contrast, the 2024 Noto Earthquake generated a more substantial tsunami. Reports by Heidarzadeh et al. (2024) and Yuhi et al. (2024) documented inundation and run-up heights of approximately 3 meters in Toyama Prefecture. These values increased northward toward Niigata Prefecture, where run-up heights of about 6 meters were measured along the Joetsu coast. The epicenter of the 2024 Noto Earthquake, along with the epicenters of several historically significant events, is shown in Figure 4.1. This phenomenon underscores that, although the Noto Peninsula is not located directly on a major plate boundary such as the Pacific subduction zone, it remains tectonically active due to complex plate interactions. Geologically, this region lies within the back-arc zone of northeastern Japan (Okamura et al., 1995), dominated by the convergence of the Eurasian and Amurian plates and influenced by the dynamics of the Okhotsk Plate to the northeast (Nishimura, Hiramatsu, & Ohta, 2023).

Several studies have been conducted to further investigate the characteristics of the tsunami generated by the 2024 Noto Peninsula Earthquake. Fujii and Satake (2024b) conducted a joint inversion analysis using tsunami waveform data from six offshore wave gauges and twelve coastal tide gauges, combined with GNSS coseismic deformation data from 53 stations distributed around the Noto Peninsula. Their objective was to estimate the slip distribution and seismic moment of the 2024 Noto Earthquake by testing two fault models: the Japan Sea Earthquake and Tsunami Research Project (JSPJ) model and the Ministry of Land, Infrastructure, Transport and Tourism (MLIT) model. In the JSPJ model, the main slip was concentrated on three subfaults, namely NT4, NT5, and NT6, located along the northern coast of the peninsula. The maximum slip reached approximately 3.5 meters, indicating a southeastward-propagating reverse fault rupture. In contrast, the adjacent subfaults NT2 and NT3, which dip in the opposite direction, did not exhibit significant slip during the mainshock, although a large aftershock (M_{JMA} 6.1) occurred in that area. This suggests that NT2 and NT3 may still retain seismic potential and could produce a future tsunamigenic earthquake, possibly up to Mw 7.1. A similar contrast was observed in the MLIT model, where fault segment F43 was identified as the primary rupture zone, while F42 remained unbroken. Among the two models, the inversion results from the JSPJ configuration provided better agreement with observed tsunami waveforms in terms of both amplitude and arrival time. Therefore, the JSPJ model was adopted in this study as the basis for earthquake source modeling. The model includes seven subfaults: NT2 through NT6, NT8, and NT9, extending along the offshore segment of the northern Noto Peninsula. Each subfault is defined by specific source parameters, such as centroid location, fault length and width, depth, strike, dip, rake, and inverted slip value.

Masuda et al. (2024) emphasized the importance of constructing a more realistic tsunami source model for the 2024 event, considering the complexity of submarine active fault systems. Far offshore segments are difficult to identify accurately using land-based observational inversion. In their study, four different fault models were evaluated to simulate tsunami propagation and inundation. Among them, the most consistent scenario involved the simultaneous rupture of two active fault systems, which explained the majority of observed tsunami heights and inundation patterns. However, some discrepancies remained, indicating that the tsunami mechanism was more complex than simple tectonic rupture. One notable finding was that tsunami propagation did not follow a concentric pattern but was strongly influenced by bathymetric heterogeneity, as evident in the impact pattern in Iida Bay. The study also suggested the possible contribution of a submarine landslide in southern Toyama Bay to the amplification of tsunami waves. These findings reinforce the necessity for an integrated approach combining numerical tsunami modeling with paleo-tsunami studies to better understand complex tsunami sources, particularly in the eastern margin of the Japan Sea.

Yamanaka et al. (2024) focused specifically on local tsunami amplification in Iida Bay, a small bay on the Noto Peninsula that experienced severe coastal damage. Unlike other studies relying on instrumental data, this research used video recordings to extract tsunami waveforms within the bay. The study found that tsunami amplification in Iida Bay was not caused by the initial wave but rather by subsequent waves propagating along the coast (alongshore waves). Some of these waves, including edge waves arriving from opposite directions, intersected at a specific point within the bay, producing constructive interference and leading to maximum inundation approximately 20 minutes after the first wave's arrival. This study underscores the importance of considering coastal wave interactions and directionality in tsunami modeling, especially for small embayments like Iida Bay (~20 km), which are often overlooked in large-scale models. More broadly, the findings suggest that tsunamis in the Japan Sea, characterized by shorter wavelengths compared to those generated by major subduction zones, may cause more pronounced local amplification effects.

Tajima et al. (2024) conducted a field survey and visual analysis using CCTV footage to assess tsunami characteristics, especially in regions distant from the epicenter, including river mouths and coastal areas around Toyama Bay. The study showed the potential presence of additional tsunami sources (multi-source tsunamis) within Toyama Bay. A particularly important finding was the occurrence of an early negative water level peak just a few minutes after the earthquake, with earlier arrival times in the southern part of Toyama Bay. This pattern, which cannot be explained by a single-source tectonic tsunami, supports the hypothesis of multiple tsunami sources within the bay. Tsunami back-propagation analysis of arrival times further substantiated the interpretation that the 2024 tsunami involved complex, multi-source generation mechanisms.

Yanagisawa, Abe, and Baba (2024) provided compelling evidence that non-seismic tsunamis generated by submarine landslides played a significant role in amplifying the tsunami induced by the 2024 Noto Earthquake. By integrating observational data from tide gauges, wave gauges, video recordings, and tsunami trace heights along the Toyama Bay coast, they validated an integrated landslide–tsunami model. Their results indicated that five submarine landslides along underwater canyons in Toyama Bay successfully reproduced observed tsunami waveforms and run-up heights. These landslides were estimated to have occurred approximately 50 seconds after the mainshock, coinciding with the peak ground shaking in Toyama Bay, supporting the hypothesis that intense seismic shaking triggered submarine slope failures. Most notably, the landslide-generated tsunami waves amplified the tsunami height by approximately 30% compared to the earthquake-only source. The study highlights the need to account for compound tsunami sources in hazard assessment, particularly in regions with complex bathymetric features and high submarine landslide potential.

Mulia et al. (2024) also presented strong evidence that submarine landslides contributed significantly to the tsunami recorded in Toyama Bay following the 2024 Noto Earthquake. While earthquake-only tsunami simulations estimated arrival times at around 20 minutes post-event, observed tsunami waves arrived within 2–3 minutes, indicating the involvement of additional non-seismic sources. Through spectral and wavelet analyses, the study identified dominant tsunami periods of 5, 14, and 32 minutes. The shorter periods (5 and 14 minutes) were attributed to submarine landslide sources. A potential landslide site was estimated to lie about 4 km offshore from Toyama City, with a length of approximately 3 km. The combined earthquake–landslide model more accurately reproduced the observed waveforms compared to the earthquake-only model. This study highlights the critical need to consider multi-source tsunami generation, especially in geologically complex regions like Toyama Bay. Furthermore, it stresses that tsunamis generated by submarine landslides can arrive with very short lead times, posing a serious challenge for conventional tsunami early warning systems. As such, the study makes a valuable contribution to raising awareness of local tsunami hazards in the southern margin of the Japan Sea that may not be fully explained by tectonic sources alone.

Based on prior studies, it is evident that the 2024 Noto Earthquake generated a substantial tsunami that caused severe damage along the coastal areas of the Noto Peninsula and surrounding regions. However, multiple field surveys and waveform analyses have shown that the tsunami's characteristics cannot be fully explained by seismic sources alone. Observed discrepancies in arrival times, waveform shapes, and inundation patterns, particularly in Toyama Bay, suggest the contribution of additional non-seismic mechanisms such as submarine landslides. This interpretation is further supported by several independent studies that reported anomalous wave periods and unusually early arrivals, which are inconsistent with tsunamis generated solely by tectonic faulting (Mulia et al., 2024).

Given this background, the present study introduces a hypothetical tsunami scenario that treats the 2024 Noto event as a representative case of a compound-source mechanism involving both an earthquake and a submarine landslide. It is important to note that this study does not attempt to directly reconstruct the 2024 tsunami from observational data. Instead, it develops a numerically controlled synthetic scenario that reflects the main features documented in the literatures. This approach is motivated not only by the inherent difficulty in isolating tsunami contributions from different source processes in the actual event but also by the ongoing uncertainty surrounding the definition of a definitive earthquake source model for the 2024 event (Yamanaka et al., 2024). Additional complicating factors include the near-simultaneous generation of waves from fault rupture and submarine landslide activity, overlapping wave periods from different sources, and the possible occurrence of multiple submarine landslides in rapid succession. These complexities make it challenging to distinguish individual source effects using observational data alone.

To address these challenges, the study adopts a synthetic modeling framework that systematically examines three distinct source scenarios: an earthquake-only scenario, a landslide-only scenario, and a compound-source scenario that combines both. For each case, tsunami waveforms are numerically simulated and compared with a reference model that approximates the key characteristics of the 2024 Noto tsunami. Inversion techniques are then applied to the synthetic data to estimate the initial sea surface displacement and to evaluate the feasibility and accuracy of source reconstruction across different generation mechanisms. Ultimately, this framework contributes to the development of more reliable tsunami source estimation strategies and supports the improvement of real-time forecasting capabilities in regions prone to both tectonic activity and submarine landslides, such as the eastern margin of the Japan Sea.

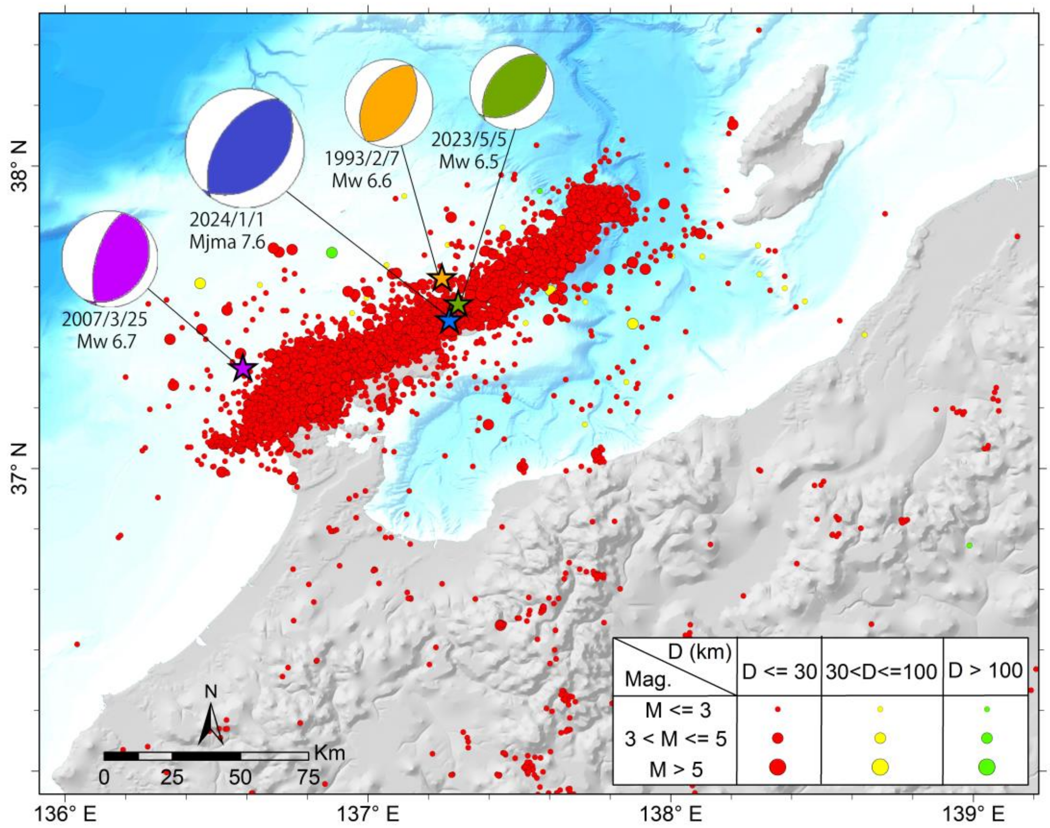

Figure 4.1. Epicenter of the 2024 Noto Earthquake and Distribution of Earthquakes Occurring Within Seven Days After the Mainshock, Along with Epicenters of Historically Significant Earthquakes in the Region

4.2 Synthetic Tsunami Waveforms and Bathymetry Data for Simulation

Building on the compound-source framework introduced in the previous section, this study employs synthetic tsunami waveforms as input for numerical simulation and inversion analysis. The synthetic dataset was constructed to reflect the main characteristics of the 2024 Noto tsunami event under controlled modeling conditions, allowing for systematic evaluation of different source contributions. These waveforms were used to examine how the presence of multiple generation mechanisms, such as fault rupture and submarine landslides, may influence the accuracy of initial sea surface displacement estimates derived from inversion.

Synthetic tsunami signals were calculated at eleven tsunami monitoring stations located along the western coast of Japan. These included seven wave gauge (WG) stations at Niigataoki, Naoetsu, Toyama, Wajima, Kanazawa, Fukui, and Tanaka, and four tide gauge (TG) stations at Toyama, Sado, Saigo, and Fukaura. This station configuration provided broad spatial coverage for capturing the effects of complex source interactions on tsunami propagation. The station distribution is illustrated in Figure 4.2.

To support the simulations, bathymetric data were sourced from two main datasets. First, regional-scale bathymetry compiled by Chikasada (2020) was used and resampled to a grid resolution of 9 arcseconds. Second, high-resolution data from the M7000 Digital Bathymetric Chart were incorporated and resampled to 3 arcseconds in areas near the assumed tsunami source. This finer resolution is essential for accurately capturing steep and irregular seafloor features, which is particularly important for modeling tsunamis generated by submarine landslides. A combined visualization of the tsunami stations and bathymetric datasets is presented in Figure 4.2.

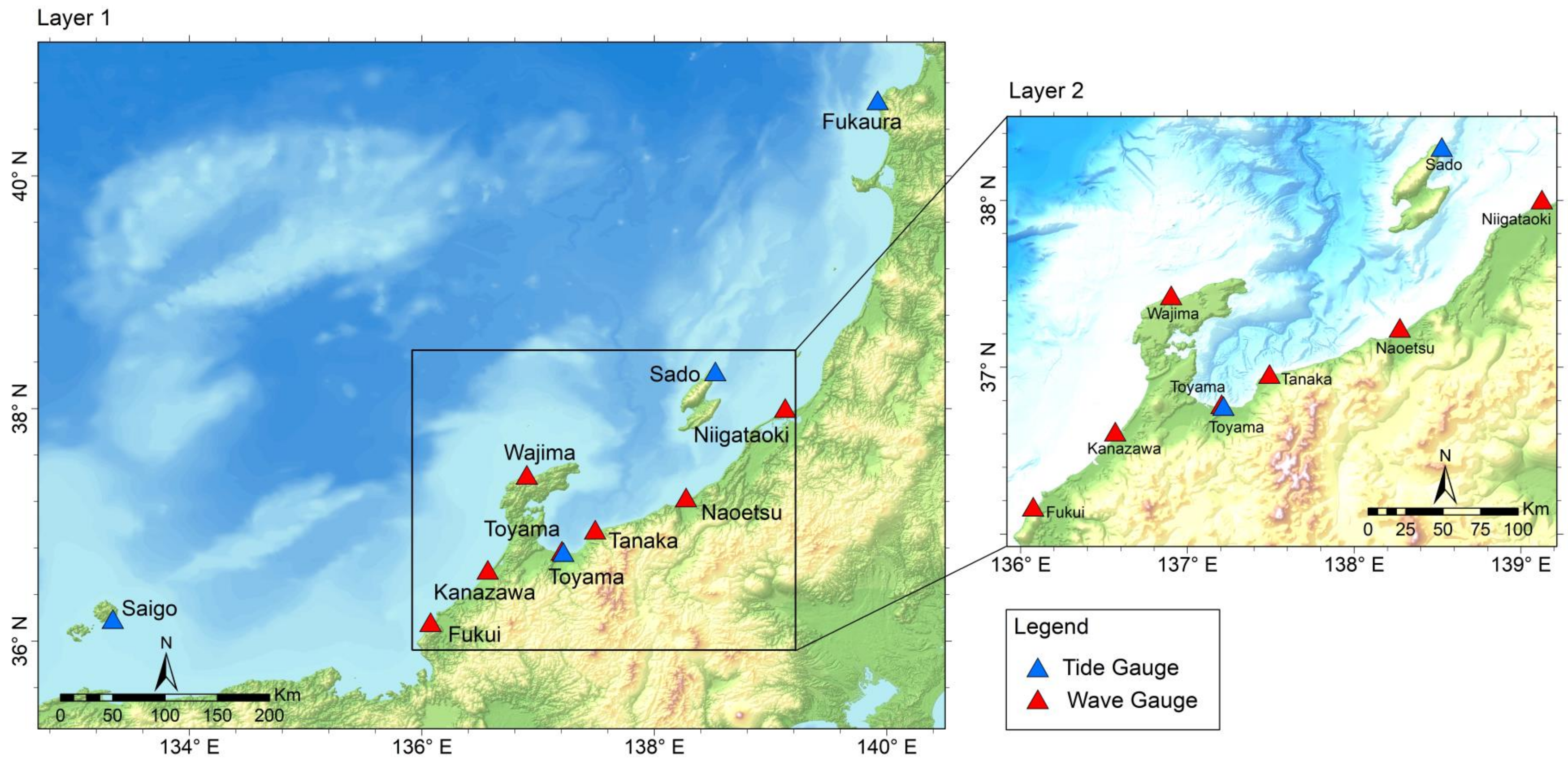

Figure 4.2. Distribution of tsunami monitoring stations and bathymetry used in this study. Blue triangles indicate tide gauge stations, and red triangles indicate wave gauge stations.

4.3 Tsunami Source Scenarios for Numerical Modeling

This section presents scenario-based numerical modeling aimed at investigating the plausible source mechanisms responsible for the 2024 Noto tsunami. Three distinct source scenarios are examined in this study: an earthquake-only scenario, a submarine landslide-only scenario, and a compound scenario that combines both earthquake and landslide mechanisms. These scenarios are constructed under controlled conditions to evaluate the individual and combined effects of the sources on tsunami generation, propagation, and resulting waveform characteristics.

All tsunami simulations were performed using the JAGURS software (Baba et al., 2015; 2017), which solves the nonlinear long-wave (NLLW) equations to accurately simulate tsunami propagation, including nonlinear effects that become prominent in shallow coastal areas. The governing equations used in this study are as follows:

$$\frac{\partial M}{\partial t} + \frac{1}{R\sin\theta}\frac{\partial}{\partial\varphi}\left(\frac{M^2}{H+\eta}\right) + \frac{1}{R}\frac{\partial}{\partial\theta}\left(\frac{MN}{H+\eta}\right) = -\frac{g(H+\eta)}{R\sin\theta}\frac{\partial\eta}{\partial\varphi} - fN - \frac{gn^2}{(H+\eta)^{7/3}}M\sqrt{M^2+N^2} \tag{4.1}$$

$$\frac{\partial N}{\partial t} + \frac{1}{R\sin\theta}\frac{\partial}{\partial\varphi}\left(\frac{MN}{H+\eta}\right) + \frac{1}{R}\frac{\partial}{\partial\theta}\left(\frac{N^2}{H+\eta}\right) = -\frac{g(H+\eta)}{R}\frac{\partial\eta}{\partial\theta} - fM - \frac{gn^2}{(H+\eta)^{7/3}}M\sqrt{M^2+N^2} \tag{4.2}$$

$$\frac{\partial\eta}{\partial t} = -\frac{1}{R\sin\theta}\left[\left(\frac{\partial M}{\partial\varphi}\right) + \frac{\partial(N\sin\theta)}{\partial\theta}\right] \tag{4.3}$$

where M and N are the depth-integrated flow quantities equal to $(H + \eta)\ u$ and $(H + \eta)\ v$, respectively, along the φ (longitude) and θ (co-latitude) directions. The variables u and v are the water velocity, H is the depth of the ocean at rest, R is the Earth's radius,

t is time, η is the difference in sea level at time t from its value at rest, and g is the gravitational acceleration. The second and third terms on the right-hand side are the Coriolis and bottom friction forces, respectively, where f is the Coriolis parameter and n is Manning's roughness coefficient.

Each simulation was conducted for 120 minutes using a time step of 0.25 seconds to satisfy the Courant–Friedrichs–Lewy (CFL) stability condition. Synthetic tsunami waveforms were extracted at multiple wave gauge and tide gauge stations. For inversion analysis, the waveforms were uniformly resampled to 10-second intervals for wave gauge data and 1-minute intervals for tide gauge data. These simulation parameters and processing steps were consistently applied across all source scenarios.

4.3.1 Earthquake scenario

The earthquake source scenario simulated in this study adopts the JSPJ model introduced in Section 4.1, which was selected based on its superior fit to observed tsunami waveforms as demonstrated by Fujii and Satake (2024b). This model considers only the co-seismic seafloor displacement and does not include any contribution from submarine landslides. Initial sea surface displacement was calculated using the inverted slip distribution across seven subfaults located along the offshore segment of the northern Noto Peninsula. These parameters, previously summarized in Table 2, serve as the input for tsunami propagation modeling. Figure 4.3 shows the location of the fault segments in the JSPJ model, along with the slip distribution based on the source parameters listed in Table 2. The resulting tsunami waveforms represent the characteristics of an earthquake-only source without any contribution from submarine landslides. Upon completion of the simulation, the resulting initial sea surface displacement is shown in Figure 4.4. The synthetic tsunami waveforms generated from this scenario are presented in Figure 4.5. This scenario is used as a baseline for evaluating the influence of additional tsunami generation mechanisms. Comparisons with the landslide-only and compound-source scenarios are made to assess how including non-seismic components affects the accuracy of initial sea surface displacement estimation and waveform reproduction.

Table 2. Fault parameters of the JSPJ models, based on Fujii and Satake (2024b)

#	Lat. (deg)	Lon. (deg)	Length (km)	Width (km)	Depth (km)	Strike (deg)	Dip (deg)	Rake (deg)	Slip (m)
NT2	37.9928	137.9269	36.6	16.3	2.5	201	50	78	0.36
NT3	37.6895	137.7640	20	16.6	2.3	242	50	117	0.39
NT4	37.6808	137.3973	19.8	16.5	0.7	61	60	122	3.45
NT5	37.5278	137.2075	21.6	17.1	0.2	52	60	108	3.19
NT6	37.3480	136.6900	50	16.7	0.5	66	60	124	3.17
NT8	37.2569	136.6106	15.1	16.7	0.5	69	60	128	0.99
NT9	37.1002	136.5354	18.4	16.7	0.5	34	60	94	0.00

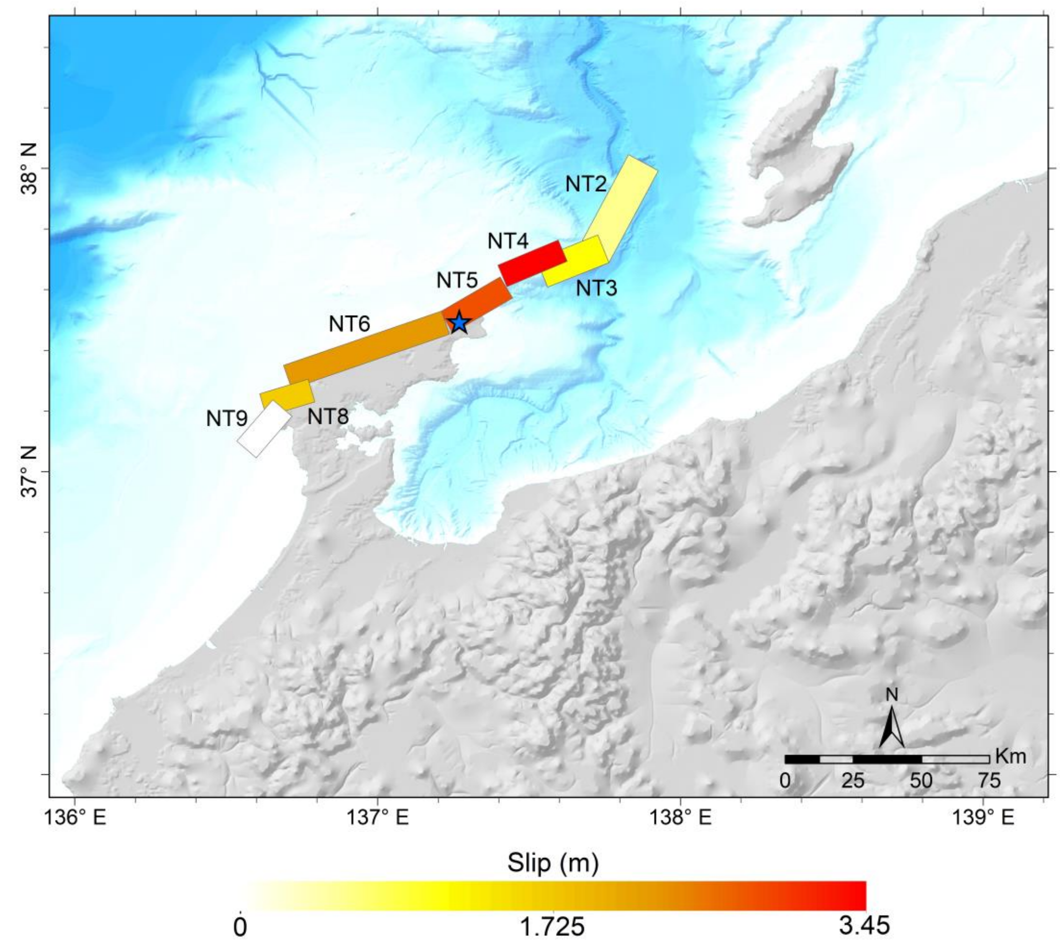

Figure 4.3. Location of the fault segments in the JSPJ model and the corresponding slip distribution based on the source parameters listed in Table 1. The blue star indicates the epicenter of the 2024 Noto earthquake.

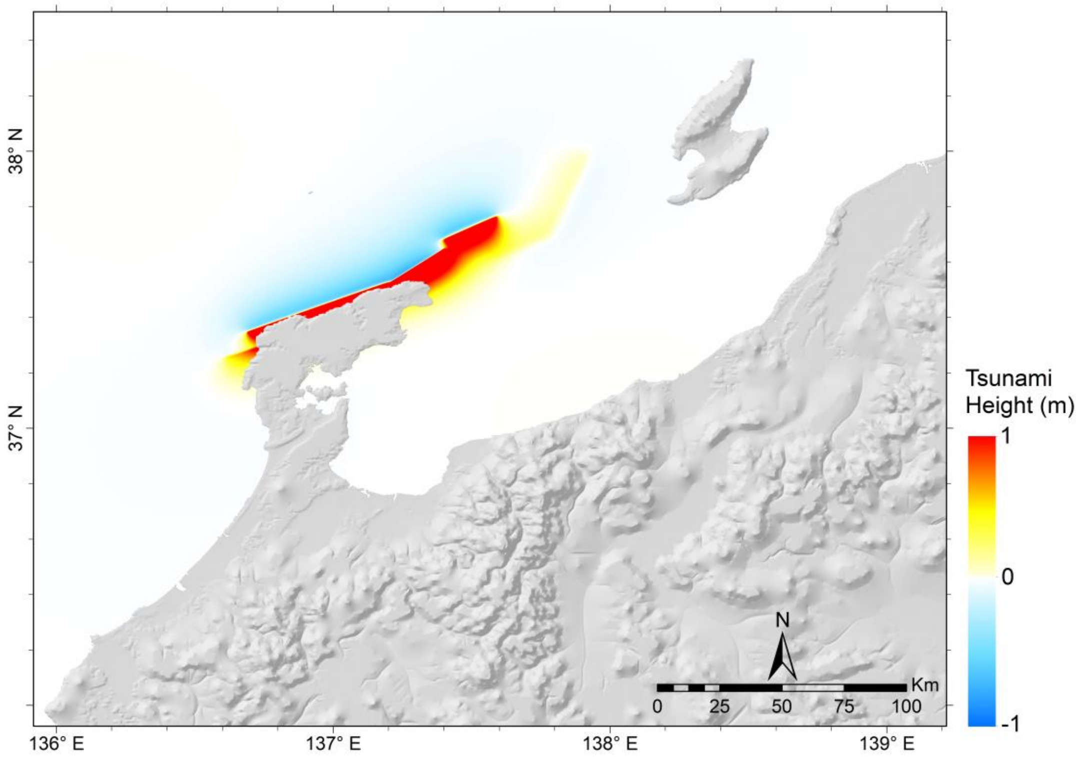

Figure 4.4. Initial sea surface displacement computed from the earthquake scenario proposed by Fujii and Satake (2024b)

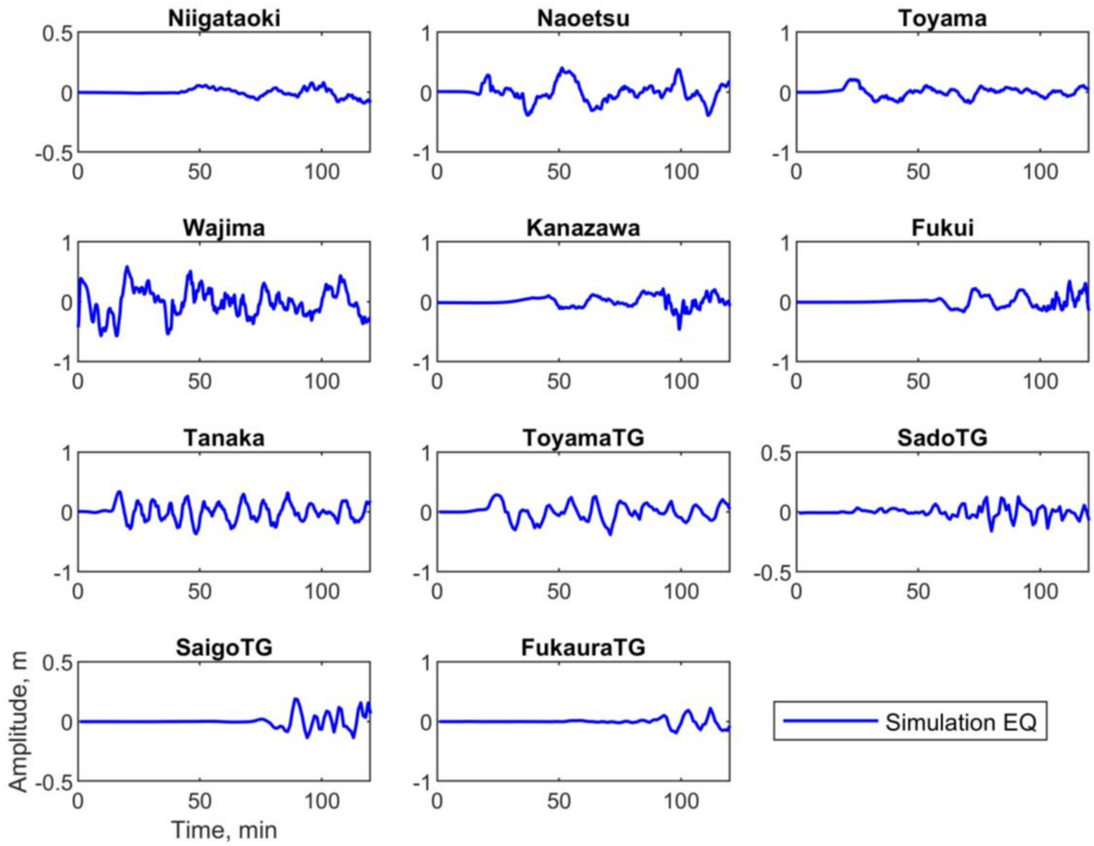

Figure 4.5. Synthetic tsunami waveforms simulated using the earthquake scenario proposed by Fujii and Satake (2024b)

4.3.2 Submarine Landslide Scenario

A tsunami source was introduced in the form of a submarine landslide. The modeling approach adopted in this study follows a static framework based on the empirical formulations originally proposed by Grilli and Watts (2005) and Watts et al. (2005), with further development by Murakami, Shikata, and Tonomo (2018). This framework was designed to simulate tsunami generation mechanisms caused by submarine mass failures (SMF), such as slides and slumps. As illustrated in Figure 4.6, the landslide volume is idealized as a two-dimensional body with a Gaussian-shaped cross-section, either in a rigid form or undergoing deformation during motion. The mass motion is simulated sliding down a gentle slope using a fully non-linear potential flow approach, where the trajectory of the SMF's center of mass is prescribed based on a combination of geometric, hydrodynamic, and material parameters. The simulation results indicate that strong deformation during motion can significantly enhance tsunami amplitude, especially in the far-field. Moreover, slides tend to generate larger waves than slumps, and the initial submergence depth of the SMF strongly influences the resulting tsunami amplitude. Based on the numerical results, Grilli and Watts (2005) and Watts et al. (2005) derived empirical equations to estimate tsunami amplitudes near the source region, incorporating nondimensional parameters such as the initial acceleration of the center of mass and the shear strength along the failure plane. The approach also includes a method to account for three-dimensional effects and establishes a practical relationship between characteristic tsunami amplitude and maximum run-up. This framework is particularly useful for rapid tsunami hazard assessment involving non-seismic sources. The corresponding equations are as follows:

$$\eta(x,y) = -\frac{\eta_{0,3D}}{\eta_{min}} sech^2\left(\kappa\frac{y-y_0}{w+\lambda_0}\right)\left(exp\left\{-\left(\frac{x-x_0}{\lambda_0}\right)^2\right\} - \kappa' exp\left\{-\left(\frac{x-\Delta x-x_0}{\lambda_0}\right)^2\right\}\right) \tag{4.4}$$

$$\eta_{0,3D} = \eta_{0,2D}\left(\frac{w}{w+\lambda_0}\right) \tag{4.5}$$

where, $\eta_{0,3D}$ represents the maximum water level depression in three dimensions, and w denotes the width of the SMF. The parameter η_{min} corresponds to the minimum value of the function on the right-hand side of Equation (4.4), excluding the amplitude component. The shape parameters are expressed as κ and κ', which are assumed to be 8.0 and 1.46, respectively. Additional parameters required for the proposed equation include w, η_0, D, λ_0 (the characteristic tsunami wavelength), and Δx (defined as $\lambda_0/2$). These parameters are either derived from the interpreted morphology of the collapsed seafloor or calculated using a predictive equation for tsunami amplitude, as presented below.

$$t_0 = \sqrt{\frac{R}{g}}\sqrt{\frac{\gamma + C_m}{\gamma - 1}} \tag{4.6}$$

$$\lambda_0 = t_0\sqrt{gd} \tag{4.7}$$

$$\eta_{0,2D} = S_0\left(\frac{0.131}{\sin\theta}\right)\left(\frac{T}{b}\right)\left(\frac{b\sin\theta}{d}\right)^{1.25}\left(\frac{b}{R}\right)^{0.63}(\Delta\Phi)^{0.39}\{1.47 - 0.35(\gamma-1)\}(\gamma-1) \tag{4.8}$$

In this context, the variables are defined as follows: b is the length of the SMF, d represents its initial depth, and T is the thickness of the failing mass. The slope angle is denoted by θ, and γ refers to the specific gravity of the SMF. X_g indicates the coordinate at which the initial water depth is equal to d. C_m, the added mass coefficient, is set to 10.5, S is the total travel distance, and S_0 is the characteristic distance, defined as $S\ /\ 2$. The curvature radius is given by $R = b^2\ /\ 8T$, and the corresponding rotation angle is $\Delta\Phi = 2S_0\ /\ R$. The characteristic time is represented by t_0, while $\eta_{0,2D}$ indicates the maximum water level depression at the location $X = X_g$. Here, X denotes the horizontal coordinate along the slope axis (aligned with the direction of slide motion), while X_g represents the horizontal position of the center of mass of the submarine landslide. Furthermore, the definitions and notations for these parameters, as applied in the SMF model used in this study, are illustrated in Figure 4.6.

In modeling the landslide source, a series of numerical experiments were conducted by varying key parameters of the landslide mass, including its length (b), initial depth (d), thickness (T), and slope angle (θ). The objective of these experiments was to explore how different parameter combinations influence the resulting tsunami waveforms. Although this study did not perform direct waveform fitting against observed data, it was found that certain scenarios could roughly reproduce tsunami characteristics reported at several tide gauge stations affected by the 2024 Noto event, as described by Tajima et al. (2024). Among the tested cases, one scenario was selected for further analysis based on its parameter configuration and resulting wave characteristics. The parameters of this scenario are presented in Table 3, which includes the geometric characteristics of the modeled landslide mass. The initial sea surface displacement generated from this landslide scenario is shown in Figure 4.7. The synthetic tsunami waveforms resulting from this source is presented in Figure 4.8.

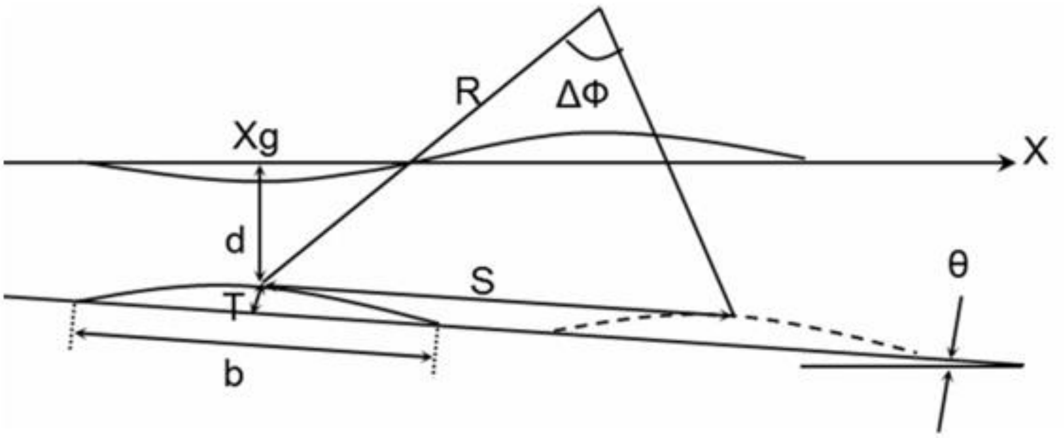

Figure 4.6. Schematic and parameter definitions of the SMF model applied in this study (Murakami, Shikata, & Tonomo, 2018).

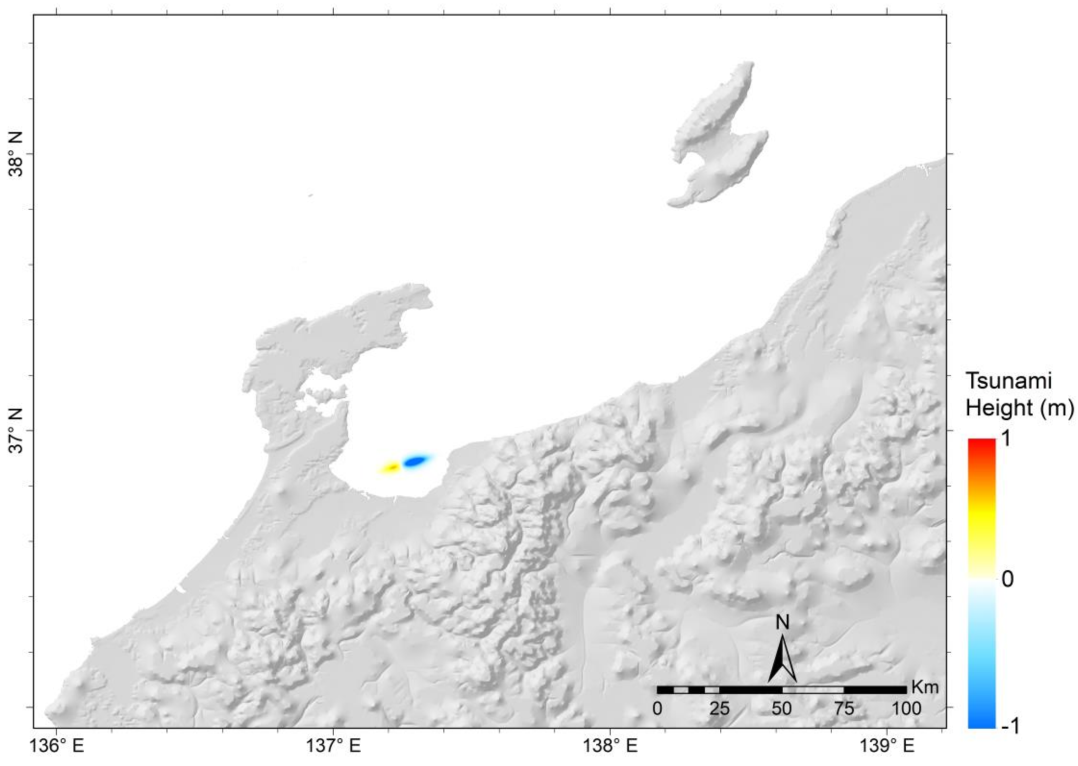

Figure 4.7. Initial sea surface displacement resulting solely from the submarine landslide scenario

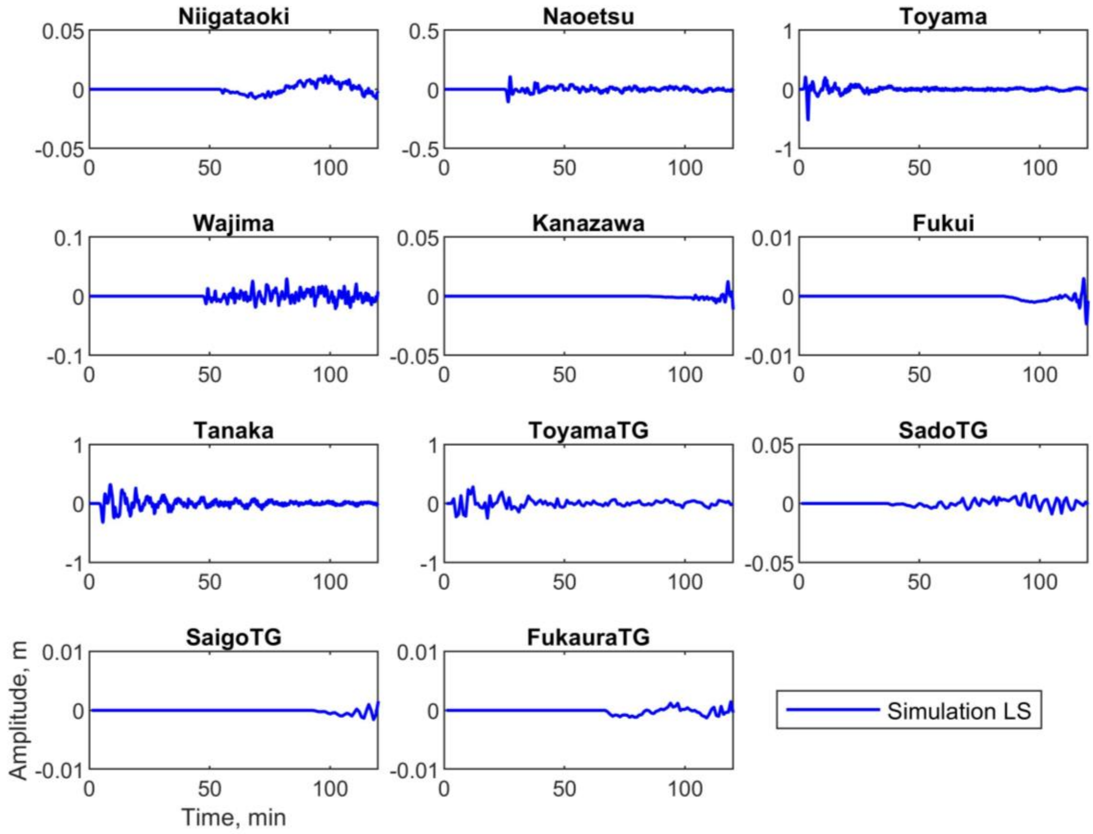

Figure 4.8. Synthetic tsunami waveform generated using only the submarine landslide scenario

Table 3. Model Parameters for the Selected Submarine Landslide Scenario

LS start (Lon/Lat)	LS end (Lon/Lat)	Length (m)	Width (m)	Thickness (m)	Slope angle (°)
137.2512°/36.8757°	137.2371°/36.8726°	3000	1500	70	8

4.3.3 Combine Earthquake and Submarine Landslide Scenario

Following the individual simulations of the earthquake-only and submarine landslide-only scenarios, a third synthetic experiment was conducted to explore the effects of a combined tsunami source. This combined scenario integrates the slip distribution from the earthquake model proposed by Fujii and Satake (2024b) with the submarine landslide parameters identified in the previous subsection, which through trial-and-error were found to approximate the scenario described by Tajima et al. (2024). The purpose of this scenario is to examine how simultaneous contributions from both seismic and non-seismic mechanisms might influence the resulting tsunami waveform characteristics under a controlled modeling framework.

The initial sea surface displacement resulting from the combined source is illustrated in Figure 4.9. Compared to the earthquake-only case, the deformation field appears more irregular and asymmetric. The contribution from the landslide component introduces localized variations near the source region, increasing spatial complexity and potentially influencing the directional distribution of tsunami energy. It should be noted that the landslide-generated tsunami is modeled as a static initial sea surface displacement, which does not represent the dynamic nature of actual submarine landslides. The key objective of this synthetic experiment is to explore how simultaneous contributions from spatially separated seismic and non-seismic sources may affect tsunami propagation and waveform characteristics.

The synthetic tsunami waveforms generated from this combined scenario are presented in Figure 4.10. In general, the waveforms display more complex shapes and a broader range of amplitudes and arrival times compared to those produced by the individual scenarios. These features reflect the superposition of distinct generation mechanisms and offer insights into how compound sources may interact in coastal settings.

This synthetic approach enables an exploratory assessment of compound-source behavior in regions with both tectonic activity and landslide potential. While the source parameters are informed by previously published studies, the analysis remains conceptual and is intended to support the development of tsunami modeling strategies for events with complex origins.

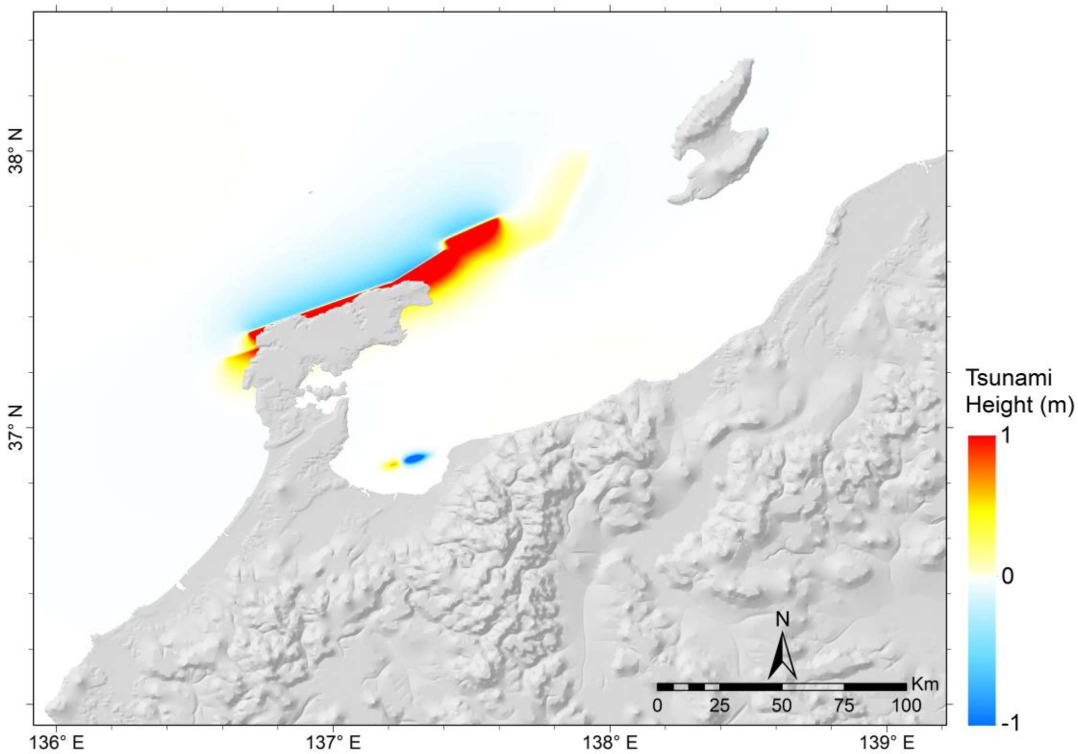

Figure 4.9. Initial sea surface displacement resulting from the combination of the earthquake scenario proposed by Fujii and Satake (2024b) and the selected submarine landslide scenario

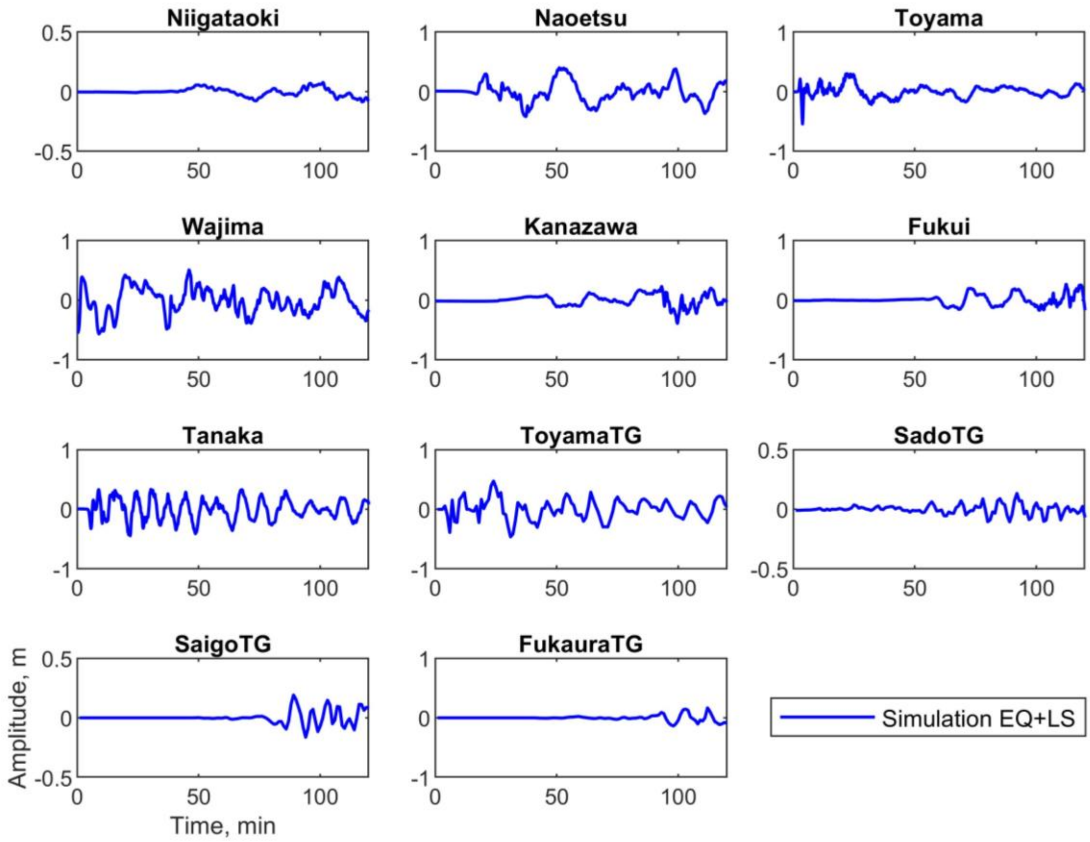

Figure 4.10. Synthetic tsunami waveforms simulated using the earthquake scenario proposed by Fujii and Satake (2024b) combined with the selected submarine landslide scenario

4.4 Estimation of the Potential Tsunami Source Area

Identifying the potential tsunami source area is a crucial step in tsunami modeling, both for forward modeling and inverse modeling approaches. The potential tsunami source area serves as a representation of the initial sea surface deformation that subsequently triggers tsunami wave propagation in various directions. Accurate estimation of this area greatly influences the success of tsunami simulations in reproducing observational data recorded at monitoring stations, as well as in understanding the physical characteristics of the tsunami generation process.

In the context of tsunamis triggered by earthquakes, the most commonly used approach for estimating the potential source area is the application of scaling laws. These laws describe empirical relationships between earthquake magnitude and the extent of seafloor deformation responsible for initiating the tsunami. Generally, there is a correlation between moment magnitude (Mw) and fault geometry parameters such as length, width, and slip amount along the fault plane. Previous studies, including those by Sepúlveda et al. (2017), Kubota et al. (2018), Nakata et al. (2019), and Baba et al. (2020), have demonstrated that scaling-law-based approaches are effective in estimating the initial dimensions of the tsunami source, particularly during the early stages of analysis when observational data are still limited and a rapid estimation is required to initiate further numerical simulations.

In addition to the scaling law approach, the potential source area can also be estimated by utilizing the spatial distribution of aftershocks. This method is based on the assumption that the pattern of aftershock activity around the main earthquake rupture zone can provide clues about the geometry and extent of the fault that contributed to tsunami generation. In many studies, this approach has been employed to estimate the size and orientation of the submarine deformation source by analyzing the spatial pattern of aftershocks that follow the main seismic event. Studies by Satake and Tanioka (1999), Satake et al. (2005), Gusman et al. (2010), and Fujii et al. (2011) indicate that aftershock distribution can serve as an additional indicator in determining whether the deformation source is spread across multiple fault segments or concentrated in a limited area. Although this method is observational in nature and does not directly represent seafloor deformation, the resulting information is still valuable as an initial reference for constructing a more realistic tsunami source model.

For tsunami events not entirely generated by earthquakes, such as those triggered by submarine landslides or other non-seismic mechanisms, the two methods mentioned above become less applicable. This is because landslides do not always produce significant seismic signals, and aftershock distributions are not reliable indicators of deformation geometry in such cases. Therefore, alternative approaches that do not rely on the seismic characteristics of the source are required. One such alternative method is backward tsunami ray tracing, initially introduced by Satake (1988). This method is based on the assumption that tsunami arrival time data recorded at various monitoring stations can be used to trace the direction of wave propagation backward toward its source location. The procedure involves treating each station as a reference point for simulating tsunami wave propagation in reverse, based on the observed arrival time data. By calculating how far the wave could have travelled within the observed time frame, it becomes possible to identify regions in the ocean that could plausibly be the tsunami source. When this analysis is performed across multiple stations, the area that consistently matches the arrival time data from all stations is considered the most likely source location.

The main advantage of this method is that it does not require prior knowledge of the tsunami generation mechanism. In other words, it can be applied to both seismically and non-seismically generated tsunamis, as it relies solely on wave propagation geometry and arrival time observations. The ray paths in this method are computed using Huygens' Principle, which states that every point on a wavefront can be treated as a secondary source emitting waves in all directions. The tsunami travel time is calculated based on the actual bathymetry of the study area, resulting in more accurate outcomes compared to assumptions involving straight-line propagation over uniform depth. The application of backward ray tracing has been demonstrated successfully in several tsunami cases. For instance, Hayashi et al. (2011) employed the method to estimate the source of the 2011 Tohoku tsunami, while Heidarzadeh and Satake (2014) applied it to the 2013 Pakistan tsunami, which likely involved contributions from both earthquake rupture and submarine landslide. In both cases, the back-tracing approach revealed initial deformation patterns that could not be fully explained by conventional seismic source models.

In this study, the tsunami back-propagation modeling method is applied to identify the potential tsunami source area, following Tajima et al. (2024). Conceptually, this method is similar to the backward ray tracing approach in that it uses tsunami arrival time data from several monitoring stations to trace the direction of wave propagation back to the source location. However, it differs fundamentally in numerical implementation. Rather than computing theoretical wave paths based on Huygens' Principle, the method performs explicit forward simulations of tsunami wave propagation from each monitoring station, treating each as a hypothetical source. In each simulation, the initial sea surface displacement is modeled using a two-dimensional Gaussian distribution (Tajima et al.,2024). The general form of the initial surface elevation used in this simulation is expressed as follows:

$$\eta(x,y) = \frac{1}{2\pi\sigma^2}\, exp\left[-\frac{(x-x_0)^2\ +\ (y-y_0)^2}{\sigma^2}\right] \tag{4.9}$$

where η represents the water surface elevation above the mean sea level for the unit source, x and y denote the longitudinal and latitudinal coordinates respectively, x_0 and y_0 are the coordinates of each tsunami monitoring station, and σ is the horizontal scale parameter which is set to 250 m.

After defining the Gaussian-based source distribution for each monitoring station, tsunami propagation simulations are conducted over the entire study domain. These simulations are performed using the JAGURS software, developed by Baba et al. (2015; 2017), which implements the linear long wave (LLW) equation, as expressed by the following formulation:

$$\frac{\partial Hu}{\partial t} = -\frac{gH}{R\sin\theta}\frac{\partial\eta}{\partial\varphi} - fHv \tag{4.10}$$

$$\frac{\partial Hv}{\partial t} = -\frac{gH}{R}\frac{\partial\eta}{\partial\theta} + fHu \tag{4.11}$$

$$\frac{\partial\eta}{\partial t} = -\frac{1}{R\sin\theta}\left[\frac{\partial Hu}{\partial\varphi} + \frac{\partial Hv\sin\theta}{\partial\theta}\right] \tag{4.12}$$

here, u and v represent the horizontal flow velocities in the longitudinal (φ) and co-latitudinal (θ) directions respectively, η denotes the water surface elevation, H is the undisturbed ocean depth, t is time, R stands for the Earth's radius, g is the gravitational acceleration, and f denotes the Coriolis parameter.

Subsequently, the potential source area was determined by categorizing it according to the different source mechanisms underlying each scenario. The estimation was divided into three categories, corresponding to the respective source types: the earthquake-only scenario, the submarine landslide-only scenario, and the combined earthquake and submarine landslide scenario. Tsunami arrival times at each monitoring station were derived from the numerical simulations conducted for each scenario. To constrain the potential source area in the earthquake-only case, synthetic waveform from six wave gauge stations (Niigataoki, Naoetsu, Toyama, Kanazawa, Fukui, and Tanaka) and four tide gauge stations (Toyama, Sado, Saigo, and Fukaura) were used. In this case, tsunami arrival time data from the Wajima wave gauge station were excluded, as it is located within the area of initial sea surface displacement. Consequently, the arrival time at this station is effectively zero, rendering it unsuitable for back-propagation analysis.

For both the submarine landslide only scenario and the combined earthquake and submarine landslide scenario, four additional tsunami monitoring stations were incorporated into the modeling framework: Ishida, Ikuji, Fushiki, and Nanao. The inclusion of these stations may help improve spatial coverage. It should be noted that these stations were used solely to provide constraints on the potential source area and were not included in the inversion process. In the combined earthquake and landslide scenario, the constraints were derived from six wave gauge stations, namely Niigataoki, Naoetsu, Toyama, Kanazawa, Fukui, and Tanaka, and four tide gauge stations, which are Toyama, Sado, Saigo, and Fukaura, along with the four additional monitoring stations mentioned above. In contrast, for the submarine landslide-only scenario, the primary constraints were based on three wave gauge stations, namely Naoetsu, Toyama, and Tanaka, and one tide gauge station, which is Toyama. The four additional stations, specifically Ishida, Ikuji, Fushiki, and Nanao, were also incorporated in this scenario to improve the spatial definition of the potential source area. As a result, the configuration of stations used to constrain the potential source area varied depending on the scenario.

The synthetic waveforms and the potential source areas resulting from each scenario are presented in the following figures. Figures 4.11 and 4.12 correspond to the earthquake-only scenario, showing the simulated waveforms and the potential source area, respectively. Figures 4.13 and 4.14 present the results for the submarine landslide-only scenario, while Figures 4.15 and 4.16 show the results for the combined earthquake and submarine landslide scenario.

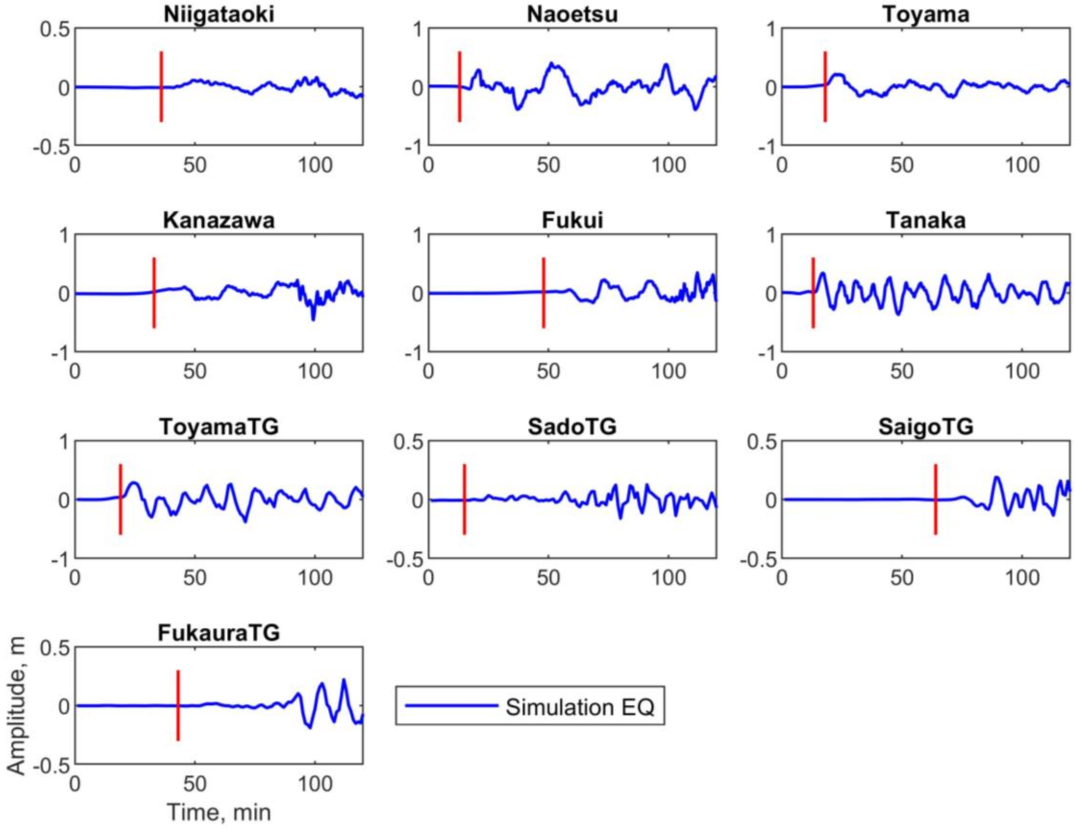

Figure 4.11. Tsunami arrival time picking on the synthetic waveform generated by the earthquake scenario.

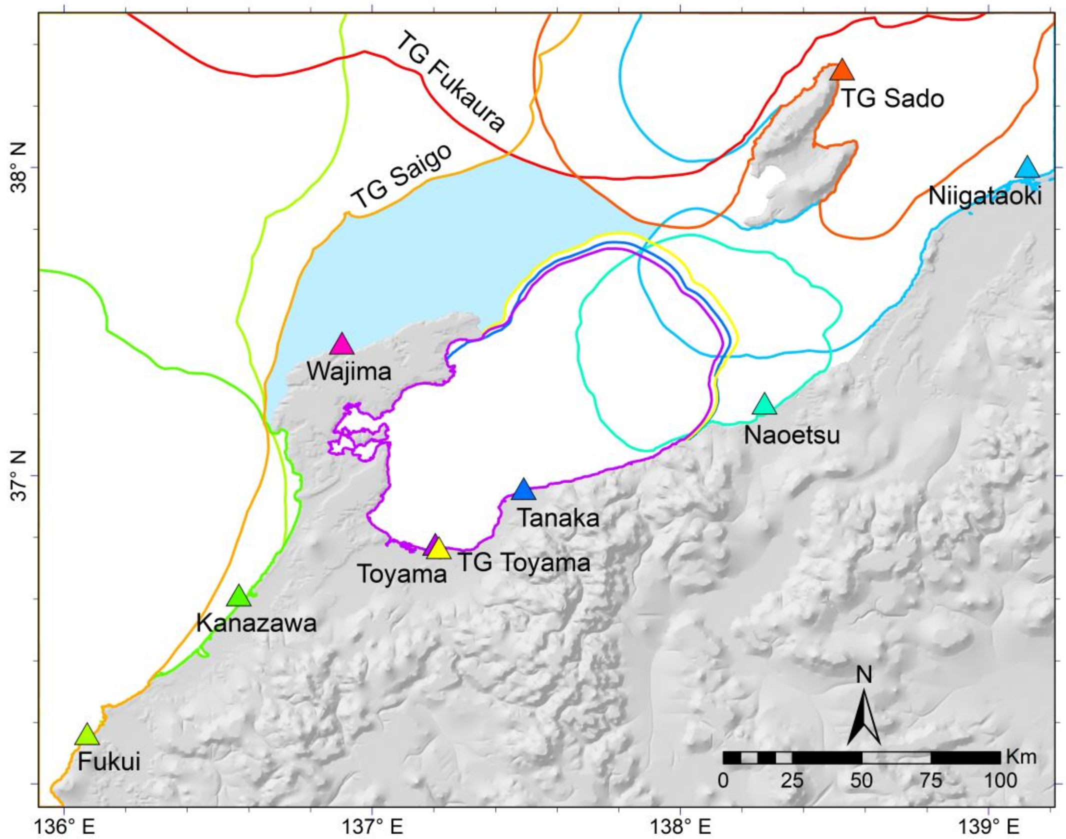

Figure 4.12. Potential source area for the earthquake-only scenario using the back-propagation method. The light blue region indicates the estimated source, while the contour lines represent tsunami travel times traced backward from each station, with line colors matching the color symbols of the corresponding stations

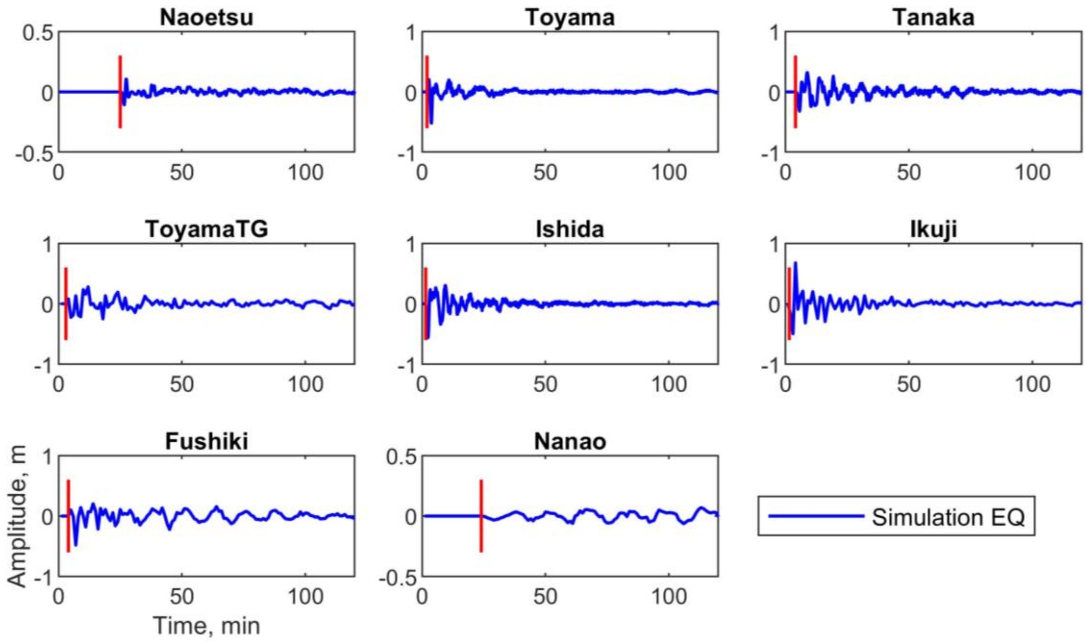

Figure 4.13. Tsunami arrival time picking on the synthetic waveform generated by the submarine landslide scenario.

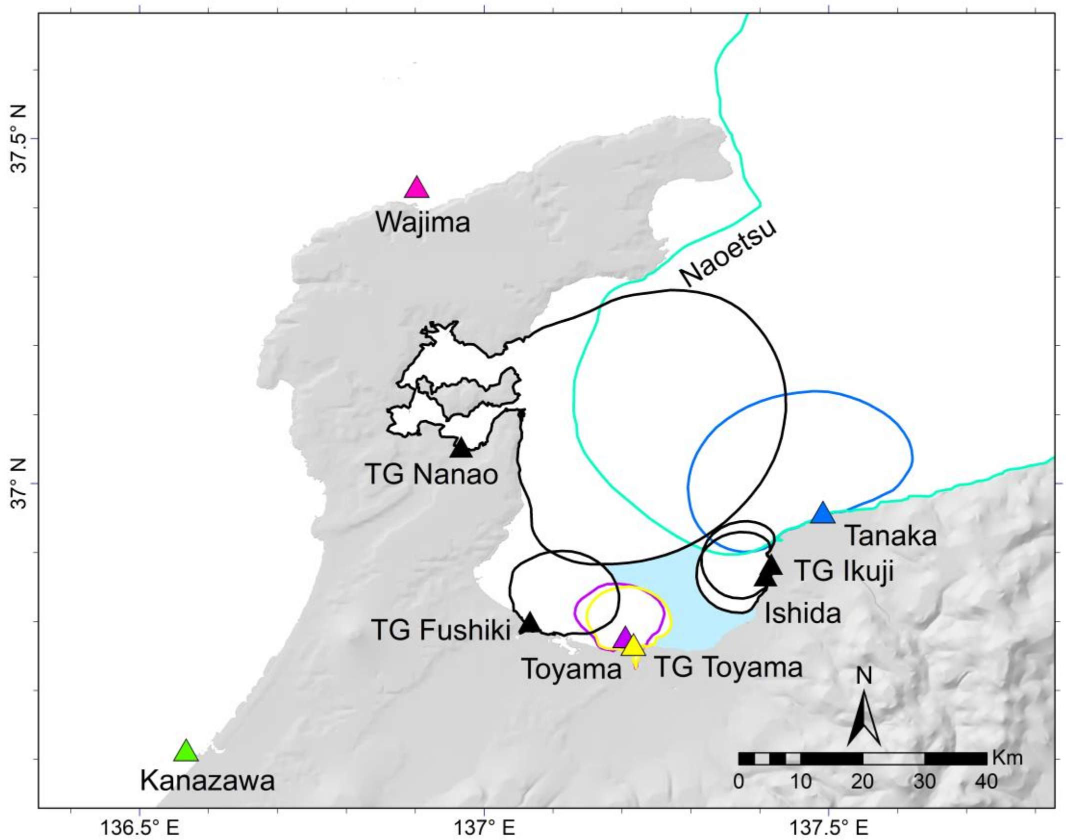

Figure 4.14. Potential source area for the submarine landslide scenario using the back-propagation method. The light blue region indicates the estimated source, while the contour lines represent tsunami travel times traced backward from each station, with line colors matching the color symbols of the corresponding stations.

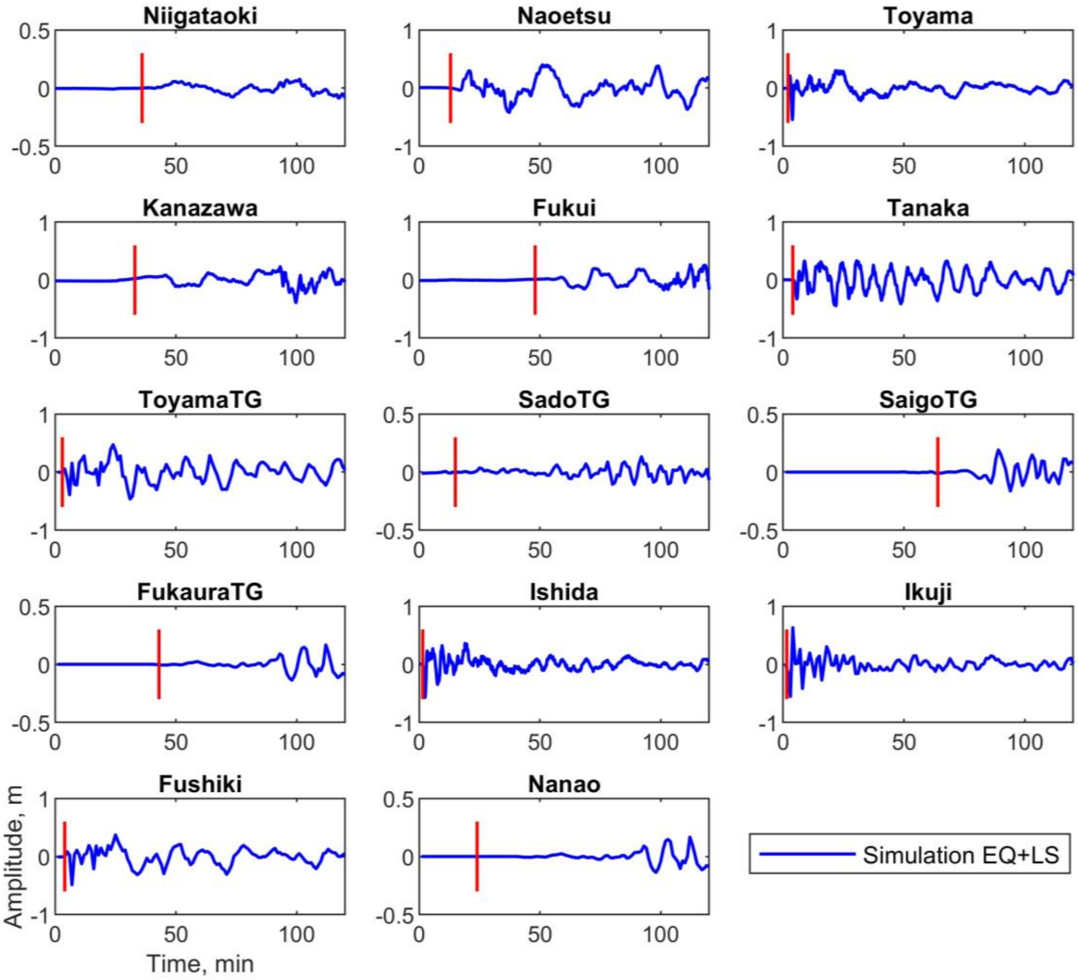

Figure 4.15. Tsunami arrival time picking on synthetic waveforms generated by the combined earthquake and submarine landslide scenarios.

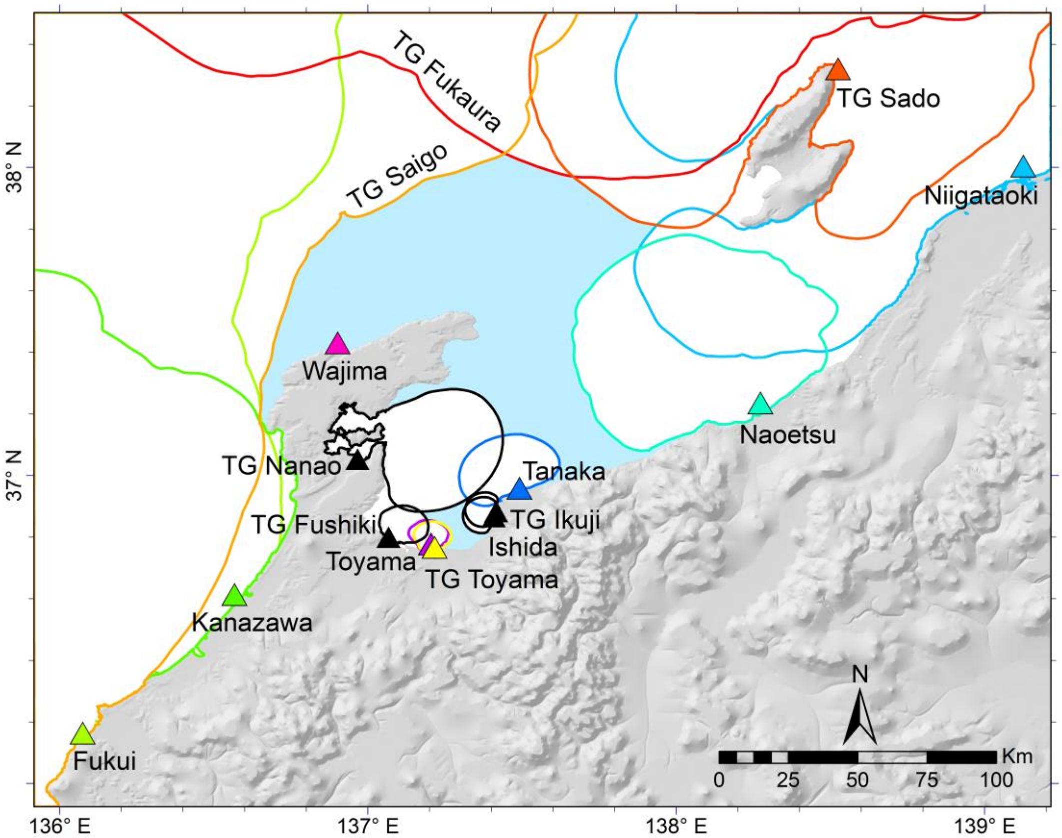

Figure 4.16. Potential source area for the combination of the earthquake and submarine landslide scenarios using the back-propagation method. The light blue region indicates the estimated source, while the contour lines represent tsunami travel times traced backward from each station, with line colors matching the color symbols of the corresponding stations.

4.5 Modeling the Initial Sea Surface Displacement

After delineating the potential source area for each scenario, unit sources were defined to generate the initial sea surface displacement within the corresponding areas. These unit sources form the basis for constructing the initial distribution of sea surface deformation in the subsequent tsunami simulation process. The spacing between unit sources is consistently set at 3 km across the entire potential source area, regardless of the scenario employed. This applies to the earthquake scenario, the combined earthquake and submarine landslide scenario, and the submarine landslide-only scenario. Each unit source adopts a two-dimensional Gaussian distribution, as described by Yamanaka et al. (2019) and Yamanaka and Shimozono (2021). The initial sea surface distribution generated by each unit source is expressed as follows:

$$\eta(x,y) = m_j\, exp\left[-\frac{\left(x-x_j\right)^2 + \left(y-y_j\right)^2}{2\sigma^2}\right] \tag{4.13}$$

here, η represents the water surface elevation above the mean sea level for the unit source. The parameter σ denotes the horizontal variance of the Gaussian distribution and is set at 3 km. The variables x and y indicate the longitudinal and latitudinal positions, respectively. The center coordinates of the j-th unit source are denoted by x_j and y_j, while m_j represents the maximum sea surface elevation at the unit source's center. The index j refers to the sequence of unit sources, with the number of unit sources depending on the scenario being analyzed. A total of 451 unit sources are used for the earthquake scenario, as shown in Figure 4.17. For the submarine landslide-only scenario, 15 unit sources are utilized, as presented in Figure 4.18. The combined earthquake and submarine landslide scenario employs 729 unit sources, as illustrated in Figure 4.19.

As a subsequent step in the modeling process, tsunami simulations were conducted for each Gaussian unit source across all tsunami monitoring stations involved in the study. The objective of these simulations is to obtain Green's functions, which represent the tsunami wave response to a single unit of sea surface deformation. These functions are then used in the linear superposition process. The wave propagation model is based on the two-dimensional linear long wave approximation and is implemented using the JAGURS software developed by Baba et al. (2015, 2017). The fundamental equations used in this model were previously presented in Equation (4.10) – (4.12) in the preceding subsection.

The inversion of observed tsunami waveforms was performed using initial waveform data recorded at the tsunami monitoring stations. In this approach, each observed waveform is represented as a linear superposition of Green's functions at the corresponding station. This method enables the computation of each unit source's contribution to the recorded tsunami signal. To ensure the stability of the inversion solution, two hyperparameters were applied, following the method proposed by Hossen et al. (2015). These include a smoothing parameter α, which reduces unrealistic oscillations in the source distribution, and a damping parameter β, which helps to prevent overfitting to the data. The inversion process is mathematically formulated as follows:

$$\begin{bmatrix} \boldsymbol{G}_{ij} \\ \alpha \boldsymbol{S}_{jj} \\ \beta \boldsymbol{I}_{jj} \end{bmatrix} \boldsymbol{m}_j = \begin{bmatrix} \boldsymbol{d}_i \\ \boldsymbol{0} \\ \boldsymbol{0} \end{bmatrix} \quad (4.14)$$

where $\boldsymbol{G}_{ij}$ denotes the Green's function, $\boldsymbol{S}_{jj}$ is the smoothing matrix constructed following the formulation of Baba et al. (2005), as shown below:

$$0 = m_{p-1,q} + m_{p+1,q} + m_{p,q-1} + m_{p,q+1} - 4m_{p,q} \tag{4.15}$$

where $m_{p,q}$ denotes the initial sea-surface displacement at the source grid point located at position (p, q), with p indexing the longitudinal direction and q the latitudinal direction. $\boldsymbol{I}_{jj}$ is the identity matrix, and m_j is the sea surface elevation parameter at the center of the Gaussian unit source. The term $\boldsymbol{d}_i$ represents the observed tsunami waveform at the i-th station. The parameters α and β are the smoothing and damping hyperparameters, respectively. The index i refers to the observation points, which are the observation stations, with i = 1, 2, ..., N, where N is the total number of observed waveforms. The index j corresponds to the unit sources, with j = 1, 2, ..., M, where M is the total number of unit sources used to discretize the potential source area. To solve the system of equations and estimate the model parameters, a regularized least-squares approach was employed, as it is commonly used for ill-posed linear inversion problems.

To determine the optimal values of the hyperparameters α and β, a grid search cross-validation was conducted over a plausible range of values. Following the approach of Yokoi et al. (2023), a leave-one-station-out cross-validation scheme was implemented. In each iteration, one observation station was selected as the evaluation dataset, while the remaining ten stations were used for the inversion process. Simulated tsunami waveforms from these ten stations were used to perform the inversion for a specific pair of α and β values, thereby yielding a sea surface deformation model. This model was then used to generate synthetic waveforms, which were compared against the simulated waveforms at the evaluation station. The discrepancy between these waveforms was quantified using the root mean square error (RMSE), serving as a metric for assessing the influence of the hyperparameters on model accuracy. The RMSE is defined as follows:

$$RMSE = \sqrt{\frac{1}{N}\sum_{i=1}^{N}\left(u_i^{obs} - u_i^{syn}\right)^2} \tag{4.16}$$

where u_i^{obs} and u_i^{syn} represent the observed and synthetic waveform amplitudes at time index i , respectively, and N is the total number of time steps. This procedure was repeated for each station, resulting in eleven RMSE values for each α, β pair. The average of the eleven RMSE values was used as a performance indicator for each hyperparameter combination. By applying various pairs of α and β , an RMSE function dependent on these two hyperparameters was obtained. The pair yielding the lowest average RMSE was selected as the optimal combination. A final inversion was then performed using all eleven observed tsunami waveforms and the corresponding optimal hyperparameter values. The procedure for performing grid-search cross-validation is shown in Figure 4.20.

Based on the final inversion results, the initial sea surface displacement was evaluated for each tsunami scenario. In the earthquake-only case, the estimated displacement distribution exhibited a broad uplift and subsidence zone consistent with the expected fault geometry. The root mean square error (RMSE) for waveform fitting was 0.0361, calculated using the optimal hyperparameter values of $\alpha = 0.0108$ and $\beta = 0.2417$. The results for this scenario are illustrated in Figures 4.21a, 4.21b, and 4.21c, which respectively show the selected hyperparameter values, the initial sea surface displacement distribution, and the waveform fitting. For the submarine landslide-only scenario, the inversion resulted in a more localized and asymmetric pattern of displacement, consistent with the expected nature of a non-seismic source. The waveform fitting remained reasonable, with an RMSE of 0.0306 obtained using $\alpha = 0.0345$ and $\beta = 0.2974$. The results are displayed in Figures 4.22a, 4.22b, and 4.22c, showing the hyperparameter values, displacement distribution, and waveform fitting, respectively. In the combined earthquake and submarine landslide scenario, the inversion yielded a slightly more complex distribution of sea surface displacement, capturing features that suggest the contribution of multiple source mechanisms. The RMSE for waveform fitting in this scenario was 0.0394, obtained using the optimal hyperparameters $\alpha = 0.0284$ and $\beta = 0.3640$. Figures 4.23a, 4.23b, and 4.23c present the hyperparameter selection, initial sea surface displacement, and waveform fitting results for this scenario, respectively.

Overall, the inversion results successfully reproduced the general features of the initial sea surface displacement patterns across all three scenarios. A key insight from this study is that the resolution and accuracy of the estimated sources are highly dependent on the density and spatial configuration of tsunami observation stations. When the station network is sparse or unevenly distributed, the inferred source area tends to become overly diffuse, limiting the model's ability to accurately reconstruct the tsunami source. This finding underscores the importance of designing an optimized and strategically located observation network to improve the reliability of tsunami source inversion.

In addition to the limitations in the source distribution, discrepancies were also observed in the later phases of the synthetic waveforms when compared with the reference simulation results. In the earthquake-only scenario, waveform mismatches appeared in the later phases at the Sado, Saigo, and Fukaura tide gauge stations. In the combined scenario, notable deviations occurred at the Toyama, Fukui, and Tanaka wave gauge stations, as well as at the Toyama, Sado, Saigo, and Fukaura tide gauge stations. The submarine landslide-only scenario exhibited more pronounced differences in the later waveform components at the Naoetsu, Toyama, Wajima, Kanazawa, Fukui, and Tanaka wave gauge stations, and the Toyama tide gauge station. These discrepancies may be attributed not only to the broad spatial extent of the potential source area but also to limitations in the Green's function approach. Specifically, the Green's functions were computed based on a linear long wave model, which does not account for nonlinear interactions that may influence tsunami behavior, particularly in nearshore regions or in compound source scenarios. As a result, these simplifications may lead to inaccuracies in waveform modeling, especially when the signals involve multiple overlapping phases or complex interactions near the coast. While the reference simulation employed a nonlinear long wave model, the influence of nonlinear effects may be limited in this case due to the relatively low water surface amplitudes observed at many stations. Nevertheless, it is important to note that in the combined earthquake and submarine landslide scenario, the waveform agreement decreased even at stations where the tsunami signals are primarily generated by the earthquake. For example, at the Naoetsu, Wajima, Kanazawa, and Fukui wave gauge stations, the waveform fitting was more accurate in the earthquake-only scenario than in the combined scenario. This result suggests that the addition of a landslide component does not always improve the inversion performance and may in fact reduce the model's ability to reproduce observations at certain locations.

Finally, the approach developed in this study demonstrates significant potential for application in real-time tsunami forecasting, particularly in situations that demand rapid assessment. Future research may focus on improving potential source area estimation methods, integrating additional data sources, and enhancing computational efficiency for operational deployment. Specifically, further efforts are needed to validate the modeling framework using actual observed tsunami waveforms from the 2024 Noto event. Incorporating real observational data will allow for a more comprehensive evaluation of the model's accuracy and enhance its reliability for operational use. Continued development in this direction will contribute substantially to disaster risk reduction in tsunami-prone regions.

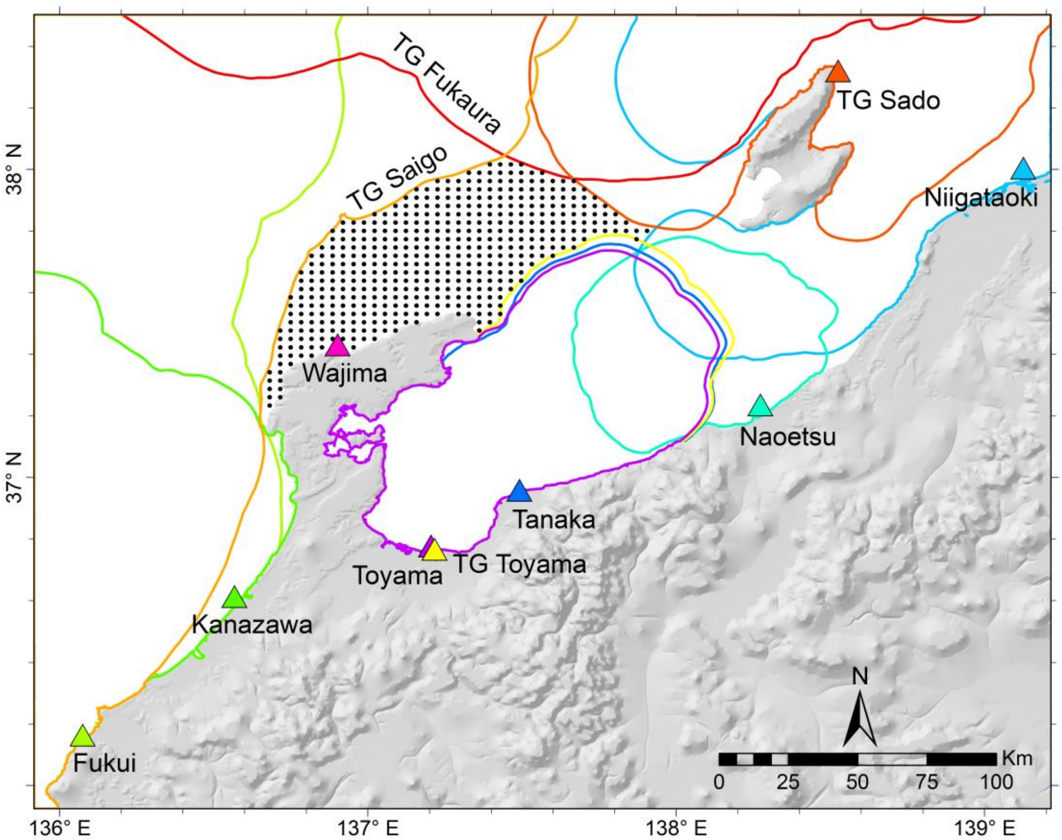

Figure 4.17. Distribution of unit sources (451 units) for the earthquake scenario, represented by black dots.

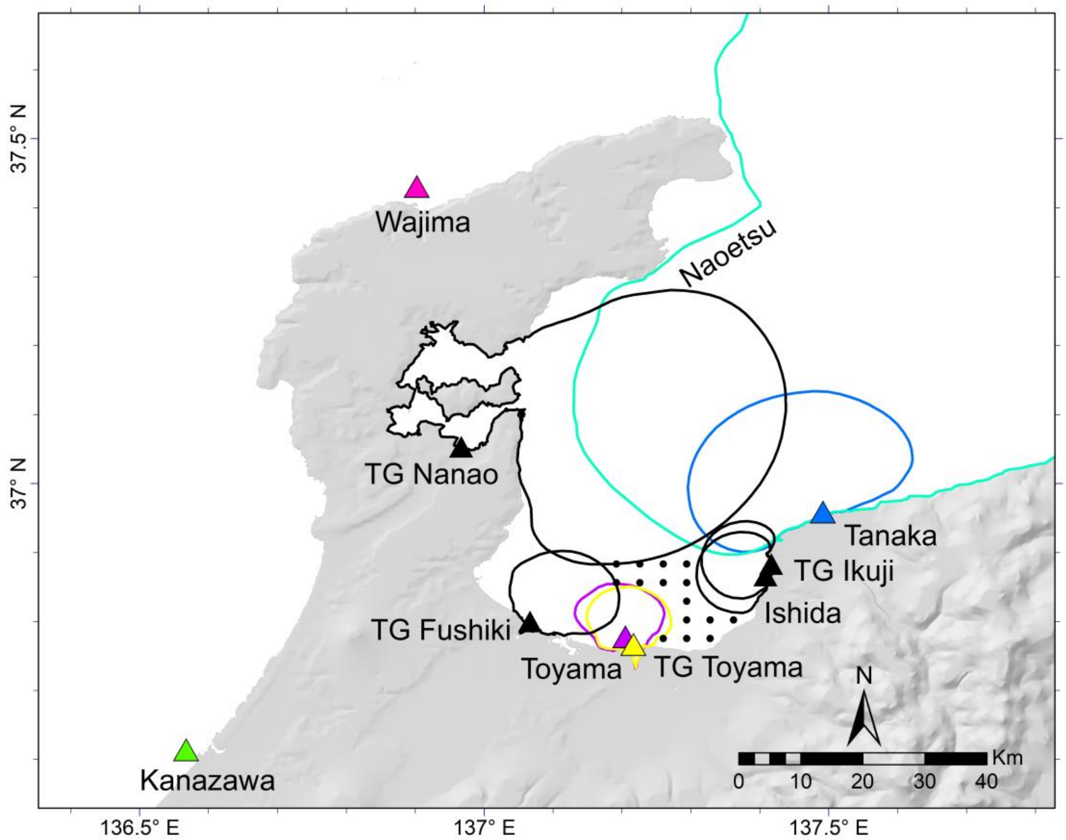

Figure 4.18. Distribution of unit sources (15 units) for the submarine landslide scenario, represented by black dots.

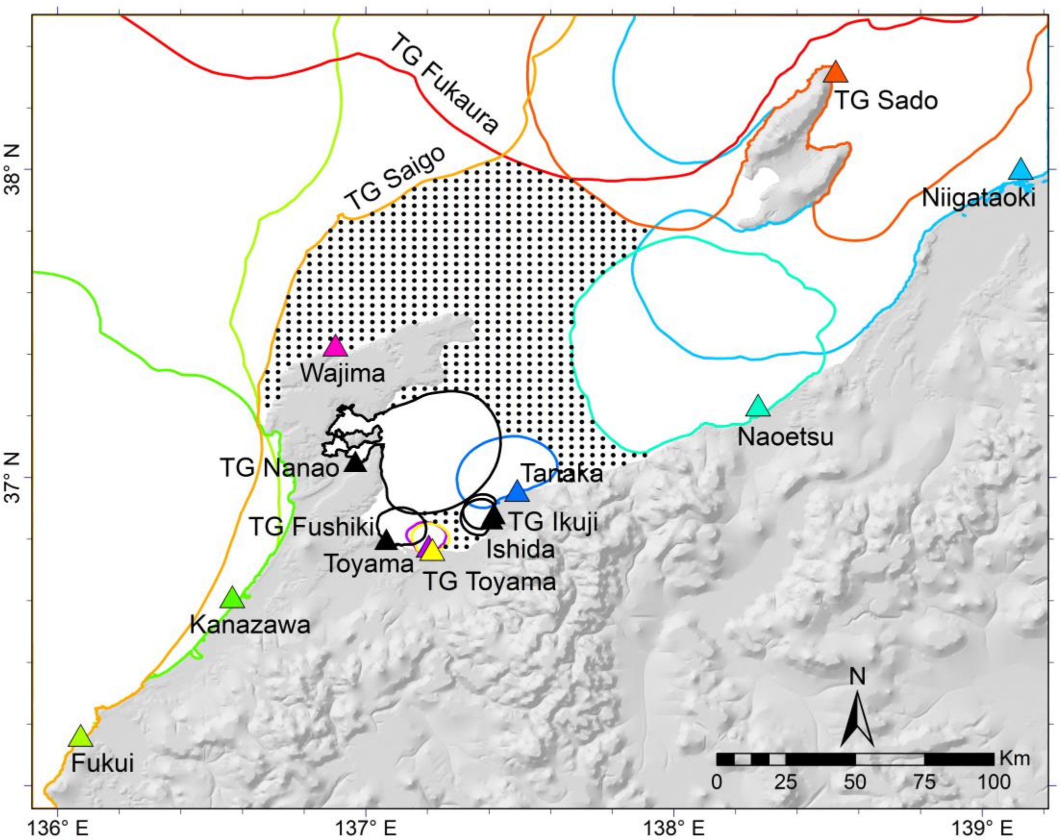

Figure 4.19. Distribution of unit sources (729 units) for the combined earthquake and submarine landslide scenario, represented by black dots.

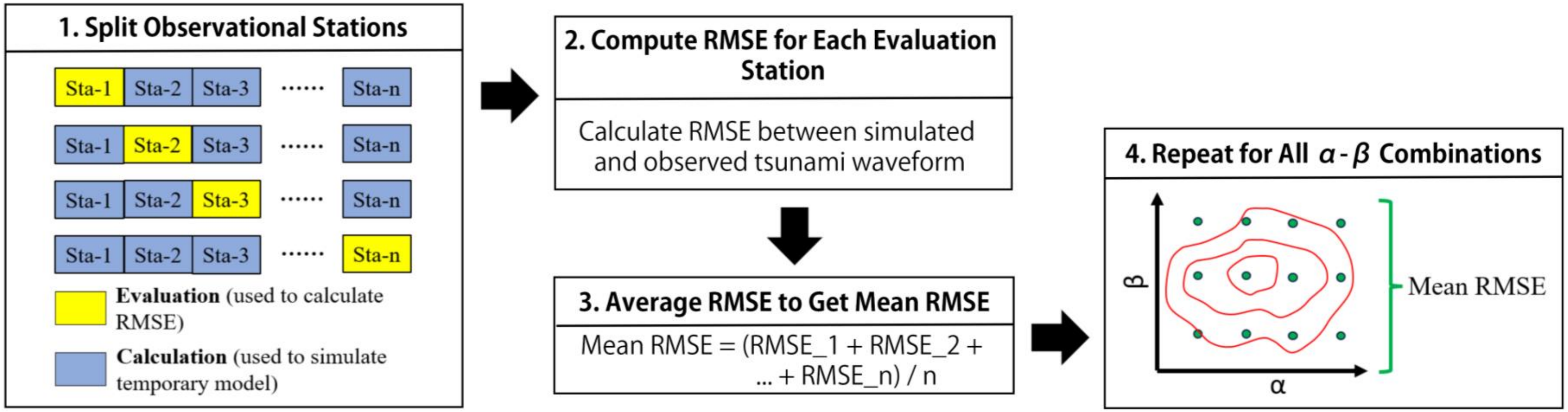

Figure 4.20. Workflow diagram of the grid-search cross-validation method

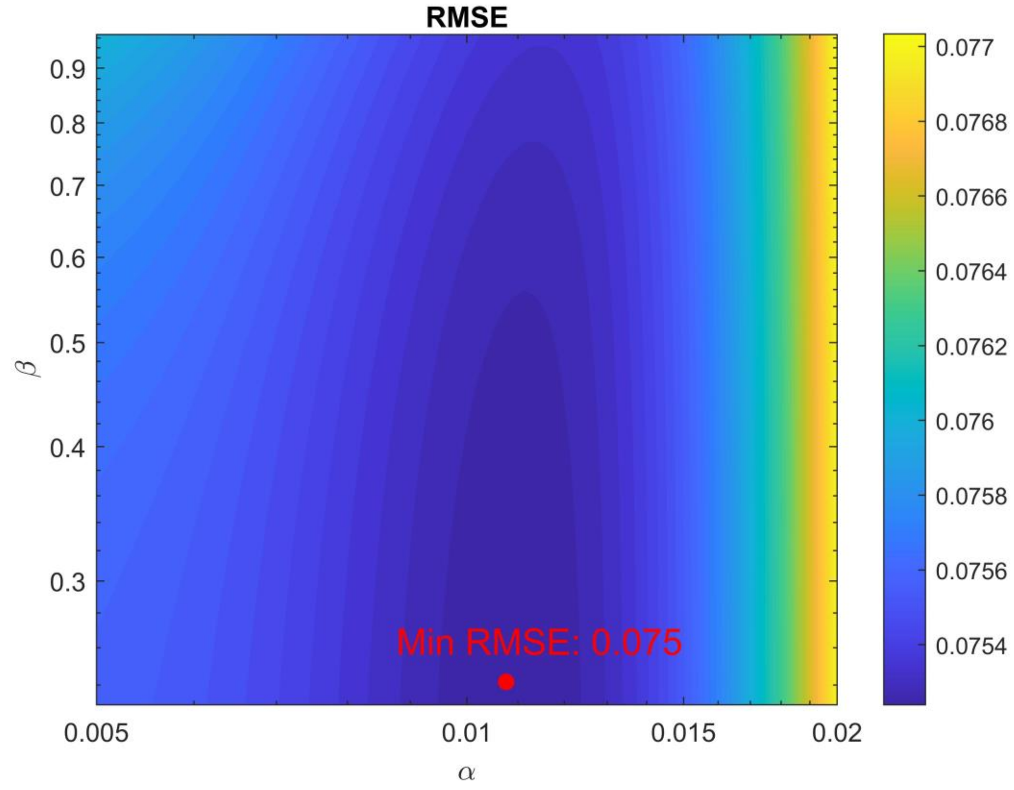

Figure 4.21a. Results of grid search analysis for the earthquake scenario, showing the optimal hyperparameter values of $\alpha = 0.0108$ and $\beta = 0.2417$.

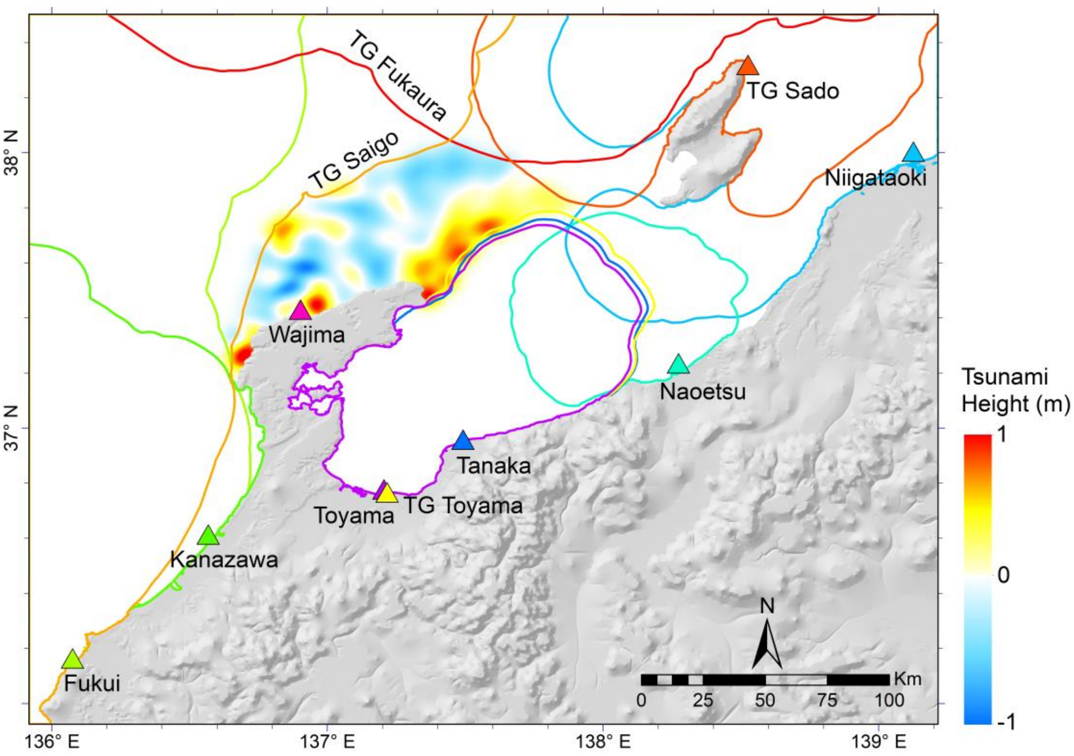

Figure 4.21b. Modeled initial sea surface displacement for the earthquake scenario

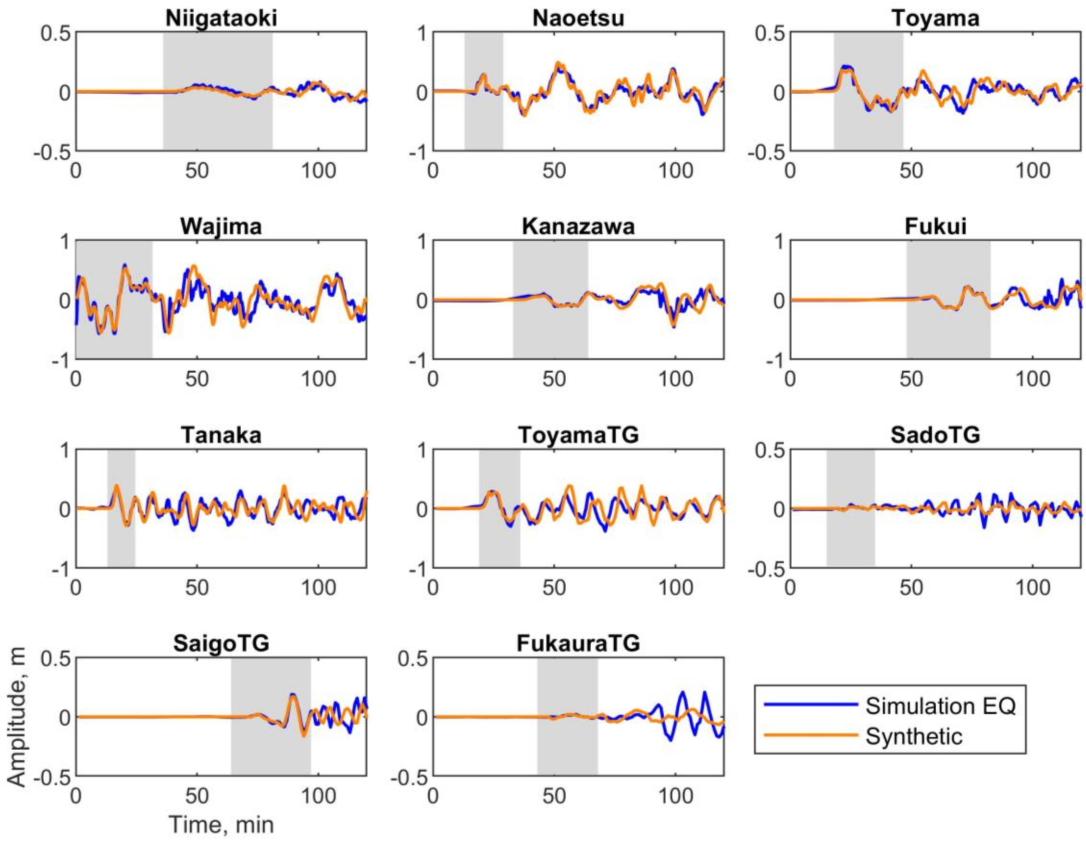

Figure 4.21c. Comparison between observed and simulated waveforms for the earthquake scenario. The gray area indicates the time window used for the inversion.

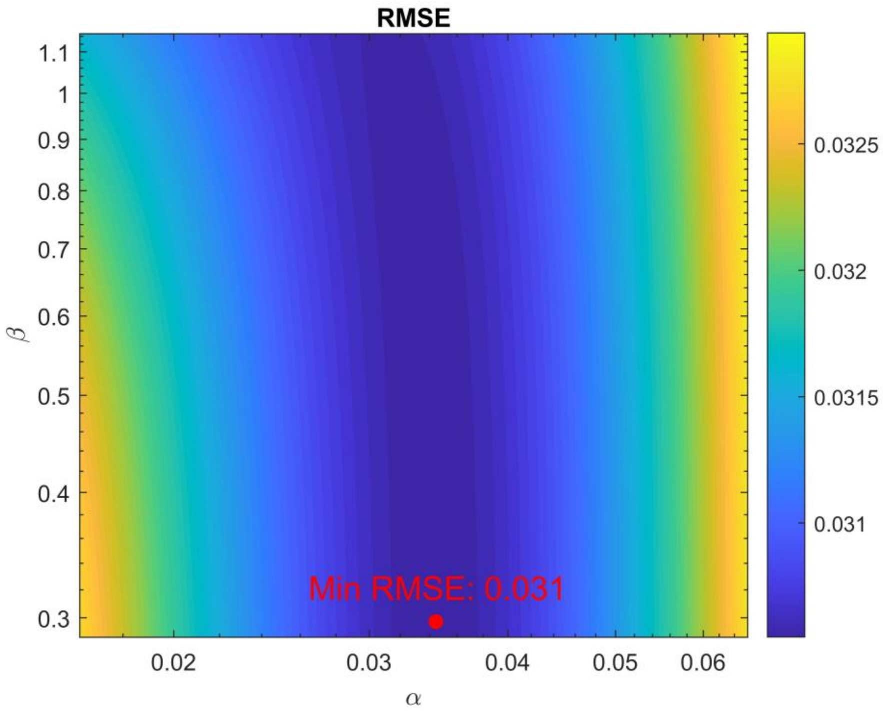

Figure 4.22a. Results of grid search analysis for the submarine landslide-only scenario, showing the optimal hyperparameter values of $\alpha = 0.0345$ and $\beta = 0.2974$.

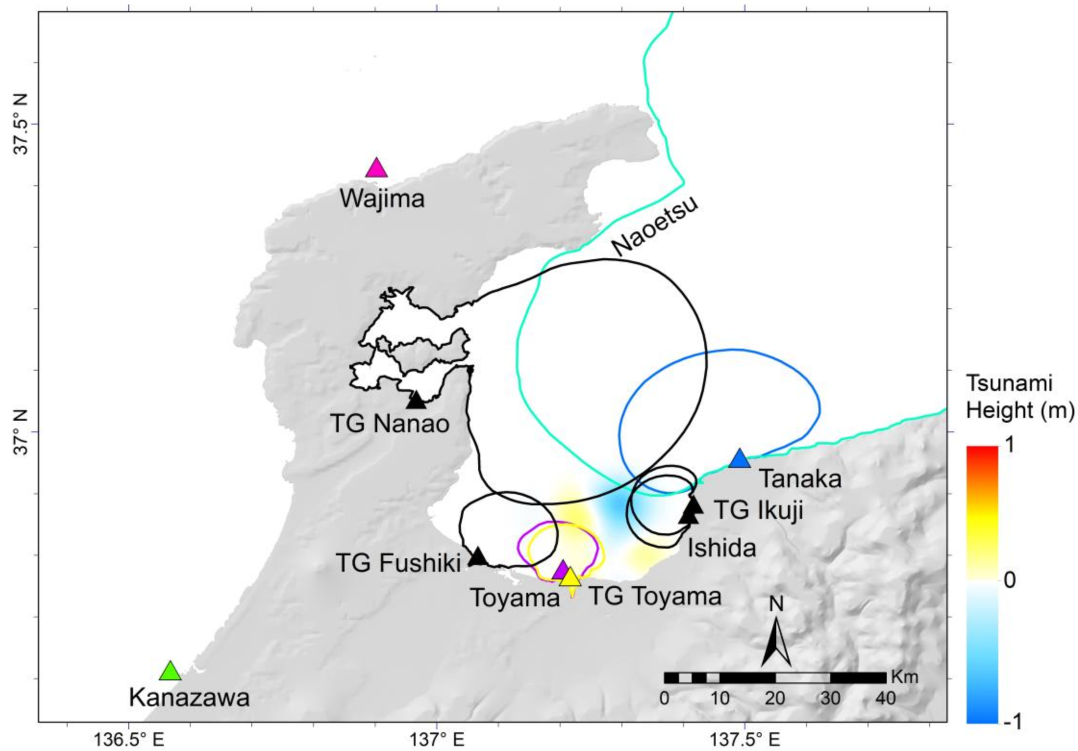

Figure 4.22b. Modeled initial sea surface displacement for the submarine landslide-only scenario.

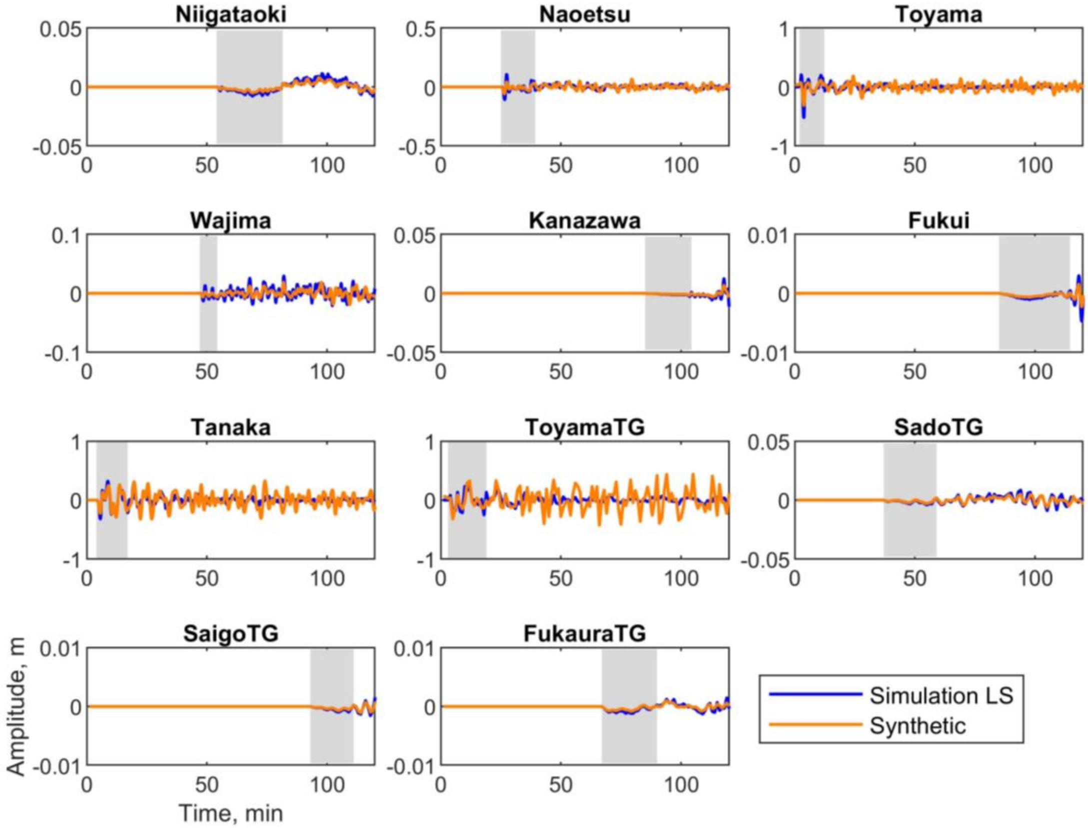

Figure 4.22c. Comparison between observed and simulated waveforms for the submarine landslide-only scenario. The gray area indicates the time window used for the inversion.

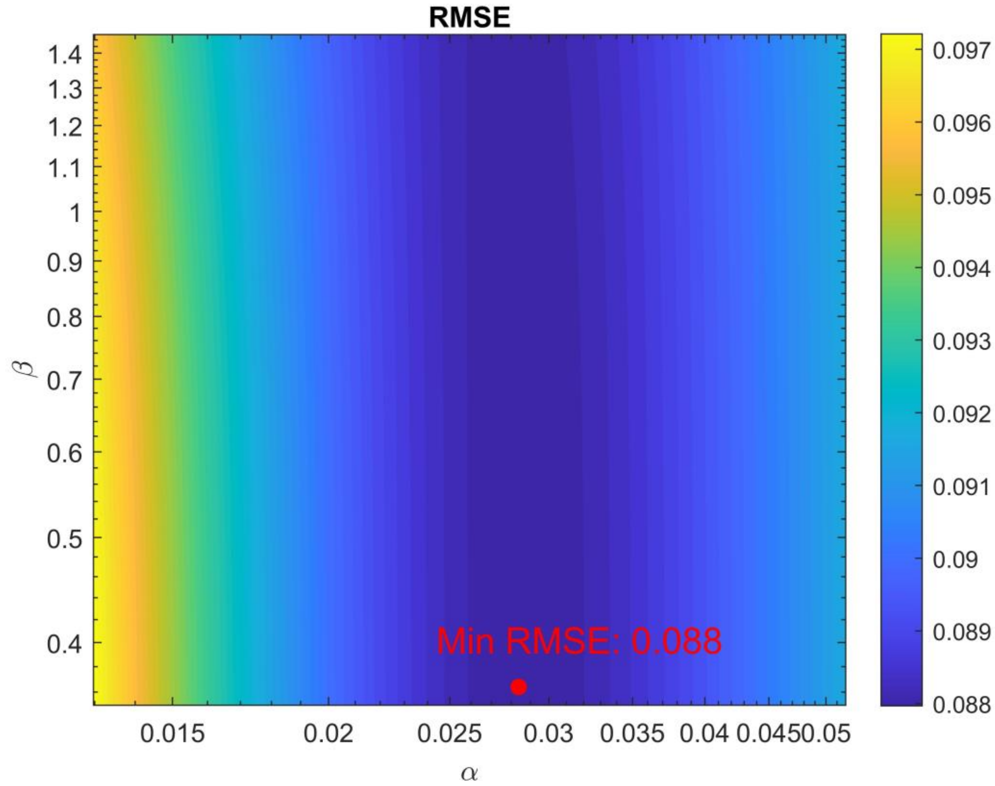

Figure 4.23a. Results of grid search analysis for the combined earthquake and submarine landslide scenario, showing the optimal hyperparameter values of $\alpha = 0.0284$ and $\beta = 0.3640$.

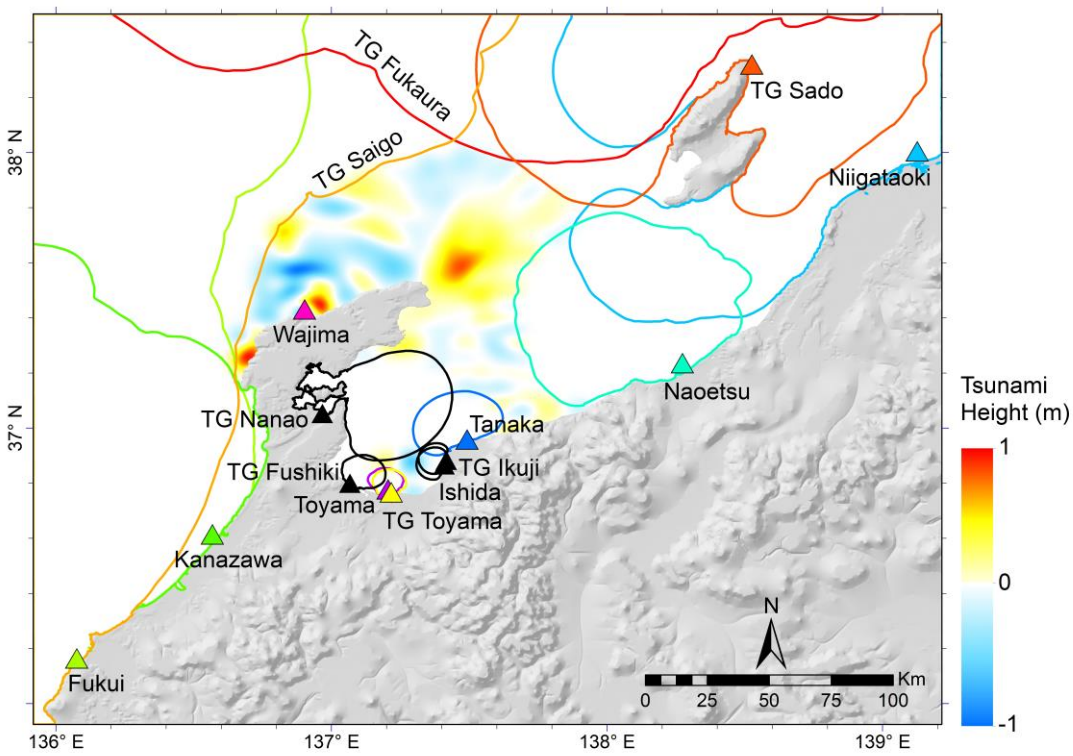

Figure 4.23b. Modeled initial sea surface displacement for the combined earthquake and submarine landslide scenario.

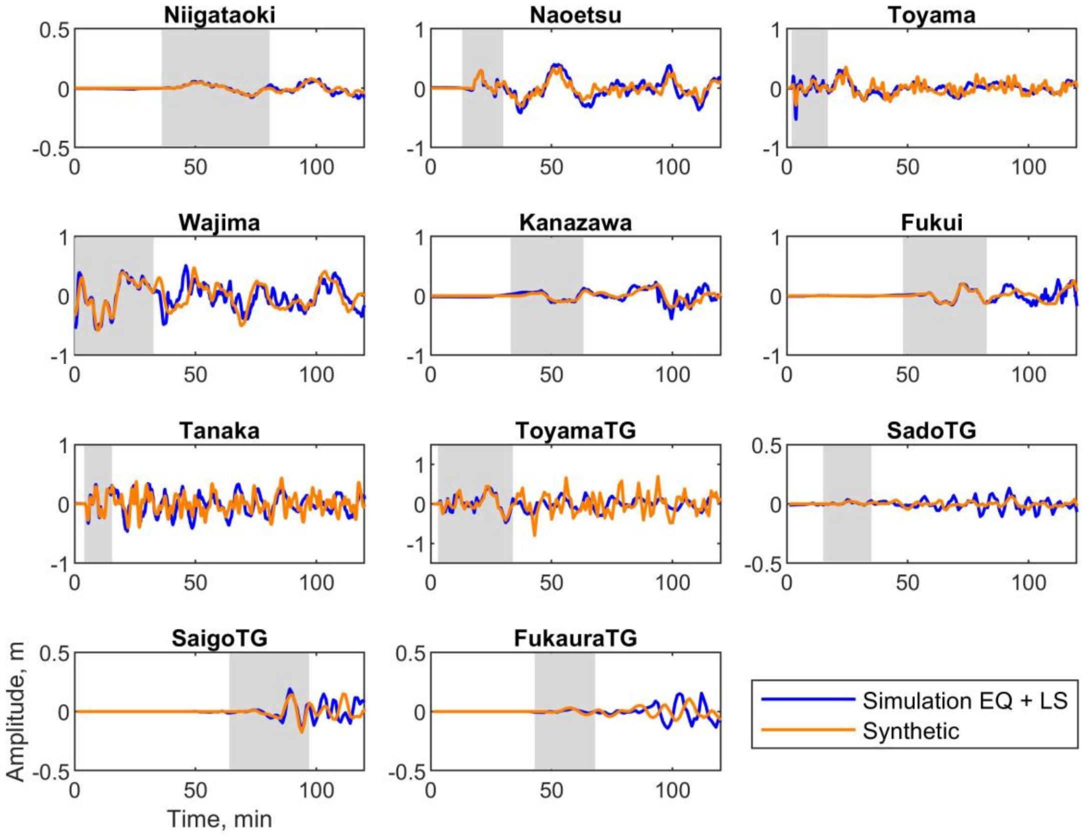

Figure 4.23c. Comparison between observed and simulated waveforms for the combined earthquake and submarine landslide scenario. The gray area indicates the time window used for the inversion.

4.6 Summary of Synthetic Analysis for the 2024 Noto Tsunami

This chapter presented a comprehensive synthetic analysis of the 2024 Noto tsunami by examining various source scenarios and numerical modeling techniques. The study evaluated three distinct tsunami generation mechanisms: the earthquake-only scenario, the submarine landslide-only scenario, and the combined earthquake and landslide scenario. Each scenario was analyzed to assess its contribution to the observed tsunami characteristics and to evaluate the accuracy of inversion techniques under different source assumptions.

To identify the potential tsunami source area, the study employed a back-propagation approach based on tsunami arrival times. This method enabled the estimation of plausible source regions for each scenario. Gaussian unit sources were defined within these areas, and Green's functions were calculated through forward simulations. The inversion process was conducted using a regularized least-squares method, with smoothing and damping hyperparameters determined through grid search and cross-validation.

The earthquake scenario was constructed based on the JSPJ fault model, which provided a reasonable approximation of the tsunami waveforms. However, the simulation results revealed delayed arrival times at several monitoring stations, particularly in Toyama Bay. These discrepancies are consistent with previous studies and indicate that the tsunami generated by the 2024 Noto Earthquake cannot be fully explained by seismic sources alone.

The submarine landslide scenario utilized a static source model based on empirical equations. This scenario successfully reproduced some of the early arrivals and high-frequency components of the tsunami signals observed in Toyama Bay. The resulting waveforms exhibited localized and asymmetric features, consistent with the behavior of non-seismic sources. Nevertheless, this scenario was unable to reproduce the broader waveform characteristics recorded across the full observation network.

The combined scenario, which integrated both the earthquake and submarine landslide components, produced more complex synthetic waveforms, with broader amplitude ranges and irregular arrival patterns. These results reflected the interaction between the two generation mechanisms and highlighted the spatial variability in tsunami propagation. However, the addition of the landslide component did not uniformly improve waveform fitting across all stations. At certain locations, particularly those predominantly influenced by seismic sources, the fitting accuracy decreased compared to the earthquake-only scenario. This finding underscores the inherent challenges in modeling tsunamis generated by compound sources.

The inversion results from all three scenarios generally reproduced the spatial distribution of initial sea surface displacement. The earthquake scenario exhibited a broad deformation pattern, while the landslide and combined scenarios produced more concentrated and irregular features. Although the waveform fitting was generally acceptable, none of the scenarios perfectly matched the reference waveforms, particularly in the later phases. These discrepancies are likely attributed to limitations in station coverage or the use of a Green's function approach based on linear wave assumptions, which may not fully capture the complexities of wave interactions during the later stages of propagation.

Overall, this synthetic analysis suggests that the 2024 Noto tsunami likely involved contributions from both seismic and non-seismic sources. The findings highlight the need for integrated modeling approaches in regions with complex tectonic and bathymetric settings. The modeling framework presented in this chapter provides a foundation for improving tsunami source estimation and supports future efforts to enhance the reliability of real-time tsunami forecasting in compound-source environments.

Chapter 5

Discussion and Conclusions

5.1 Discussion

This study demonstrates that the static source inversion approach offers a practical and computationally efficient solution for tsunami source estimation, particularly in cases involving complex sources such as volcanic activity, submarine landslides, or combinations of seismic and non-seismic mechanisms. While this method has proven effective in reconstructing initial sea surface deformation, its implementation in real-time tsunami early warning systems requires further evaluation, especially concerning computational speed, model flexibility, and limitations in observational data.

One of the key advantages of this approach lies in its simplicity in terms of parameterization and computational demand. Unlike conventional fault-based methods that require detailed assumptions about fault geometry and slip distribution, the static inversion approach relies solely on tsunami waveform data to estimate sea surface deformation. By requiring only a limited set of initial parameters, source estimation can be performed rapidly. The method becomes particularly effective when observational stations are densely distributed around the source region, as the recorded tsunami signals contain strong spatial information that enhances inversion accuracy.

As a point of comparison, the tFISH (tsunami Forecasting based on Inversion for initial sea-Surface Height) method, developed by Tsushima et al. (2009), has been widely adopted in operational tsunami early warning systems. This method utilizes a pre-computed database of Green's functions based on finite-difference solutions to the linear long-wave equations. The tsunami source is discretized into overlapping rectangular elements, and a nested grid system is used to enhance resolution around tide gauge stations. By integrating initial epicentral information from seismic analysis, tFISH estimates sea surface deformation through waveform fitting against the stored Green's functions.

In tFISH, the concept of an influence area is introduced, referring to the region of the sea surface that is considered to contribute to the initial tsunami waveform. This area is defined by back-propagating wavefronts from the observation stations using the estimated origin time of the tsunami. As time progresses, the influence area expands, allowing more distant sources to be considered. However, in cases where only a single station records the initial wave, source location estimation becomes under-constrained and tends to be distributed along the back-propagated wavefront. This condition can reduce the accuracy of predicted tsunami arrival times and amplitudes.

To address the limitations associated with under-constrained tsunami source inversion during the early stages of wave recording, the tFISH method incorporates two additional constraints into its inversion framework: smoothness and spatial damping. The smoothness constraint is applied to suppress unrealistic spatial fluctuations in the estimated initial sea-surface deformation by ensuring that neighboring grid points exhibit smoothly varying displacement values. The smoothness operator **S** is implemented using a discrete Laplacian operator, defined as:

$$0 = a_{l+1,m} + a_{l-1,m} + a_{l,m+1} + a_{l,m-1} - 4a_{l,m} \tag{5.1}$$

where $a_{l,m}$ denotes the initial sea-surface displacement at the grid point located at position (l, m) along the easting and northing axes.

In addition, a spatial damping constraint is introduced to suppress displacement estimates in regions far from the assumed epicenter. This constraint uses a distance-dependent weighting function that decreases linearly with horizontal distance from the source. The damping matrix **D** is a diagonal matrix with components defined by:

$$d_{ij} = \delta_{ij} w(r_i) \tag{5.2}$$

where δ_{ij} is the Kronecker delta and $w(r_i)$ is a weight function that penalizes displacement as a function of the distance r_i between the epicenter and grid point i. The weighting function is expressed as:

$$w(r) = \frac{r}{r_{max}} \tag{5.3}$$

with r being the epicentral distance and r_{max} the maximum horizontal distance between the epicenter and the farthest point within the influence area.

By incorporating these constraints, the inversion system becomes more stable and robust. The regularized inversion equation used in tFISH is formulated as:

$$\begin{bmatrix} \boldsymbol{f}^{obs}(T) \\ \mathbf{0} \\ \mathbf{0} \end{bmatrix} = \begin{bmatrix} \boldsymbol{G}(T) \\ \alpha \boldsymbol{S} \\ \beta \boldsymbol{D} \end{bmatrix} \boldsymbol{a} \quad (0 \le T \le T_0) \tag{5.4}$$

In this formulation, $f^{obs}(T)$ denotes the vector of observed tsunami waveforms, while $\boldsymbol{G}(T)$ is the Green's function matrix that relates unit sea surface displacements to waveforms at observation stations. The vector $\boldsymbol{a}$ represents the initial sea surface displacements to be estimated. The parameters α and β are regularization coefficients that control the strength of the smoothness and damping constrains, respectively. The variable T refers to the elapsed time since the origin time of the earthquake ($T = 0$), and T_0 denotes the time at which the forecast is generated. The waveform data used for forecasting are derived from station records between the tsunami origin time and

T_0, ensuring that the inversion only incorporates the early portion of the tsunami signal relevant for rapid forecasting.

In this study, the influence area for the 2024 Noto tsunami case was defined based on four stations located closest to the tsunami source, namely the Wajima wave gauge, Toyama wave gauge, Toyama tide gauge, and Tanaka wave gauge, as illustrated in Figures 5.1 and 5.2. Figure 5.1 presents the influence area calculated using an elapsed time of 15 minutes, while Figure 5.2 shows the result for 25 minutes. These figures demonstrate that the selected elapsed time significantly affects the extent of the influence area, with longer elapsed times resulting in broader spatial coverage. When using an elapsed time of 15 minutes, the influence area does not fully encompass the deformation zone of the reference model. In contrast, with 25 minutes, the entire deformation region is covered. In such configurations, which apply the damping constraint defined in equations (5.2) and (5.3) to suppress deformation in areas far from the epicenter, the estimated initial sea surface displacement becomes concentrated around the epicentral region. As a consequence, deformation signals originating from submarine landslides located farther away are significantly reduced, resulting in a deformation pattern that no longer matches the reference model. This analysis suggests that while tFISH is effective for purely seismic sources, its performance remains limited in handling compound or non-seismic tsunami sources.

Therefore, as a representative framework for rapid tsunami source estimation, tFISH could be enhanced by integrating the inversion method proposed in this study. A notable strength of the present approach is its ability to separately identify tsunami sources originating from earthquakes and submarine landslides, both in terms of location and deformation pattern. In complex cases such as the 2024 Noto tsunami, where the submarine landslide occurred outside the main tectonic zone, the proposed method yielded more accurate deformation estimates than tFISH.

Nevertheless, a significant challenge identified in this study is the reduction in estimation accuracy when the spatial distribution of observation stations is sparse. This highlights the need to strengthen offshore tsunami observation infrastructure or implement alternative solutions such as virtual stations. The concept of virtual stations has been introduced in prior studies, such as Gusman et al. (2014) and Setiyono et al. (2017), in which virtual sensors are numerically defined and strategically placed within the simulation domain. These stations generate synthetic tsunami data without requiring physical instruments and have been used to assist model calibration through waveform matching.

A similar strategy could be applied in this study, albeit with a different focus. Instead of waveform fitting, virtual stations could be utilized to expand the spatial constraints of tsunami source estimation. By integrating data from virtual stations, source localization can be performed with higher spatial resolution and accuracy, thereby enhancing the effectiveness of the back-propagation method. To implement this strategy effectively, it is necessary to develop a database containing synthetic tsunami waveforms and propagation results at specific time intervals for both real and virtual stations. This development should be accompanied by improvements in the Green’s function formulation, incorporation of nonlinear effects, more accurate modeling of shallow water dynamics, and the use of high-resolution bathymetric data. These enhancements are expected to improve the model’s ability to reproduce tsunami characteristics, particularly during the later phases, and increase the accuracy of initial sea surface deformation estimates, which are critical components for tsunami forecasting and hazard assessment.

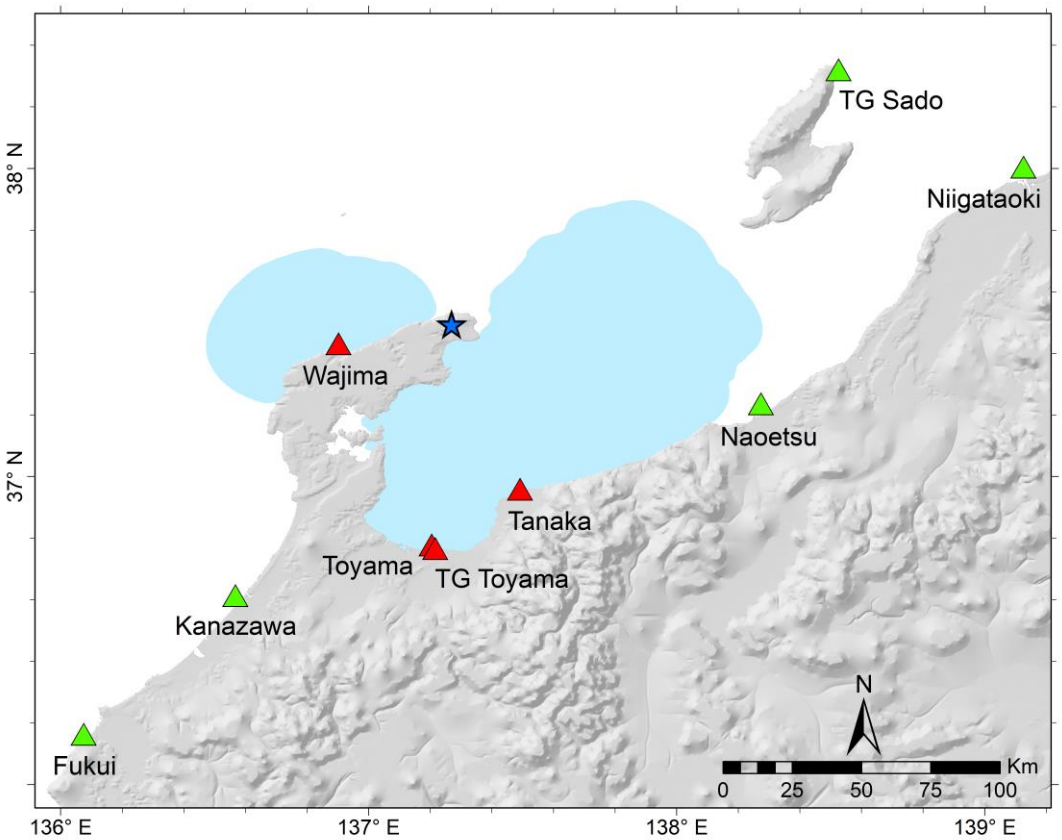

Figure 5.1. Influence area estimated using the method of Tsushima et al. (2009) for the 2024 Noto tsunami, based on an elapsed time of 15 minutes. The influence area is shown in light blue. The blue star indicates the epicenter. Red triangles represent the stations used to define the influence area, while green triangles denote stations located farther from the epicenter.

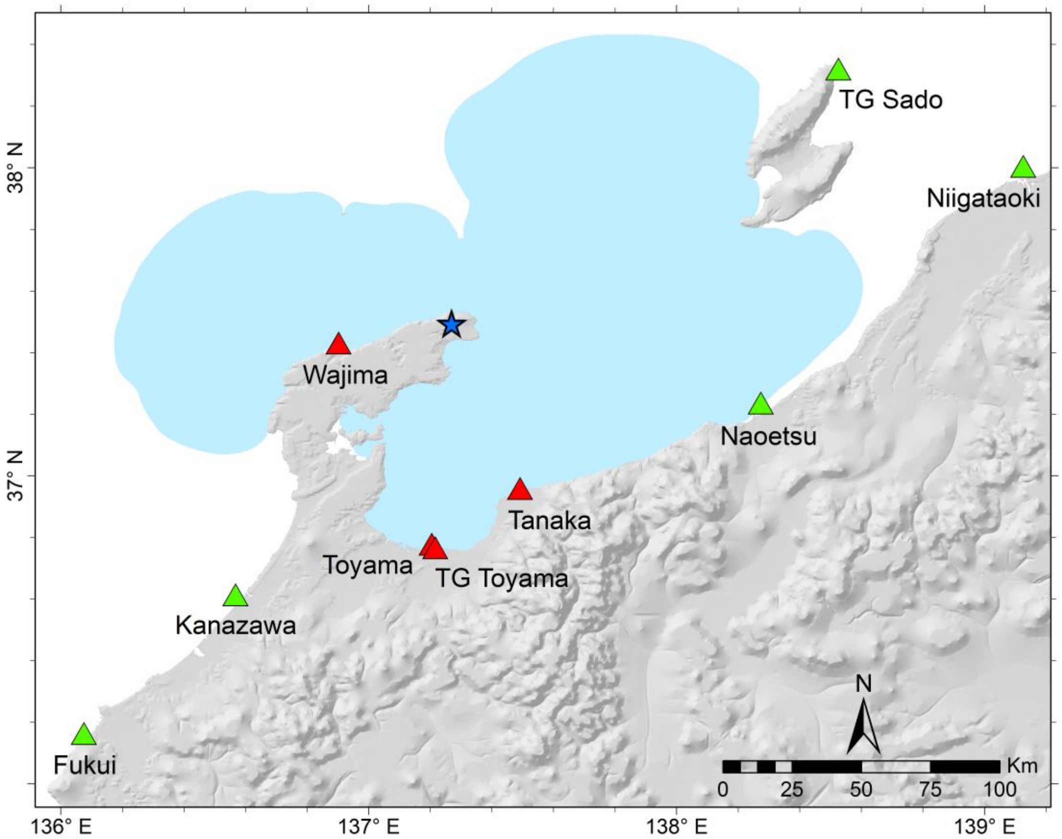

Figure 5.2. Influence area estimated using the method of Tsushima et al. (2009) for the 2024 Noto tsunami, based on an elapsed time of 25 minutes. The influence area is shown in light blue. The blue star indicates the epicenter. Red triangles represent the stations used to define the influence area, while green triangles denote stations located farther from the epicenter.

5.2 Conclusions

This study developed and applied a static source modeling approach based on tsunami waveform inversion to estimate the initial sea surface deformation for two tsunami events with non-seismic and compound generation mechanisms: the 2018 Anak Krakatau volcanic tsunami and the 2024 Noto tsunami. Despite the differing source characteristics of these events, the same modeling framework produced reasonable results and was able to reproduce the spatial and temporal patterns of the observed tsunami waveforms.

In the case of the 2018 Anak Krakatau tsunami, the static source model employing a two-dimensional Gaussian function successfully estimated the tsunami origin time, initial deformation pattern, and displaced water volume, with magnitudes consistent with previously reported landslide estimates. Although based on a linear framework with simplified assumptions, the model captured the dominant features of the tsunami waveforms, even under limited data and noisy conditions. These findings affirm that the static inversion approach is effective for the rapid estimation of tsunami sources generated by volcanic processes.

In the 2024 Noto case, synthetic analysis suggested that the tsunami was likely generated by a combination of seismic faulting and submarine landslides. Three source scenarios were analyzed, including earthquake-only, landslide-only, and a combined case, using a back-propagation technique and Gaussian-based inversion. The combined scenario yielded more realistic and complex waveform features. Although the waveform fitting results within the main time window were generally good and captured the essential characteristics of the observed signals, none of the scenarios achieved accurate fitting during the later phases. These discrepancies highlight the influence of limitations in station coverage and the linear assumptions used in tsunami propagation models. The findings also illustrate the challenges in accurately modeling compound-source events and the importance of integrated modeling strategies.

The discussion in this study highlights several advantages of the static inversion method, including its computational efficiency, flexibility with respect to source types, and minimal reliance on detailed assumptions. Compared to methods such as tFISH, the proposed approach overcomes initial parameter and epicentral distance constraints. Nevertheless, model accuracy is highly dependent on the density and spatial distribution of observation stations. To address this issue, the use of virtual stations is proposed as a strategy to improve spatial coverage in tsunami source estimation. By constructing a comprehensive database of synthetic tsunami waveforms and integrating nonlinear effects and high-resolution bathymetric data, this approach can be further enhanced to better reproduce full tsunami waveform characteristics.

In conclusion, the static inversion framework developed in this study offers a practical, efficient, and adaptable solution for rapid tsunami source estimation across a range of generation mechanisms, including volcanic, submarine landslide, and compound events. The main contribution of this study lies in demonstrating that the approach can be effectively applied to both real and synthetic cases and holds operational relevance for tsunami early warning systems. With the integration of virtual observation strategies and precomputed response databases, this framework offers a promising direction for improving the speed, accuracy, and reliability of tsunami forecasting in the future.

Acknowledgement

With deep respect and gratitude, I would like to express my sincere thanks to my supervisor, Dr. Yusuke Yamanaka, for his invaluable guidance, attention, and academic support throughout my studies and the preparation of this thesis. I also extend my heartfelt thanks to Dr. Yuichiro Tanioka for all the assistance, encouragement, and insightful discussions that have significantly enriched the research process. My sincere appreciation also goes to Dr. Aditya Gusman for the constructive discussions that have greatly contributed to deepening my understanding of the research topic. I am grateful to Prof. Dwikorita Karnawati, Head of the Indonesian Agency for Meteorology, Climatology, and Geophysics (BMKG), for the support and permission granted, which enabled me to pursue this study smoothly. I would also like to express my sincere appreciation to the DX Doctoral Fellowship of Hokkaido University for the financial support provided throughout the course of my studies.

I wish to express my profound gratitude to my beloved parents for their endless prayers, love, and unwavering support. Every step of this journey has been lighter thanks to their blessings and the faith they have instilled in me. To my siblings, Dyah May Karini and Johan Teguh Prasetyo, I am deeply thankful for their help and constant support, which were always present when I needed them the most. I also extend my sincere appreciation to all members of the Institute of Seismology and Volcanology (ISV), Hokkaido University for the collegial atmosphere, insightful discussions, and the various forms of support and encouragement provided throughout my academic

journey. Your presence has fostered a warm, intellectually stimulating, and supportive environment that greatly enriched my experience.

And most importantly, I dedicate my deepest thanks and love to my dearest wife, Khotimah, and my children, Amara Sheza Aaqilah and Sayyid Hisyam Assulaimi. Thank you for being by my side through every step of this journey, and for your sacrifices, patience, and unwavering love. Your presence is my greatest strength and a constant reminder of the purpose behind every struggle. Without your support and companionship, this journey would not have been possible.

References

Abe, K., & Okada, M. (1995). Source Model of Noto-Hanto-Oki Earthquake Tsunami of 7 February 1993. In: Imamura, F., Satake, K. (eds) Tsunamis: 1992–1994. Pageoph Topical Volumes. Birkhäuser Basel. https://doi.org/10.1007/978-3-0348-7279-9_14

Abdurrachman, M., Widiyantoro, S., Priadi, B., & Ismail, T., 2018. Geochemistry and Structure of Krakatoa Volcano in the Sunda Strait, Indonesia. Geosciences, Vol. 8(4), p. 111. https://doi.org/10.3390/geosciences8040111

Baba, T., Cummins, R., & Hori, T., 2005. Compound fault rupture during the 2004 off the Kii Peninsula earthquake (M 7.4) inferred from highly resolved coseismic sea surface deformation. Earth, Planet and Space, Vol. 57, pp. 167–172. https://doi.org/10.1186/BF03351810

Baba, T., Cummins, P.R., Thio, H.K., & Tsushima, H., 2009. Validation and Joint Inversion of Teleseismic Waveforms for Earthquake Source Models Using Deep Ocean Bottom Pressure Records: A Case Study of the 2006 Kuril Megathrust Earthquake. Pure and Applied Geophysics, Vol. 166, pp. 55–76. https://doi.org/10.1007/s00024-008-0438-1

Baba, T., Takahashi, N., Kaneda, Y., Ando, K., Matsuoka, D., & Kato, T., 2015. Parallel Implementation of Dispersive Tsunami Wave Modeling with a Nesting Algorithm for the 2011 Tohoku Tsunami. Pure Appl. Geophys. 172, 3455–3472, https://doi.org/10.1007/s00024-015-1049-2

Baba, T., Allgeyer, S., Hossen, J., Cummins, PR., Tsushima, H., Imai, K., Yamashita, K., & Kato, T., 2017. Accurate numerical simulation of the far-field tsunami caused by the 2011 Tohoku earthquake, including the effects of Boussinesq dispersion, seawater density stratification, elastic loading, and gravitational potential change, Ocean Modeling, Volume 111, Pages 46-54, ISSN 1463-5003. https://doi.org/10.1016/j.ocemod.2017.01.002

Baba, T., Chikasada, N., Nakamura, Y.,Fujie, G., Obana, K., Miura, S., & Kodaira, S., 2020. Deep investigations of outer-rise tsunami characteristics using well-mapped normal faults along the Japan Trench. Journal of Geophysical Research: Solid Earth, 125, e2020JB020060, https://doi.org/10.1029/2020JB020060

BNPB-National Agency for Disaster Management, 2019. Tsunami Selat Sunda (Update 14 Januari 2019). https://bnpb.go.id/berita/tsunami-selat-sunda

Borrero, Jose C., 2005. Field Survey of Northern Sumatra and Banda Aceh, Indonesia after the Tsunami and Earthquake of 26 December 2004. Seismological Research Letters; 76 (3): 312–320. https://doi.org/10.1785/gssrl.76.3.312

Chikasada, N., 2020. Global tsunami Terrain Model. https://doi.org/10.17598/NIED.0021

Escaleras, M.P. & Register, C.A., 2008. Mitigating Natural Disasters through Collective Action: The Effectiveness of Tsunami Early Warnings. Southern Economic Journal, 74: 1017-1034. https://doi.org/10.1002/j.2325-8012.2008.tb00878.x

Fujii, Y., & Satake, K., 2007. Tsunami Source of the 2004 Sumatra–Andaman Earthquake Inferred from Tide Gauge and Satellite Data. Bulletin of the Seismological Society of America; 97 (1A): S192–S207. doi: https://doi.org/10.1785/0120050613

Fujii, Y., Satake, K., Sakai, S., Shinohara, M., & Kanazawa, T., 2011. Tsunami source of the 2011 off the Pacific coast of Tohoku Earthquake. Earth Planet Sp 63, 815–820. https://doi.org/10.5047/eps.2011.06.010

Fujii, Y., & Satake, K., 2013. Slip Distribution and Seismic Moment of the 2010 and 1960 Chilean Earthquakes Inferred from Tsunami Waveforms and Coastal Geodetic Data. Pure Appl. Geophys. 170, 1493–1509. https://doi.org/10.1007/s00024-012-0524-2

Fujii, Y., & Satake, K., 2024a. Modeling the 2022 Tonga Eruption Tsunami Recorded on Ocean Bottom Pressure and Tide Gauges Around the Pacific. Pure Appl. Geophys. 181, 1793–1809. https://doi.org/10.1007/s00024-024-03477-1

Fujii, Y., & Satake, K., 2024b. Slip distribution of the 2024 Noto Peninsula earthquake (MJMA 7.6) estimated from tsunami waveforms and GNSS data. Earth Planets Space 76, 44. https://doi.org/10.1186/s40623-024-01991-z

Grilli, S.T., & P. Watts, 2005. Tsunami Generation by Submarine Mass Failure. I : Modeling, Experimental Validation, and Sensitivity Analysis, Journal of Waterway, Port, Coastal, and Ocean Engineering, ASCE, pp.283-297. https://doi.org/10.1061/(ASCE)0733-950X(2005)131:6(283)

Grilli, S.T., Tappin, D.R., Carey, S., Watt, S.F.L., Ward, S.N., Grilli, A.R., Engwell, S.L., Zhang, C., Kirby, J.T., Schambach, L., & Muin, M., 2019. Modeling of the tsunami from the December 22, 2018 lateral collapse of Anak Krakatau volcano in the Sunda Straits, Indonesia. Scientific Reports, Vol. 9, pp. 11946. https://doi.org/10.1038/s41598-019-48327-6

Grilli S.T., C. Zhang, J.T. Kirby, A.R. Grilli, D.R. Tappin, S.F.L. Watt, J.E. Hunt, A. Novellino, S. Engwell, M.E.M. Nurshal, M. Abdurrachman, M. Cassidy, A.

L. Madden-Nadeau, & S. Day, 2021. Modeling of the Dec. 22nd 2018 Anak Krakatau volcano lateral collapse and tsunami based on recent field surveys: Comparison with observed tsunami impact, Elsevier Marine Geology, Vol. 440, pp. 106566. https://doi.org/10.1016/j.margeo.2021.106566

Gusman, A. R., Tanioka, Y., Kobayashi, T., Latief, H., & Pandoe, W., 2010. Slip distribution of the 2007 Bengkuluearthquake inferred from tsunami waveforms and InSAR data, J. Geophys. Res., 115, B12316. https://doi.org/10.1029/2010JB007565

Gusman, A. R., Tanioka, Y., Sakai, S., & Tsushima, H., 2012. Source model of the great 2011 Tohoku earthquake estimated from tsunami waveforms and crustal deformation data, Earth and Planetary Science Letters, Volumes 341–344, Pages 234-242, ISSN 0012-821X. https://doi.org/10.1016/j.epsl.2012.06.006

Gusman, A. R., Tanioka, Y., MacInnes, B.T., & Tsushima, H., 2014. A methodology for near-field tsunami inundation forecasting: Application to the 2011 Tohoku tsunami, J. Geophys. Res. Solid Earth, 119, 8186–8206. https://doi.org/10.1002/2014JB010958

Gusman, A. R., Satake, K., & Harada, T., 2017. Rupture process of the 2016 Wharton Basin strike-slip faulting earthquake estimated from joint inversion of teleseismic and tsunami waveforms, Geophysical Research Letters, Vol. 44, pp. 4082–4089. https://doi.org/10.1002/2017GL073611

Gusman, A.R., Satake, K., Shinohara, M., Sakai, S., & Tanioka, Y., 2017. Fault Slip Distribution of the 2016 Fukushima Earthquake Estimated from Tsunami Waveforms. Pure Appl. Geophys. 174, 2925–2943. https://doi.org/10.1007/s00024-017-1590-2

Gusman, A. R., Mulia, I. E., & Satake, K., 2018. Optimum sea surface displacement and fault slip distribution of the 2017 Tehuantepec earthquake (Mw8.2) in Mexico estimated from tsunami waveforms. Geophysical Research Letters, Vol. 45, pp. 646–653. https://doi.org/10.1002/2017GL076070

Gusman, A. R., Supendi, P., Nugraha, A. D., Power, W., Latief, H., Sunendar, H., et al., 2019. Source model for the tsunami inside Palu Bay following the 2018 Palu earthquake, Indonesia. Geophysical Research Letters, 46, 8721–8730. https://doi.org/10.1029/2019GL082717

Harbitz, C.B., Løvholt, F., Pedersen, G., & Masson, D.G., 2006. Mechanisms of tsunami generation by submarine landslides: a short review. Norwegian Journal of Geology, Vol. 86, pp. 255-264. Trondheim 2006. ISSN 029-196X.

Hayashi, Y., Tsushima, H., Hirata, K., Kimura, K., & Maeda, K., 2011. Tsunami source area of the 2011 off the Pacific coast of Tohoku Earthquake determined from tsunami arrival times at offshore observation stations. Earth Planet Sp 63, 54. https://doi.org/10.5047/eps.2011.06.042

Heidarzadeh, M., & Satake, K., 2014. Possible sources of the tsunami observed in the northwestern Indian Ocean following the 2013 September 24 Mw 7.7 Pakistan inland earthquake, Geophysical Journal International, Volume 199, Issue 2, Pages 752–766. https://doi.org/10.1093/gji/ggu297

Heidarzadeh, M., Ishibe, T., Sandanbata, O., Muhari, A., & Wijanarto, A.B., 2020. Numerical modeling of the subaerial landslide source of the 22 December 2018 Anak Krakatoa volcanic tsunami, Indonesia. Elsevier Ocean Engineering, Vol. 195, pp. 106733. https://doi.org/10.1016/j.oceaneng.2019.106733

Heidarzadeh, M., Ishibe, T., Gusman, A. R., & Miyazaki, H., 2024. Field surveys of tsunami runup and damage following the January 2024 Mw 7.5 Noto (Japan sea) tsunamigenic earthquake, Ocean Engineering, Volume 307, 118140, ISSN 0029-8018. https://doi.org/10.1016/j.oceaneng.2024.118140

Hossen, M. J., Cummins, P.R., Dettmer, J., & Baba, T., 2015. Tsunami waveform inversion for sea surface displacement following the 2011 Tohoku earthquake: Importance of dispersion and source kinematics, Journal of Geophysical Research: Solid Earth, Vol. 120, pp. 6452–6473, https://doi.org/10.1002/2015JB011942

JAXA-Japan Aerospace Exploration Agency, 2018. Observation Result for Eruption of Anak Krakatau Volcano in Indonesia by Alos-2. https://www.eorc.jaxa.jp/ALOS-2/en/img_up/dis_pal2_eruption_anak_krakatau_20181226.htm (Last Accessed 12 October 2022).

Kubota, T., Saito, T., Ito, Y., Kaneko, Y., Wallace, L. M., Suzuki, S., et al. (2018). Using tsunami waves reflected at the coast to improve offshore earthquake source parameters: Application to the 2016 Mw 7.1 Te Araroa earthquake, New Zealand. Journal of Geophysical Research: Solid Earth, 123, 8767–8779. https://doi.org/10.1029/2018JB015832

Masuda, H., Sugawara, D., Cheng, A. C., Suppasri, A., Shigihara, Y., Kure, S., & Imamura, F., 2024. Modeling the 2024 Noto Peninsula earthquake tsunami: implications for tsunami sources in the eastern margin of the Japan Sea. Geosci. Lett. 11, 29. https://doi.org/10.1186/s40562-024-00344-8

Mori, N., T. Takahashi, T. Yasuda, & H. Yanagisawa, 2011. Survey of 2011 Tohoku earthquake tsunami inundation and run-up, Geophys. Res. Lett., 38, L00G14. https://doi.org/10.1029/2011GL049210

Muhari, A., Heidarzadeh, M., Susmoro, H., Nugroho, H. D., Kriswati, E., Supartoyo., Wijanarto, A. B., Imamura, F., & Arikawa, T., 2019. The December 2018 Anak Krakatau Volcano Tsunami as Inferred from Post-Tsunami Field Surveys and Spectral Analysis. Pure and Applied Geophysics Vol. 176, pp. 5219–5233. https://doi.org/10.1007/s00024-019-02358-2

Mulia, I.E., Watada, S., Ho, T.C., Satake, K., Wang, Y., & Aditiya, A., 2020. Simulation of the 2018 Tsunami Due to the Flank Failure of Anak Krakatau Volcano and Implication for Future Observing Systems. Geophysical Research Letters, Vol. 47, pp. e2020GL087334. https://doi.org/10.1029/2020GL087334

Mulia, I. E., Heidarzadeh, M., Gusman, A. R., Satake, K., Fujii, Y., Sujatmiko, K. A., Meilano, I., & Windupranata, W., 2024. Compounding impacts of the earthquake and submarine landslide on the Toyama Bay tsunami during the January 2024 Noto Peninsula event, Ocean Engineering, Volume 310, Part 1, 118698, ISSN 0029-8018. https://doi.org/10.1016/j.oceaneng.2024.118698

Murakami, Y., Shikata, T., & Tonomo, K., 2019. Case Study of Tsunami Evaluation Triggered by Submarine Landslide. Journal of Natural Disaster Science, 39(1), 1-18. https://doi.org/10.2328/jnds.39.1

Nakata, K., Hayashi, Y., Tsushima, H., Fujita, K., Yoshida, Y., & Katsumata, A., 2019. Performance of uniform and heterogeneous slip distributions for the modeling of the November 2016 off Fukushima earthquake and tsunami, Japan. Earth Planets Space 71, 30. https://doi.org/10.1186/s40623-019-1010-1

Namegaya, Y., & Satake, K., 2008. Tsunami generated by the 2007 Noto Hanto earthquake. Earth Planet Sp 60, 127–132. https://doi.org/10.1186/BF03352773

Nishimura, T., Hiramatsu, Y. & Ohta, Y., 2023. Episodic transient deformation revealed by the analysis of multiple GNSS networks in the Noto Peninsula, central Japan. Sci Rep 13, 8381. https://doi.org/10.1038/s41598-023-35459-z

Okal, EA., & Synolakis, CE., 2004. Source discriminants for near-field tsunamis, Geophysical Journal International, Volume 158, Issue 3, Pages 899–912. https://doi.org/10.1111/j.1365-246X.2004.02347.x

Okamura, Y., Watanabe, M., Morijiri, R., & Satoh, M., 1995. Rifting and basin inversion in the eastern margin of the Japan Sea. Island Arc, 4: 166-181. https://doi.org/10.1111/j.1440-1738.1995.tb00141.x

Omira, R., Dogan, G.G., Hidayat, R. et al., 2019. The September 28th, 2018, Tsunami In Palu-Sulawesi, Indonesia: A Post-Event Field Survey. Pure Appl. Geophys. 176, 1379–1395. https://doi.org/10.1007/s00024-019-02145-z

Omira, R. & Ramalho, I., 2020. Evidence-Calibrated Numerical Model of December 22, 2018, Anak Krakatau Flank Collapse and Tsunami. Pure and Applied Geophysics, Vol. 177, pp. 3059–3071. https://doi.org/10.1007/s00024-020-02532-x

Paris, R., Switzer, AD., Belousova, M., Belousov, A., Ontowirjo, B., Whelley, PL., & Ulvrova, M., 2013. Volcanic tsunami: a review of source mechanisms, past events and hazards in Southeast Asia (Indonesia, Philippines, Papua New

Guinea). Natural Hazards, Vol. 70, pp. 447–470. https://doi.org/10.1007/s11069-013-0822-8

Paris, R., 2015. Source mechanisms of volcanic tsunamis. Phil. Trans. R. Soc. A373:20140380. http://dx.doi.org/10.1098/rsta.2014.0380

Paris, A., Heinrich, P., Paris, R., & Abadie, S., 2020. The December 22, 2018 Anak Krakatau, Indonesia, Landslide and Tsunami: Preliminary Modeling Results. Pure and Applied Geophysics, 177, pp. 571–590. https://doi.org/10.1007/s00024-019-02394-y

Peng, Z., Lei, X., Wang, Q. Y., Wang, D., Mach, P., Yao, D., Kato, A., Obara, K., & Campillo, M., 2025. The evolution process between the earthquake swarm beneath the Noto Peninsula, central Japan and the 2024 M 7.6 Noto Hanto earthquake sequence, Earthquake Research Advances, Volume 5, Issue 1, 100332, ISSN 2772-4670. https://doi.org/10.1016/j.eqrea.2024.100332

Permana, T., Yatimantoro, T., & Handayani, A.S., 2023. Seismic signature detection during the 2018 Anak Krakatau flank collapse and tsunami using seismic amplitudes from regional-scale monitoring, Earth, Planets and Space, Vol. 75, p. 162. https://doi.org/10.1186/s40623-023-01917-1

Ratnasari, R.N., Tanioka, Y., Yamanaka, Y., & Mulia, I.E., 2023. Development of early warning system for tsunamis accompanied by collapse of Anak Krakatau volcano, Indonesia. Frontiers in Earth Science, Vol. 11, pp. 1213493. https://doi.org/10.3389/feart.2023.1213493

Saito, T., Satake, K., & Furumura, T., 2010. Tsunami waveform inversion including dispersive waves: the 2004 earthquake off Kii Peninsula, Japan. Journal of

Geophysical Research, Vol. 115, pp. B06303. https://doi.org/10.1029/2009JB006884

Saito, T., Ito, Y., Inazu, D., & Hino, R., 2011. Tsunami source of the 2011 Tohoku-Oki earthquake, Japan: Inversion analysis based on dispersive tsunami simulations. Geophysical Research Letters, Vol. 38, pp. L00G19. https://doi.org/10.1029/2011GL049089

Sandanbata, O., Watada, S., Satake, K., Kanamori, H., Rivera, L., & Zhan, Z., 2022. Sub-decadal volcanic tsunamis due to submarine trapdoor faulting at Sumisu caldera in the Izu–Bonin Arc. Journal of Geophysical Research: Solid Earth, 127, e2022JB024213. https://doi.org/10.1029/2022JB024213

Satake, K., 1987. Inversion of Tsunami Waveforms for the estimation of a Fault Heterogeneity: Method and Numerical Experiments. Journal of Physics of the Earth, Vol. 35(3), pp. 241–254. https://doi.org/10.4294/jpe1952.35.241

Satake, K., 1988. Effects of bathymetry on tsunami propagation: Application of ray tracing to tsunamis. PAGEOPH 126, 27–36. https://doi.org/10.1007/BF00876912

Satake, K., 1993. Depth distribution of coseismic slip along the Nankai Trough, Japan, from joint inversion of geodetic and tsunami data, Journal of Geophysical Research, Vol. 98(B3), pp. 4553–4565, https://doi.org/10.1029/92JB01553

Satake, K., & Tanioka, Y., 1999. Sources of Tsunami and Tsunamigenic Earthquakes in Subduction Zones. Pure appl. geophys. 154, 467–483. https://doi.org/10.1007/s000240050240

Satake, K., Baba, T., Hirata, K., Iwasaki, S.I., Kato, T., Koshimura, S., Takenaka, J., & Terada, Y., 2005. Tsunami source of the 2004 off the Kii Peninsula earthquakes inferred from offshore tsunami and coastal tide gauges. Earth, Planet and Space, Vol. 57, pp. 173–178. https://doi.org/10.1186/BF03351811

Sepúlveda, I., P. L.-F. Liu, M. Grigoriu, & M. Pritchard (2017), Tsunami hazard assessments with consideration of uncertain earthquake slip distribution and location, J. Geophys. Res. Solid Earth, 122, 7252–7271. https://doi.org/10.1002/2017JB014430

Setiyono, U., Gusman, A.R., Satake, K., & Fujii, Y., 2017. Pre-computed tsunami inundation database and forecast simulation in Pelabuhan Ratu, Indonesia. Pure Appl. Geophys. 174, 3219–3235. https://doi.org/10.1007/s00024-017-1633-8

Soloviev, S.L., & Go, Ch. N., 1974. A catalogue of tsunamis on the western shore of the Pacific Ocean. Nauka Publishing House, Moscow, USSR, 310 p, Canadian Translation of Fisheries and Aquatic Sciences pp. 5077.

Tajima, Y., Matsuba, Y., Yamanaka, Y., Shimozono, T., & Kato, F., 2024. Estimation of tsunami characteristics under rough wind waves in the 2024 Noto Peninsula Earthquake, Coastal Engineering Journal, 66:3, 419-433. https://doi.org/10.1080/21664250.2024.2385784

Tanioka, Y., Satake, K., & Ruff, L., 1995. Total analysis of the 1993 Hokkaido Nansei-Oki Earthquake using seismic wave, tsunami, and geodetic data. Geophysical Research Letters, Vol. 22, pp. 9–12. https://doi.org/10.1029/94GL02787

Tanioka, Y., Kususose, T., Kathiroli, S., Nishimura, Y., Iwasaki, S. I., & Satake, K., 2006. Rupture process of the 2004 great Sumatra-Andaman earthquake estimated from tsunami waveforms. Earth Planets Space, 58, 203-209. https://doi.org/10.1186/BF03353379

Tappin, D. R., Grilli, S. T., Harris, J. C., Geller, R. J., Masterlark, T., Kirby, J. T., Shi, F., Ma, G., Thingbaijam, K.K.S., & Mai, P. M., 2014. Did a submarine landslide contribute to the 2011 Tohoku tsunami?, Marine Geology, Volume 357, Pages 344-361, ISSN 0025-3227. https://doi.org/10.1016/j.margeo.2014.09.043

Tsushima, H., R. Hino, H. Fujimoto, Y. Tanioka, & F. Imamura, 2009. Near-field tsunami forecasting from cabled ocean bottom pressure data, Journal of Geophysical Research, Vol. 114, pp. B06309, https://doi.org/10.1029/2008JB005988

Ward, S. N., 2001. Landslide tsunami, J. Geophys. Res., 106(B6), 11201–11215. https://doi.org/10.1029/2000JB900450

Watts, P., Grilli, S. T., Tappin, D. R., & Fryer, G. J., 2005. Tsunami generation by submarine mass failure. II: Predictive equations and case studies. Journal of waterway, port, coastal, and ocean engineering, 131(6), 298-310. https://doi.org/10.1061/(ASCE)0733-950X(2005)131:6(298)

Yamanaka, Y., Sato, S., Shimozono, T., & Tajima, Y., 2019. A numerical study on nearshore behavior of Japan Sea tsunamis using Green’s functions for Gaussian sources based on linear Boussinesq theory. Coastal Engineering Journal, Vol. 61(2), pp. 187–198. https://doi.org/10.1080/21664250.2019.1579462

Yamanaka, Y., & Shimozono, T., 2021. Rapid assessment of tsunami source impacts on low-lying coastal areas using offshore wave superposition and static sweep of onshore terrain. Coastal Engineering Journal, Vol. 64(2), pp. 229–245. https://doi.org/10.1080/21664250.2021.2005364

Yamanaka, Y., & Tanioka, Y., 2024. Tsunami waveform inversion using Green's functions with advection effects: application to the 2003 Tokachi–Oki earthquake. Earth, Planet and Space, 76, 71. https://doi.org/10.1186/s40623-024-02006-7

Yamanaka, Y., Matsuba, Y., Shimozono, T., & Tajima, Y., 2024. Nearshore propagation and amplification of the tsunami following the 2024 Noto Peninsula Earthquake, Japan. Geophysical Research Letters, 51, e2024GL110231. https://doi.org/10.1029/2024GL110231

Yanagisawa, H., Abe, I., & Baba, T., 2024. What was the source of the nonseismic tsunami that occurred in Toyama Bay during the 2024 Noto Peninsula earthquake. Sci Rep 14, 18245. https://doi.org/10.1038/s41598-024-69097-w

Yasuda, T., Takayama, T., Kawamura, K., & Mase, H., 2007. Real-Time Tsunami Prediction by Inverse Analysis of Tsunami Profiles Observed at Offshore Points. Proceedings of Coastal Engineering, JSCE, Vol. 54, pp. 196–200. https://doi.org/10.2208/proce1989.54.196

Yatimantoro, T., Yamanaka, Y., Gusman, A. R., Tanioka, Y., Ratnasari, R. N., & Karnawati, D., 2025. Investigation of a static source model for non-seismic tsunamis using waveform inversion: a case study of the 2018 Anak Krakatau event, Geophysical Journal International, Volume 241, Issue 1, April 2025, Pages 170–183. https://doi.org/10.1093/gji/ggaf037

Yokoi, H., Baba, T., Lin, Z., Minami, T., Kamiya, M., Naitoh, A., & Toh, H., 2023. Simultaneous inversion of ocean bottom pressure and electromagnetic tsunami records for the 2009 Samoa earthquake. Journal of Geophysical

Research: Solid Earth, Vol. 128, pp. e2023JB026956. https://doi.org/10.1029/2023JB026956

Yokota, Y., Koketsu, K., Fujii, Y., Satake, K., Sakai, S., Shinohara, M., & Kanazawa, T., 2011. Joint inversion of strong motion, teleseismic, geodetic, and tsunami datasets for the rupture process of the 2011 Tohoku earthquake, Geophysical Research Letters, Vol. 38, pp. L00G21, https://doi.org/10.1029/2011GL050098

Yoshida, K., Uchida, N., Matsumoto, Y., Orimo, M., Okada, T., Hirahara, S., et al. (2023). Updip fluid flow in the crust of the northeastern Noto Peninsula, Japan, triggered the 2023 Mw 6.2 Suzu earthquake during swarm activity. Geophysical Research Letters, 50, e2023GL106023. https://doi.org/10.1029/2023GL106023

Yuhi, M., Umeda, S., Arita, M., Ninomiya, J., Gokon, H., Arikawa, T., et al., 2024. Post-event survey of the 2024 Noto Peninsula earthquake tsunami in Japan. Coastal Engineering Journal, 66(3), 405-418. https://doi.org/10.1080/21664250.2024.2368955

Zhu, Yf., An, C., Wang, T., & Liu, H., 2021. Time-Dependent Tsunami Source Following the 2018 Anak Krakatau Volcano Eruption Inferred from Nearby Tsunami Recordings. China Ocean Engineering, Vol. 35, pp.145–152. https://doi.org/10.1007/s13344-021-0013-4